Università degli Studi "Roma Tre"

Faculty of Mathematical, Physical and Natural Sciences

Department of Physics "Edoardo Amaldi"

MoCA: a Monte Carlo code for accretion in Astrophysics

Candidate:
Francesco Maria Tamborra

Supervisor:
Prof. Giorgio Matt
Co-advisor:
Dr. Stefano Bianchi

February 2013

"Physics isn't a religion.
If it were, we'd have a much easier time raising money."
(Leon Lederman)

Contents

Introduction

Accretion is a common mechanism in astrophysics and, due to its peerless efficiency it is the only one able to power the most luminous objects in the sky. From the point of view of energetics the question is very simple: the gravity of the accreting source attracts matter which, due to its angular momentum, forms an accretion disc. The gravitational potential energy is converted in kinetic energy and viscosity forces inside the disc convert this energy into radiation. The efficiency of this process is the highest in nature and, if the gravitational potential well is deep enough, huge luminosities can be reached.

Compact objects are among the most exotic sources in the Universe and their luminosity is produced by accretion. The class of compact objects includes Neutron Stars (NSs), White Dwarfs (WDs) and Black Holes (BHs), objects which show a very high compactness, M/R, and differ from all the other stars because there are no thermonuclear fusion processes that produce radiation and counteract their gravity. When these objects are in a binary system, matter from the companion star accretes onto the compact object forming an accretion disc which can produce a large amount of radiation in X-ray band. These systems are called X-ray binaries (XRBs). The X-ray spectrum produced is complex and constituted by several components, due to the circumnuclear material which scatters, absorbs and reprocesses X-ray photons produced by the disc. Furthermore, the spectral energy distribution can have a different shape depending on the state of the XRB. A common feature in all XRBs X-ray spectra is a strong Iron K_α emission line at $6.4\,keV$. The line is produced by the reprocessing of X-ray photons absorbed by the neutral disc. These lines often show a broad energy profile and the origin of this broadening is still matter of debate. The two common interpretations are that it is given either by General Relativistic effects or by Comptonization (or, of course, by a combination of the two). One way to discriminate between these explanations is given by the polarization signal. In the case of Comptonization, in fact, some degree of linear polarization is expected to be measured in the line flux while for GR broadening it is not predicted.

Another case of astrophysics interest in which X-ray polarization plays a key role is on the determination of the corona geometry in Active Galactic Nuclei (AGN). The term AGN refers to a few percent of galaxies whose emission from the inner region is ascribed to accretion onto a super massive black hole (SMBH). As for XRBs, the emission, in all the energy bands of the electromagnetic spectrum, is complex and constituted by several components. One important difference is that in AGN the accretion disc radiates in the UV/optical band rather than in X-ray band. Therefore, X-ray emission in AGN is due only to the scattering electrons cloud which surrounds the inner part of the disc, known as 'corona'. The characteristics of the corona, especially the geometry, are still unknown. Measuring the polarization signal in the X-ray spectra of AGN, offers the unique possibility to constrain some of the corona properties.

In the framework of this scenario we developed MoCA, a code dedicated to the study of the spectrum and the polarization signal produced in accreting sources. We applied our code to the two issues described before: the spectrum and the polarization signal of the continuum X-ray emission in AGN and the Comptonization of the Iron line in XRBs. The code includes all special relativistic corrections and it is modular, allowing, with minor modifications, to be applied to different accreting systems and astrophysical situations.

The structure of this thesis is as follows. **Chapter 1** introduces the reader to the physics and classification of compact objects, with a particular regard for AGN and black hole X-ray binaries (BHXBs). In **Chapter 2** the basic physics governing the mechanism of accretion will be illustrated while **Chapter 3** is devoted to a brief review on Comptonization. In **Chapter 4** a detailed description of the physical model adopted to study the two cases mentioned before will be shown while **Chapter 5** contains a description of the algorithms used to perform the calculations described in Chapter 4. In **Chapter 6** we show the results of the simulations while in **Chapter 7** the conclusions of this work together with possible future developments will be discussed.

Chapter 1

Phenomenology of Compact Objects

Compact objects are among the most exotic sources in the Universe. As we will see in detail in the next chapter, accretion is the physical mechanism responsible for their energy release. Within the class of compact objects we can include Neutron Stars (NSs), White Dwarfs (WDs) and, of course, Black Holes (BHs). These objects show a very high compactness, M/R and differ from all the other stars because there are no thermonuclear fusion processes that produce radiation and counteract their gravity. This is the reason why they are also called 'collapsed objects'. In the case of WDs and NSs, the degenerate-pressure of a gas of fermions (electrons and neutrons, respectively) counteracts the gravity. For BHs, further collapse is unavoidable and a singularity in the space-time is produced. In this chapter we are going to focus on the phenomenology of two subclasses of sources: 'Active Galactic Nuclei' (AGN) and 'X-ray Binaries' (XRBs). Both sources have a BH as central engine and even if there are some similarities, the differences can be as much. X-ray Binaries are systems in which a stellar BH (i.e. a BH formed by the collapse of a massive star) accretes matter from a companion star. The term AGN, on the other hand, refers to those Super Massive Black Holes (SMBHs), lying at the center of a galaxy, which accrete matter from the galaxy itself (gas and stars). BHs are very simple objects, defined by only three independent parameters: the mass, the angular momentum (the spin) and the electric charge.[1] Nonetheless, the mass of the BH ($\sim 10 M_\odot$ for BHXBs and in the range $10^6 - 10^{10} M_\odot$ for AGN) and especially the circumnuclear matter, can produce drastically different phenomena and al-

[1] It is usually assumed that the electric charge is negligible for astrophysically relevant BHs.

ter properties such as the luminosity and the spectral energy distribution between the two systems.

1.1 AGN

As said before, the term AGN refers to a few percent of galaxies whose emission from the inner region cannot be ascribed to stars. The 'zoo' of galaxies that fits this definition is wide and varied, and the classification, mainly based on luminosity and spectroscopical features, is complex and not always straightforward.

The main and common trait of AGN is their huge luminosity, typically in the range $10^{42} - 10^{48}\ erg\ s^{-1}$, that span over ~ 20 decades of the electromagnetic spectrum, making them among the most luminous objects in the sky from radio to gamma rays. Any source can reach a maximum value of luminosity called 'Eddington luminosity' where where the continuum radiation force outwards balances the gravitational force inwards in hydrostatic equilibrium. If the luminosity exceeds this limit, then the radiation pressure drives an outflow. Whatever the emission mechanism is involved, the limit Eddington Luminosity relation (for fully ionized hydrogen gas)

$$L_{Edd} = \frac{4\pi G M m_p c}{\sigma_T} \cong 1.3 \times 10^{38} \left(\frac{M}{M_\odot}\right) \frac{erg}{s} \tag{1.1}$$

tell us that a mass of the order $M \approx 10^8 M_\odot$ is required to achieve the typical AGN luminosity.

Another important characteristic shared among AGN is their variability timescales, of the order of days or less, which implicates a sub-parsec scale size of the emitting region

$$R_{AGN} \approx c \times t \ll 1\ pc \ll R_{Galaxy} \approx 10^4\ pc$$

as confirmed by many observations showing an unresolved emission core in all electromagnetic bands. The extreme compactness of AGN leads naturally to consider SMBHs liable for the huge luminosity. After all is well-known that 'normal' galaxies, like our own, host SMBHs at their core with masses of $10^6 M_\odot - 10^8 M_\odot$, directly estimated by stellar kinematics (see Schodel et al. 2006 [67] for details). The 'SMBH paradigm' is nearly unanimously accepted among the scientific community and represents the starting point to understand the AGN physics.

If a SMBH converts mass to energy at a rate of $\dot{M}$, it must do it with high efficiency η to produce the immense luminosity observed

$$L = \eta \dot{M} c^2 \tag{1.2}$$

Low efficiency stellar nuclear reactions like pp-chain, $\eta = 0.007$, or triple-alpha process, $\eta = 0.00062$ are ruled out. The only plausible alternative is accretion, a process where matter around the black hole slowly spirals inward converting gravitational potential energy in kinetic energy. As we will see in the next chapter, this kinetic energy, converted in internal energy, can be dissipated and produce a large amount of radiation, with efficiencies in the range $\eta \approx 0.06 - 0.4$.

With a prudential value of $\eta = 0.1$, from (1.2), it is possible to reach Eddington luminosity with an accretion rate of

$$\dot{M}_E \equiv \frac{L_E}{\eta c^2} \cong 10^{-8} M_8 \frac{M_\odot}{s} \tag{1.3}$$

a quite reasonable value if compared to the typical black hole masses involved, $M_{BH} = 10^8 M_\odot = M_8$.

1.1.1 AGN Taxonomy

The taxonomy of AGN tends to be rather confusing as we do not yet fully understand the physics underlying this phenomenon. Undoubtedly some of the differences we see between various types of AGN are due more to the way we observe them than to intrinsic differences; this theme represents the basis of the unification models.

In Figure 1.1, a summarizing scheme shows some of the various 'species' of the rich AGN family.

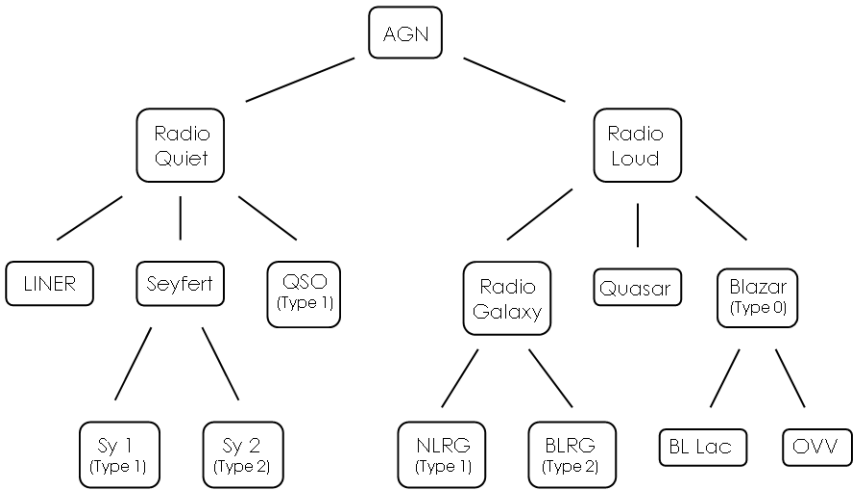

Figure 1.1: *AGN taxonomy scheme*

A detailed description of all the different types of AGN does not fall in the purposes of this thesis. We just want to broadly give an idea of the classification and introduce the Unification Model for AGN. A first classification criterion comes from the radio luminosity (L_R) to optical luminosity (L_O) ratio. When $\frac{L_R}{L_O} \lesssim 10$, objects are classified as 'radio-quiet' while if the ratio exceed the value of 10 they are classified as 'radio-loud'. Radio-loud objects comprise about 15% of the total. Another criterion is based on optical/UV spectroscopical features and allow to mark as 'type I' those AGN which exhibit both broad and narrow emission line in their spectra, and as 'type II' those where only narrow emission lines are present. The 'type 0' label indicates atypical AGN with very faint or no emission lines compared to continuum emission. This spectral classification represent the basis for the unification.

1.1.2 The Spectral Energy Distribution

In this section the main properties of AGN across the whole electromagnetic spectrum, with particular attention to the X-ray component, will be briefly described according to our present, still incomplete, knowledge. The following description, in the context of the Unification Model (see section 1.3), applies to all AGN, once the peculiar properties of each subclass are taken into account. Figure 1.2 shows the typical spectral energy distribution (SED) for radio-quiet and radio-loud AGN.

Optical/UV

The dominant feature in optical/UV band is the so-called 'big blue bump', where the peak of AGN emission is usually found. The peak energy is around the Lyman edge ($\lambda = 1216$ $\mathring{A}$), and the spectrum can be well approximated with a power law both at lower and higher frequencies (see Figure 1.3). The big blue bump is generally ascribed to thermal emission from the accretion disk which, as we will see in the next chapter in more detail, peaks in the UV band. Even if appealing, this connection is not well constrained because of starlight contamination by the host galaxy, absorption by materials on the line of sight and reddening by dust. Moreover, superposition of emission lines makes the analysis difficult. In particular, between ~ 2000 $\mathring{A}$ and 4000 $\mathring{A}$, a blend of Balmer and FeII lines from the 'Broad Line Region' (BLR), constituting the 'small blue bump', alters the shape of the underlying continuum. Even considering all these effects and correcting for them, observed spectra do not match with spectra predicted by the simplest (Shakura and Sunyaev) accretion model. Albeit the assumption of blackbody emission

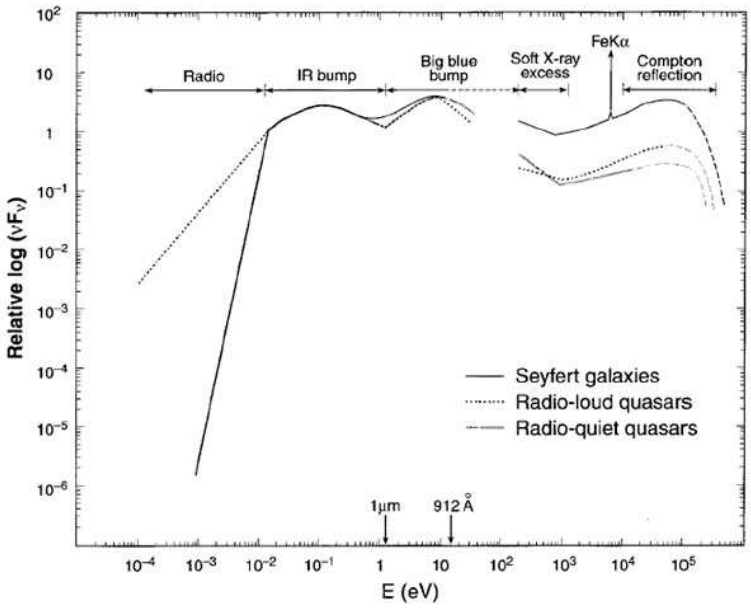

Figure 1.2: *Spectral energy distribution for Seyfert (thick solid line), radio-loud (dotted line) and radio-quiet (thin solid line) QSOs. The gap between* $1000-100$ *Å* $(10-10^2$ *eV) is due to HI absorption from our own galaxy; above* 100 *μm* $(< 10^{-2}$ *eV) there is the 'submillimeter break' (see §2.2).*

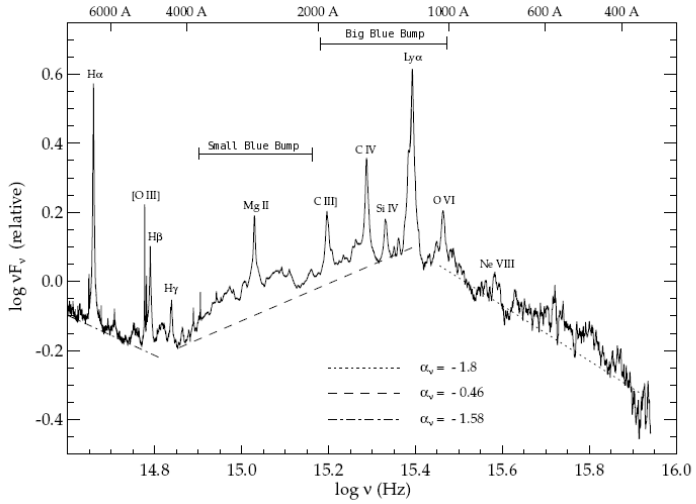

Figure 1.3: *Composite quasar spectrum in optical/UV band. For* $\lambda >$ *Lyα data are obtained from* $\sim$*2200 Sloan Digital Sky Survey (SDSS) quasar spectra (Vanden Berk et al. 2001 [80]). For* $\lambda <$ *Lyα data are obtained from HST/FSO observation of radio-quiet quasars (Zheng et al. 1997 [83]). The change in the slope at* 5000 *Å might be due to starlight contamination from host galaxies.*

from the accretion disk is a useful starting point, it is an oversimplification. Many attempts have been made to refine the predictions of the spectrum produced by accretion. In some cases, for example, models of stellar atmosphere (although with inappropriately high surface gravities) have been used to approximate the disk spectrum. More complex models, properly dealing with rotational, inclination, and relativistic effects have been developed (e.g. Sun and Malkan 1989 [70] among others). Two important predictions resulting from simulations are:

- *Polarization of the continuum.* Scattering effects lead to a significant polarization of the accretion-disk continuum. For edge-on disks, the polarization should reach several percent of the total.

- *Lyman discontinuity.* The Lyman edge (912 $\mathring{A}$), either in emission or absorption, is expected to be observed in any source in which there is a temperature gradient because the opacity drastically changes at this wavelenght.

Neither of these features is clearly observed in optical/UV AGN spectrum. Another problem with the multi-temperature blackbody emission concerns variability. One of the basic assumption of the model is that photons with different energies come from different radii of the disk and, as a direct consequence, if different parts of the disk undergo changes in local emitting conditions then the relative change in the respective electromagnetic bands is expected to be seen with a time delay proportional to the sound speed in the disk. Actually, observations seems to suggest that UV and optical variability are indeed simultaneous (see Ulrich et al. 1997 [77]), requiring propagation speeds tipically higher than 0.1 c, very difficult to reconcile with the standard accretion disk model. A viable alternative to thermal emission is represented by optically thin emission processes like bremsstrahlung. The advantages of free-free emission models are that Lyman edge is expected to be weak as long as the temperature is high ($\sim 10^6\ K$) and that polarization is expected to be low, but the efficiency also is fairly low. Moreover these models do not match very well with the rapid X-ray variability observed.

The broad lines observed in the optical/UV spectra of AGN have typical widths of 5000 $km\ s^{-1}$, but can be as large as 30000 $km\ s^{-1}$. Such widths are due to the keplerian velocities of a large number of clouds (the Broad Line Region: BLR) quickly rotating around the central SMBH at a distance of $0.01 - 0.1\ pc$. The density of this gas is believed to be very high, of the order of $10^9 - 10^{11}\ cm^{-3}$, as required by the observed ratio between forbidden and

permitted emission transitions. The origin of these clouds is still under debate. Several models have been proposed, such as the release from accretion disk instabilities (Collin & Huré 2001 [10]) or from stellar wind envelopes (Torricelli-Ciamponi & Pietrini 2002 [74]). The main problem is represented by the mechanism providing the confinement of the BLR clouds. The alternative Unification Model proposed by Elvis [15] has in the outflowing wind the right candidate to play this role.

The narrow lines have much smaller widths, typically of the order of 100 $km\ s^{-1}$, and it is thought they are produced by a material (the Narrow Line Region: NLR) farther away from the SMBH and extending on the $\sim kpc$ scale, as directly observed. The gas has a density lower than the BLR, typically in the range $10^3 - 10^6\ cm^{-3}$ and is likely composed by the inner part of the galactic disk, photoionized by the nuclear continuum.

Infrared

The infrared emission of quasars has been systematically studied with the 'Infrared Astronomical Satellite' (IRAS; Sanders et al. 1989 [65]), and, more recently, with the 'Infrared Space Observatory' (ISO; Haas et al. 2003 [31]) and 'Spitzer' satellites. The latter confirms the basic results of the former, while adding further details. The origin of the infrared continuum emission is uncertain and still matter of debates, but some evidence seems to suggest a thermal origin, in terms of reprocessing of the primary radiation from dust.

The almost ubiquitous presence of a hump in the spectrum (the 'IR bump'), tipically around $10 - 30\ \mu m$ (but there are examples of peaks anywhere between 2 and 100 μm) is naturally interpreted as thermal emission from dust whose temperature does not exceed $\simeq 2000\ K$ with the minimum around 1 μm being the corresponding Wien cut-off.

While variability between optical and UV continuum emission does not exhibit a measurable time delay, and X-ray continuum emission shows a correlation with them with little time delay, in IR band we see the same variations observed in optical/UV band but with a significant time delay. For the well studied case of Fairall 9, such a delay was measured in about 400 days (Clavel et al. 1989 [8]). This time delay implies that the dust closest to the nucleus (and thus hottest) resides at a distance $\lesssim 1\ pc$, in good agreement with the expected dust sublimation radius for an object with the luminosity of Fairall 9.

Various observations highlighted a steep decline at submillimeter wave-

lenghts ($\sim$ above 100 μm) which can be easily understand as the decreasing of dust grains emitting efficiency at long wavelenghts ($\propto \nu^2$). It seems thus reasonable to picture a scenario where the UV/optical continuum from the nucleus fully depletes the dust up to the sublimation radius. Beyond this radius, the same radiation heats the dust to a wide range of temperatures (depending on the distance from the central source), producing the observed IR bump. It should be noted, however, that IR continuum expected from a quasar or a starburst is strongly dependent on the geometry and physical properties of the reprocessing medium, and the same observed continuum can be successfully explained with more than one model (Elitzur et al. 2004 [14]). The spectrum between the IR bump and submillimeter wavelenghts, for example, can be reproduced by a power law with spectral index close to $\alpha = 2.5$, as expected from synchrotron self-absorption. Under this assumption, the main emission mechanism would be synchrotron emission from relativistic electrons instead of reprocessing by dust.

Radio

Depending on the radio-loudness of the source, the radio emission can be significantly different, as expected. However, in all cases, the radio emission provides a negligible fraction of the bolometric luminosity, being about 3 orders of magnitude and up to 5-6 orders of magnitude lower than the UV/optical continuum for radio-loud and radio-quiet AGN, respectively (see Figure 1.2). The emitting region is usually very compact, but there are a few cases of *kpc* scale radio jets, which are the possible counterparts of the larger structures (the lobes) seen in radio-loud AGN. The flatness of the radio spectrum, a clear sign of non-thermal emission, is ascribable to synchrotron radiation. This interpretation is supported by the presence of low frequency cut-offs in some objects, as expected for synchrotron self-absorption, even if the frequency dependence is often not as steep as it should be.

X-rays

High-energy (X-ray and γ-ray) observations are of great importance for the understanding of the AGN phenomenon. Not only do X-rays account for tipically $\sim 10\%$ of the bolometric AGN luminosity, but they provide a probe of the innermost region of active nuclei. In fact they are emitted very close to the black hole, as indicated by their rapid variability.

Before going on it is useful to know that in X-ray astronomy, power law SEDs are usually fitted in units like photons per keV rather than energy per

unit frequency. X-ray power law fits are generally of the form

$$P_E \left[\frac{photons}{keV \cdot s}\right] \propto E^{-\Gamma} \propto \nu^{-\Gamma}$$

since *photons per second* is close to the measured quantity, which is *counts per second*. In units of energy flux (or luminosity) as we have used so far

$$F_\nu \propto P_E \left[\frac{photons}{keV \cdot s}\right] \times h\nu \left[\frac{ergs}{photon}\right] \propto \nu^{-\Gamma+1} \propto \nu^{-\alpha}$$

To distinguish clearly between these two spectral indices, α is usually referred as the 'energy index' and Γ $(= \alpha + 1)$ is called the 'photon index'.

Coming back to AGN, in Figure 1.4 a plot reproducing the typical X-ray spectrum of a type I AGN is shown. By having a glance at the spectrum it

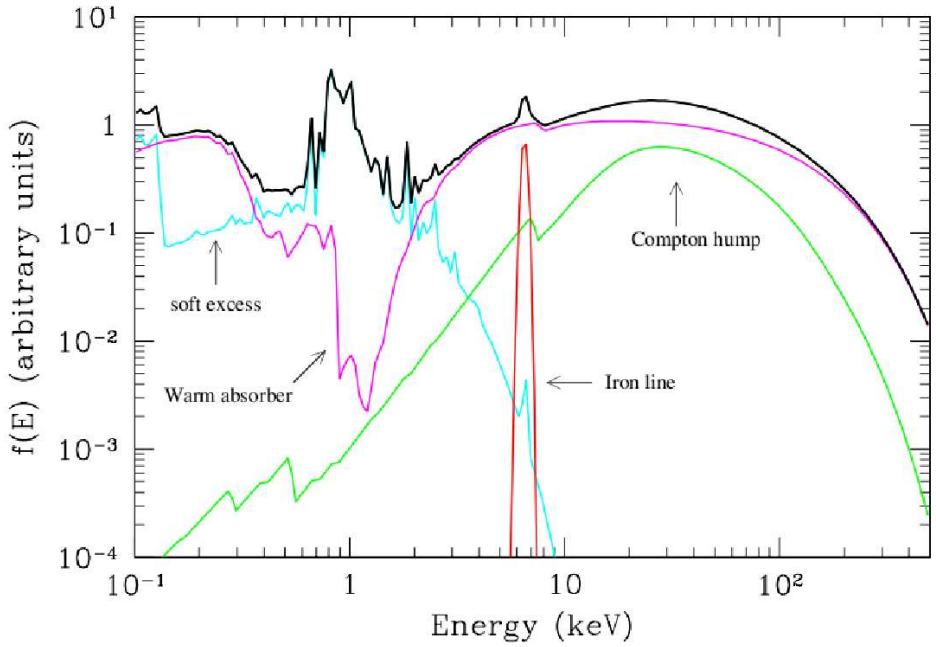

Figure 1.4: *Average total spectrum (thick black line) and main components (thin coloured lines) in the X-ray spectrum of a type 1 AGN. The main primary continuum component is a power law (pink line) with an high energy cut-off at E* $\sim 100 - 300\,keV$*, absorbed at soft energies by warm gas. A cold reflection component (green line) is also shown. The most relevant narrow feature is the iron K*α *emission line at* $6.4\,keV$ *(red line). Finally, a 'soft excess' is shown (pale blue line). (from Risaliti & Elvis, 2006)*

is clear that the physics behind X-ray emission from AGN is not simple. In the following sections the mechanisms wich are believed to be responsible for X-rays production in AGN will be discussed.

- The primary emission

The X-ray emission from AGN extends from the galactic absorption cut-off at $\sim 0.1\,keV$ up to $\sim 300\,keV$. The intrinsic continuum X-ray emission of AGN is to first order a power law.

However, as higher resolution and better signal-to-noise spectra have become available, emission and absorption features have been found (see Figure 1.4). The typical spectral index of the power law is between $\Gamma = 1.8-2$, both for low luminosity Seyfert galaxies and high luminosity quasars. Radio-loud AGN have a somewhat flatter spectrum ($\Gamma = 1.5 - 1.7$).

The origin of the 'power law component' cannot be directly ascribed to the accretion disc because, as we have seen before and will see in more detail in the next chapter, for a SMBH the peak of the emission is in the Optical/UV band. However many authors, shortly after the paper by Shakura and Sunyaev, realized that 'Comptonization'[2] in a surrounding hot 'corona' of UV thermal photons produced by accretion would be a good mechanism to reproduce the observed X-ray emission in AGN. The simplest model is the so-called 'two-phase model' and was proposed by Haardt and Maraschi in 1991 [29]. The basic idea assumes a 'sandwich geometry' where the standard accretion disk (the 'cold phase') is completely surrounded by a hot corona (the 'hot phase') consisting of an electron-positron pairs plasma in thermal equilibrium at a temperature T_e. The thermal distribution of electrons is favoured with respect to a non-thermal one, since it may explain the observed high-energy cut-off at $\sim 80 - 300\,keV$ (Perola et al. 2002 [54]). The model envisages that the release of gravitational power occurs in the hot phase, assumed to be optically thin ($\tau < 1$), so that the main cooling mechanism is Comptonization of the soft photons emitted by the thick phase. The two phases are indeed coupled, i.e. the optically thick emission of the cool layer provides the soft photon input for the Comptonization, and hard Comptonized photons contributes to the heating of the thick phase. The feedback between the two phases determines the fraction of the total power emitted in the three main spectral components: a blackbody from the optically thick phase, a power law from Comptonization in the hot layer, and a reflection component. The resulting spectrum is found to be largely independent of

[2]This term refers to the mechanism of inverse Compton (see Chapter 3); it is used also as a verb, i.e. 'photons Comptonized by electrons'.

the coronal parameters and in good agreement with observations (see Figure 1.5).

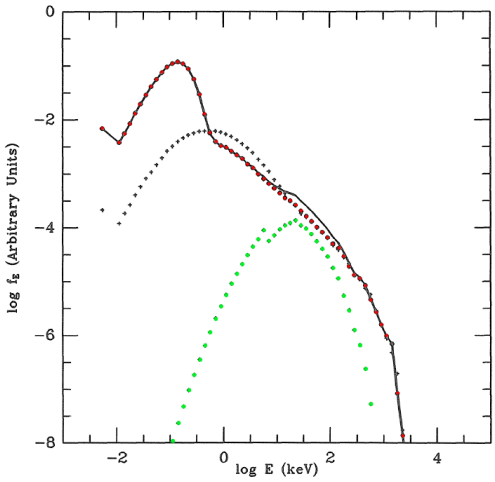

Figure 1.5: *Monte carlo simulation of emitted spectrum (solid line), obtained adding the upward Comptonized spectrum (red dots) and the reflected component (green dots). The downward Comptonized spectrum (black crosses) is also shown. The hot pahse parameters are* $\tau = 0.1$, $\Theta = 0.51$. *The soft photon source is a blackboddy with* $kT = 50\ eV$. *(from Haardt and Maraschi, 1991)*

Moreover, the spectral index Γ (which depends on τ and T_e) is actually anticorrelated to the corona temperature, so that an increase of the spectral index is due to a decrease of T_e. Observations of long time scale (i.e. > 1 day) variability show that the photon index increases as the $2 - 10\,keV$ flux increases (see e.g. Perola et al. 1986 [53]). These results support the thermal Comptonization models, since this behaviour is expected if the X-ray spectral variability is mainly driven by a variation of the UV flux, which in turns changes the cooling of the corona. On the other hand, X-ray variability on time scales of a few hours or less is generally completely uncorrelated with the UV emission and is probably associated to local processes, such as reconnection instability in a magnetically dominated corona (di Matteo 1998 [12]).

However, this simple model presents some problems when compared to the data. As we mentioned before, one of the assumptions the model requires to reproduce the observed parameters is that most of the gravitational energy must be dissipated in the corona instead of in the disk, leading necessarily to an X-ray luminosity comparable to that in the UV band. That is contrary to the observations, since UV luminosities are much larger. A possible solution

to this problem can be found in a more complex geometry of the system. In particular, a 'patchy corona' was proposed by Galeev et al. in 1979 [24] and further developed by Haardt et al. in 1994 [30], where the hot electrons are not distributed evenly around the disk, but partially cover it. In this case, the emission from the regions of the disk under the active clouds is effectively dominated by the radiation produced in the corona, but the rest of the disk simply radiates as the corona were not present. An alternative mechanism to the hot corona model was proposed by Ghisellini et al. in 2004 [26]. They suggest that the central BHs in radio-quiet AGN power outflows and jets intermittently, producing blobs of material. The ejection velocity may be smaller than the escape velocity, causing the blobs to fall back and eventually collide with the blobs still moving outwards because produced later. In the collision, the bulk kinetic energy of the blobs is dissipated and effectively accelerates the electrons of the plasma. Their rapid cooling via inverse Compton processes leads to the production of the X-ray continuum. The main difference with the hot corona scenario, whose source of energy is only accretion, is that the 'aborted jets' model provides a viable method to power high energy emission also through extraction of rotational energy from the BH. Moreover, it is interesting to note that this mechanism does not necessarily exclude a contribution from a hot corona: on the contrary, both processes may be simultaneously active in AGN.

- The reprocessed spectrum

As we have seen in the previous section, the 'two-phase' model predicts that a part of Comptonized photons (one-half, if the corona emission is isotropic) falls down to the accretion disk again. Hard photons directed downward are partly absorbed and then re-emitted as black body radiation and partly reflected (Compton scattered), adding to the primary spectrum emitted by the corona[3]. The shape of the reprocessed spectrum depends strongly on the ionization state of the disk. If the matter is highly ionized, the Compton scattering becomes the principal interaction mechanism, leading to a spectrum hard to distinguish from the primary continuum. On the other hand, if the matter is mostly neutral, as it is likely to be, photoelectric absorption prevails at lower energies, producing the so called 'Compton reflection' component, a sort of hump peaking at $20 - 30\,keV$ (see e.g. George & Fabian 1991 [25]; Matt et al. 1991 [44]). Photoelectric absorption from electrons in the K shell of the metallic elements of the disk can be followed by the emission of K_α lines. The strongest emission line is produced by iron, at

[3]Second-order reflection from the hot layer can be shown to be unimportant for $\tau < 1$.

$6.4\,keV$ if the matter is mostly neutral, at 6.68 and $6.97\,keV$ from more ionized material. The iron line profile is intrinsically narrow, apart from the natural broadening (much lower than the resolution of X-ray instruments). However, if it is produced in the accretion disk, as expected, a number of effects contribute to forge a peculiar profile (see Fabian et al. 2000 [17], for a review). Firstly, the line is broadened because of the rotation velocity of the accretion disk. Each radius produces a double-horned line profile, with the blue peak due to the region approaching the observer, and the red one to the receding region (first panel in Figure 1.6). The effect is clearly higher for the inner radii of the disk, whose rotational velocities are larger. Since these velocities reach easily relativistic values, the blue peaks are beamed and thus enhanced with respect to the red ones. Moreover, the transverse Doppler effect also becomes important, shifting the overall profile to lower energies (second panel in Figure 1.6). A comparable effect is due to gravitational redshift, as shown in the third panel of Figure 1.6.

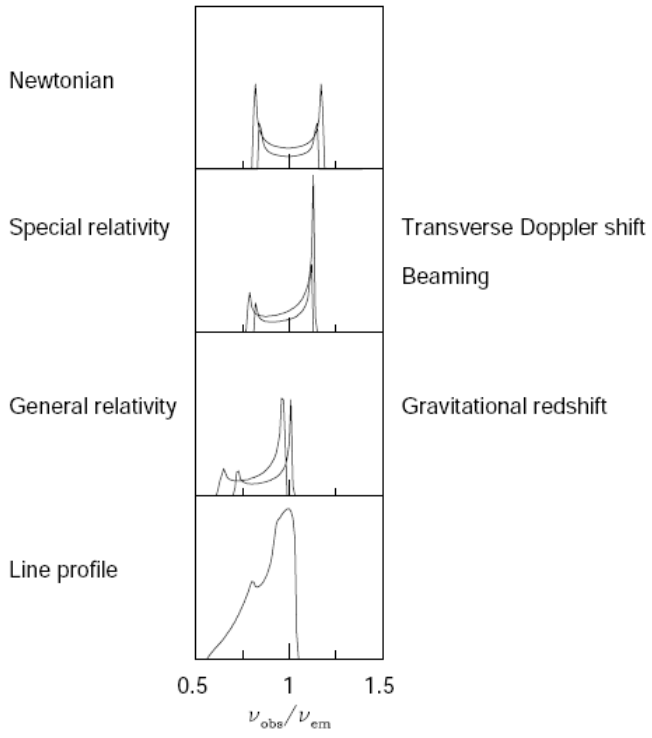

Figure 1.6: *All the individual effects that contribute to forge the characteristic double-horned relativistic line. (from Fabian et al., 2000)*

The resulting profile is a good diagnostic tool both for the accretion disk

and the central black hole's properties. It is very sensitive to the inclination angle of the disk with respect to the line of sight and, more subtly, to other parameters, including the spin of the BH and the line emissivity of the accretion disk. Moreover, the behaviour of the $K\alpha$ line profile in response to variations of the primary continuum could provide a technique to measure the mass of the central SMBH, as first proposed by Stella in 1990 [69] and, in a complementary way, by Matt and Perola in 1992 [43].

Figure 1.7 shows the reprocessed spectrum from a cold material, including all the above mentioned processes.

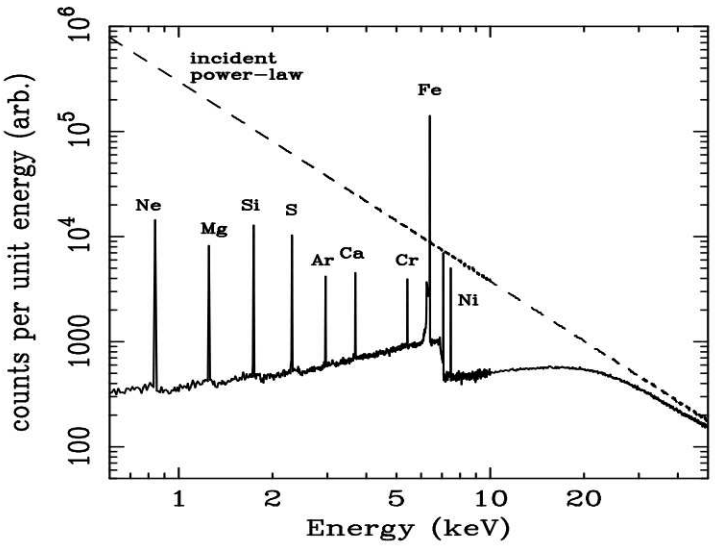

Figure 1.7: *Reflection of a power law X-ray spectrum from an optically thick material. The incident continuum is shown as a broken line, while the solid line is the reprocessed spectrum, including the $K\alpha$ lines from the indicated elements. (from Reynolds, 1999)*

- Reflection and absorption from the torus

Once escaped from the central regions, the X-ray photons can still be reprocessed by the various kinds of circumnuclear matter lying farther away from the nucleus. The most striking effect is the absorption from intervening neutral matter. The column density of the absorber discriminates between two kinds of sources: 'Compton-thick' if it exceeds the value $N_H > \sigma_T^{-1} = 1.5 \times 10^{24}\ cm^{-2}$ (i.e. when the optical depth for Compton scattering equals unity), completely blocking the nuclear continuum up to $10\,keV$ or more; 'Compton-thin' if it is lower, but still in excess of the Galactic one, allowing

only photons more energetic than a certain threshold (proportional to the column density) to pierce through the material (see Figure 1.8). The nature of this absorber comes naturally from the unification models, as the same medium responsible for the obscuration, in Seyfert 2 galaxies, of the nucleus and the BLR in the optical band, the so called 'torus'. The 'Compton-thick'

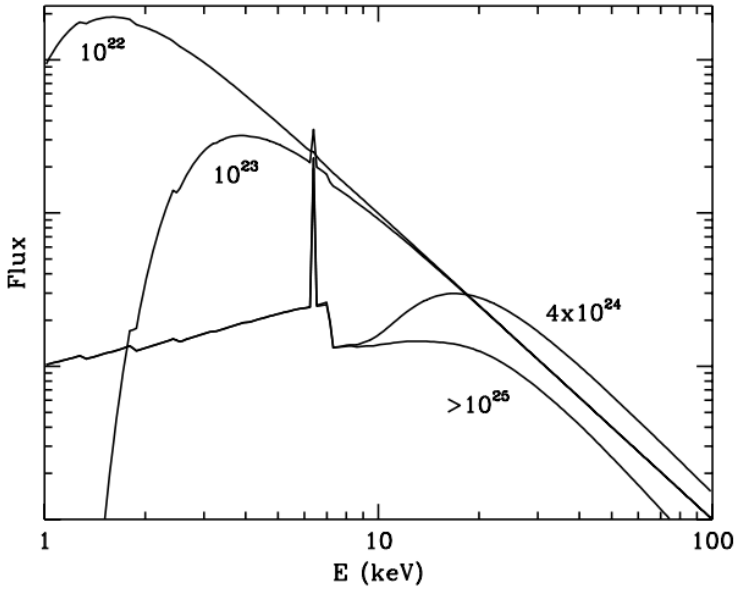

Figure 1.8: *The X-ray spectrum of an obscured Seyfert Galaxy, for different column densities of the absorber, assumed as a geometrically thick torus with an opening angle of* 30°. *See Figure 3.7 for the geometry. (from Matt et al., 2003)*

torus may be indirectly observed even if it does not intercept the line of sight. A part of the nuclear radiation hitting the inner walls of the material, can be scattered towards the observer (see the sketch in Figure 1.9). The reprocessed spectrum has the same shape as the Compton reflection component produced by the accretion disk. The main differences are associated with the larger distance of the torus from the nucleus, which has important effects on variability issues and line widths, and by the absence, in the radiation relfected by the torus, of general relativity distortion. Heavy absorption in the X-rays is very common, since about half of the optically selected Seyfert 2s in the local Universe are Compton-thick (Maiolino et al. 1998 [37]), while Risaliti et al. (1999, [62]) have shown that Compton-thin and Compton-thick objects have somewhat different optical properties. Moreover, there are a number of cases which suggest the presence of both materials in the same source. These considerations lead Matt in 2000 [42] to propose a modification of the Uni-

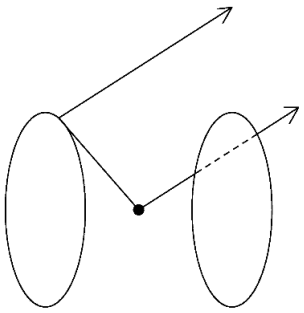

Figure 1.9: *Sketch of the simple geometry assumed for the torus. The opening angle is* 30°. *(from Matt et al., 2003)*

fication Model (see below) to take into account X-ray observations. In this scenario, the torus is assumed always to be Compton-thick, while Compton-thin absorption comes from large scale (hundred of parsecs) dust lanes, like the one observed with the *Hubble Space Telescope* (*HST*) by Malkan et al. in 1998 [39]. More recently. it has been shown (e.g. Risaliti et al. 2005 [63]) that absorbing clouds, sometimes even Compton-thick, may be present much closer to the BH, possibly associated with the BLR.

Finally, another circumnuclear material constituted by mostly ionized matter, is observed in a large fraction - as high as 50% - of unobscured (generally type 1) AGN as intervening gas producing a series of absorption lines and edges from ionized elements, the so-called 'warm absorber' (see Figure 1.4). A study by Blustin et al. (2005) [6] on a sample of 23 nearby AGN reveals some interesting properties of the warm absorbing gas like an average ionization parameter covering a wide range of values, a column densities in the range 10^{21-22} cm^{-2}, and typical outflowing velocities of a few hundreds $km\ s^{-1}$. The exact geometry of the warm absorber is unknown, although dynamical constraints are consistent with it originating as a radiation-driven high-velocity outflow in accretion disk instabilities (Krongold et al. 2005 [35]), and propagating up to typical NLR distances (Kraemer et al. 2006 [33]).

1.1.3 Unification Model

In 1985 when Antonucci and Miller [2] observed the Seyfert 2 NGC 1068 in polarized light, they noticed that broad lines, completely absent in the total spectrum, were clearly visible and similar to those observed in Seyfert 1s. This result led them to suggest that type 2 objects harbour a type 1 nucleus, which is obscured by intervening gas. Its presence may be indirectly

observed thanks to a reflecting 'mirror' (such as a gas of electrons) which scatters part of the nuclear radiation towards the line of sight, introducing a detectable degree of polarization. Therefore, the basic assumption of what was called the 'Unification Model' (see [1], for a review) is that type 1 and type 2 objects are absolutely equivalent, the only difference being whether the absorbing gas intercepts the line of sight to the nucleus or not. The absorbing medium assumes clearly the fundamental role in this scenario. It is usually envisaged as an optically thick 'torus' embedding the nucleus and the 'Broad Line Region' (BLR) (see Figure 1.10). If we observe the torus

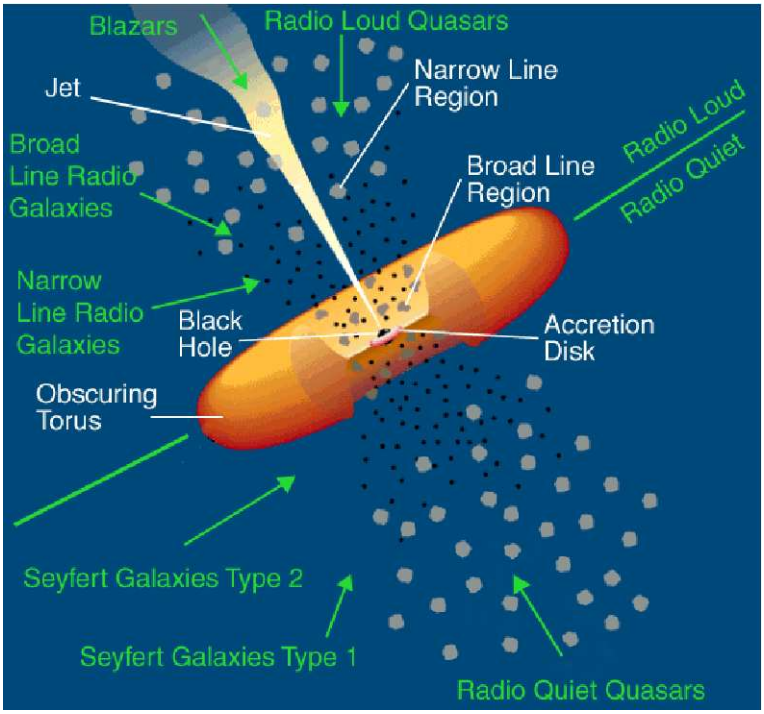

Figure 1.10: *AGN unification model sketch*

edge-on, all the nuclear radiation, including lines from the BLR which is inside it, is completely blocked and we classify the source as a type 2. The narrow lines are still visible, because the 'Narrow Line Region' (NLR) is located farther away from the nucleus, outside the torus. On the other hand, if the torus does not intercept our line of sight, we observe every component of the spectrum and the object is classified as a type 1.

The basic idea behind the Unification Model, i.e. geometrical effects play a fundamental role in the classification of AGN, is probably correct, but a number of observational evidence suggests that some complications should be introduced. Since the first work by Antonucci and Miller (1985), polarized

broad lines have been observed in several other Seyfert 2s, but there are also many examples of type 2 objects which, observed in polarized light, still do not present broad lines (see Tran 2001 [75] ,Tran 2003 [76]). Moreover, simple extrapolations of the optical/UV scenario to the X-ray emission do not easily fit the observations, leading sometimes to different classifications between the two bands. Indeed, a number of obscured objects in X-rays turn out to be type 1 AGN when observed in the optical band (Maiolino et al. 2001 [38], Fiore et al. 2001 [21], Fiore et al. 2002, [22]). There is also evidence for the existence of unobscured Seyfert 2s (Panessa & Bassani 2002 [52]). The great success of the classical Unification Model, together with the problems it cannot explain, justify all the efforts spent to propose a number of alternatives. Among them, one of the most promising is the one advanced by Elvis in 2000 [15]. In the proposed scenario, a funnel-shaped thin shell outflow substitutes the torus and offers the possibility to explain many other features observed in AGN (see Figure 1.11).

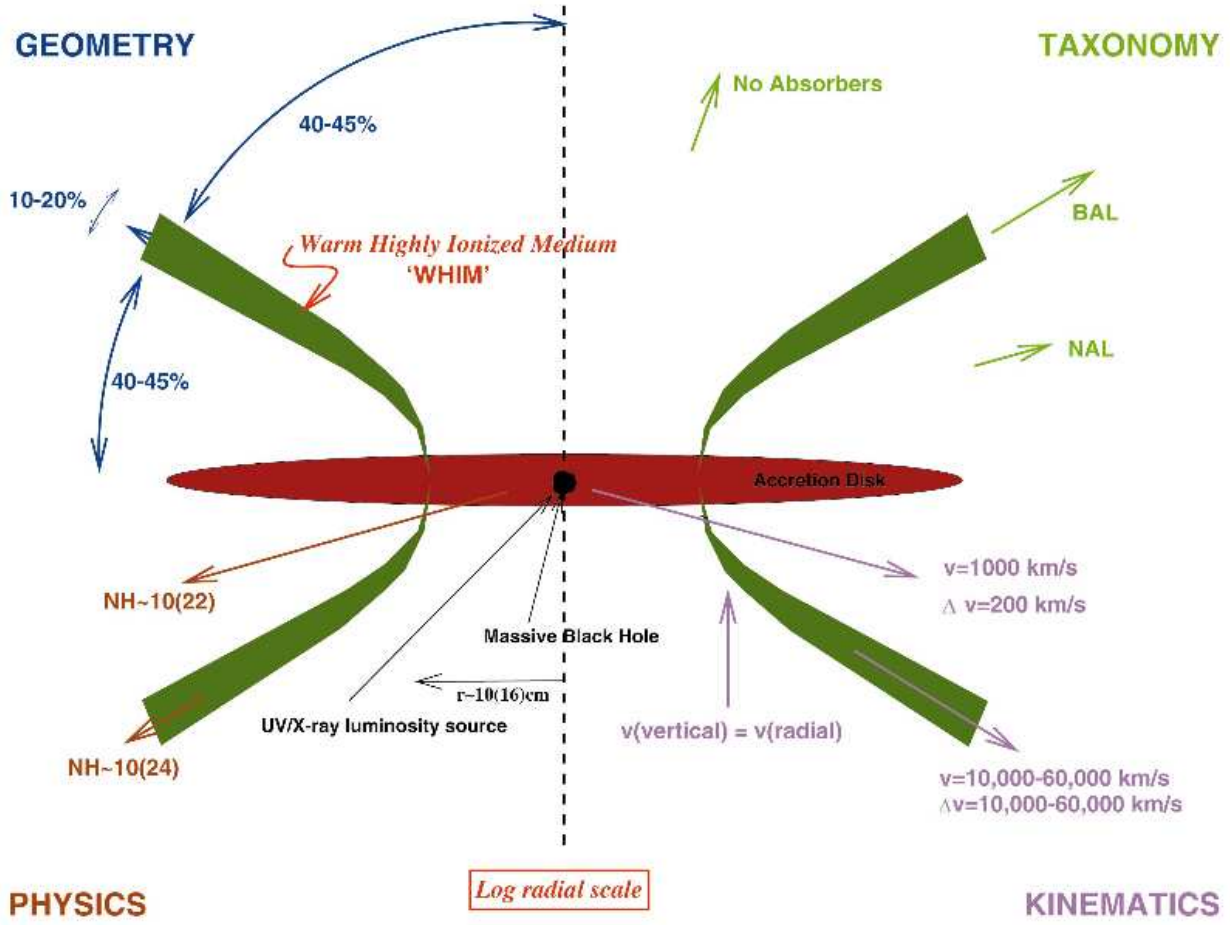

Figure 1.11: *A cartoon depicting the alternative Unification Model proposed by Elvis. The figure is divided in four quadrants which illustrate (clockwise from top left): the geometrical angles involved in the structure, the resulting classification for a distant observer, the outflow velocities for each line of sight and typical radii and column densities. (from Elvis, 2000)*

1.2 X-ray Binaries

The trivial definition of X-ray Binaries (XRBs) is that they are binary systems emitting X-rays. However it has been largely demonstrated that X-ray binary systems emit energy in IR, Optical, UV, X-ray, Gamma-Ray and sometimes they show also a valuable radio emission. In 1934, Baade and Zwicky first suggested that the supernova was the result of the transition from normal star to a neutron star. During the process the energy release is comparable to the change in gravitational potential energy of a star which collapse from its normal size of $\sim 10^6\,Km$ down to the size of a neutron star of $\sim 10\,Km$. The discovery of the first extra-solar X-ray source, Sco X-1, (Giacconi et al. 1962 [27]) accelerated the studies on neutron stars. From that moment, the challenge of X-ray astronomy started and the knowledge of X-ray sources quickly evolved during these last four decades, thanks to a multitude of space-based X-ray experiments on board rockets, stratospheric balloons and satellites.

As for AGN, the family of X-ray binaries is quite vast and varied. The common trait is the engine producing the huge release of energy, which is still the accretion. In this case the material comes from the companion star (the secondary star) of the binary system and accrete onto the compact object (the primary star) which can be a neutron star, a black hole or a white dwarf. In Figure 1.12 the famous sketch by Remillard and McClintock [61] shows the 16 confirmed and largely observed BH binaries in the Milky Way at that time. As one can see at a first look, their diversity is evident.

1.2.1 Classification of X-ray Binaries

X-ray Binary systems can be divided in different sub-classes. A first criterion is based on how the matter flow through the compact object. If the secondary star fills its Roche lobe, see Figure 1.13, the matter flows through the first Lagrangian point and, approaching the primary star, forms an accretion disc around it because of conservation of angular momentum. If the secondary is contained within its Roche lobe, the matter accretes onto the primary via stellar wind.

The 'High Mass X-ray Binaries' (HMXBs) belong to this second class (stellar wind accretion) and are characterized, as the name suggests, by a massive companion star with $M \gg 1M_{\odot}$. They can be further divided in two sub-classes: 'Hard X-ray Transient Sources' (HXTSs) and 'Permanent X-ray Sources' (PXSs). The optical counterparts of HXTSs are usually main-sequence stars (luminosity class between V and III) with quite eccentric orbits ($0.2 \leq e \leq 0.5$) and orbital period $P_{orb} > 10\,d$. Their hard X-ray

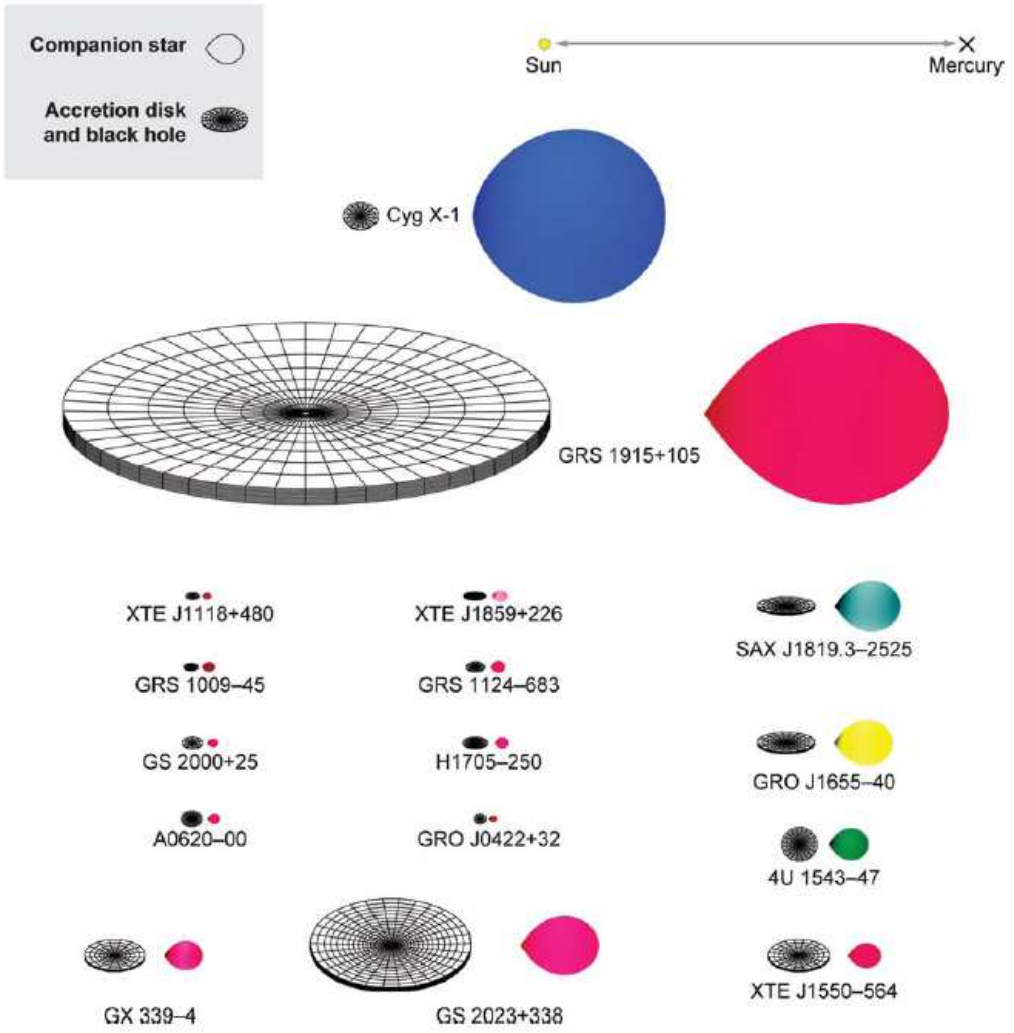

Figure 1.12: *Scale drawings of 16 black-hole binaries in the Milky Way (courtesy of J. Orosz). The Sun-Mercury distance (0.4 AU) is shown at the top. The estimated binary inclination is indicated by the tilt of the accretion disk. The color of the companion star roughly indicates its surface temperature.*

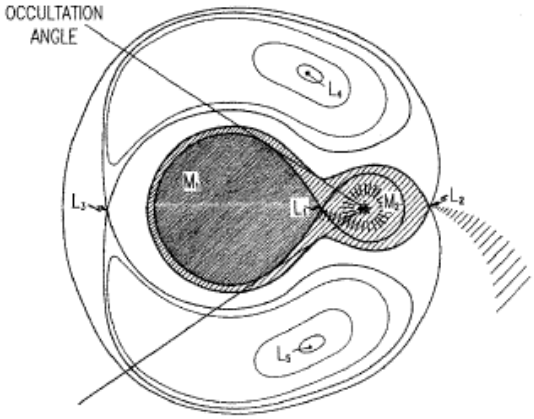

Figure 1.13: *Roche lobes and equipotential surfaces of a binary system formed by a normal star M1 and a compact collapsed companion M2. L1, L2, L3, L4 and L5 are the Lagrange points of the system (Ruffini, 1975).*

emission ($\gtrsim 17\,keV$) is extremely variable with a ratio between maximum and minimum luminosity of the order $L_{Xmax}/L_{Xmin} > 10^2$. With the sensitivities of the first generation detectors, they were not always detectable and this is the reason for their name. The optical counterparts of PXSs are usually OB supergiant stars (luminosity class I) with orbits almost circular ($e \sim 0$) and periods $P_{orb} < 10\,d$. Their hard X-ray emission is approximately constant.

In the 'Low Mass X-ray Binaries' (LMXBs) the optical companion is a late-type star with $M \leq 1M_{\odot}$ which accretes onto the compact object by Roche lobe overflow. They are often found in globular clusters and populate the Galactic Bulge while the HMXBs are more concentrated towards the Galactic Plane and show clear signature of the spiral structure in their spatial distribution (see Figure 1.14).

Other sub-classes of XRBs exist. Among them, the most famous and studied are the 'Cataclysmic Variables' (CVs) in which the optical companion is a low-mass-late-type star and the compact object is a White Dwarf. More exotic XRBs includes the 'Anomalous X-ray Pulsars' and the 'RS Canum Venaticorum' type systems.

1.2.2 X-ray light curves and SED

As we said at the beginning of this chapter, AGN are variable objects and XRBs share the same feature. Recent works (see, e.g. Uttley et al. 2005

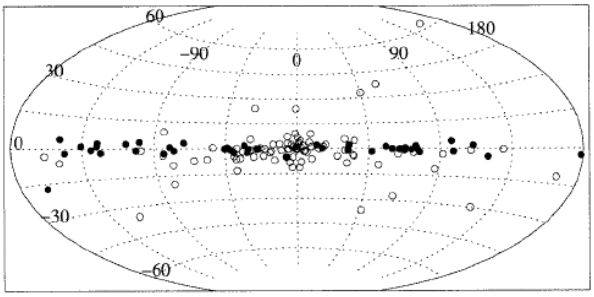

Figure 1.14: *Distribution of HMXBs (filled circles) and LMXBs (open circles) in the Galaxy. In total 52 HMXBs and 86 LMXBs are shown. Note the significant concentration of HMXBs towards the Galactic Plane and the clustering of LMXBs in the Galactic Bulge (Grimm, Gilfanov and Sunyaev 2002).*

[78]) seem to suggest that the process underlying the variability is the same but scaled for the masses, in timescales. In Figure 1.15 X-ray light curves for an AGN and a BHB are shown. The amplitude and modulation of variation is quite similar for both the sources, apart from the timescales. For this

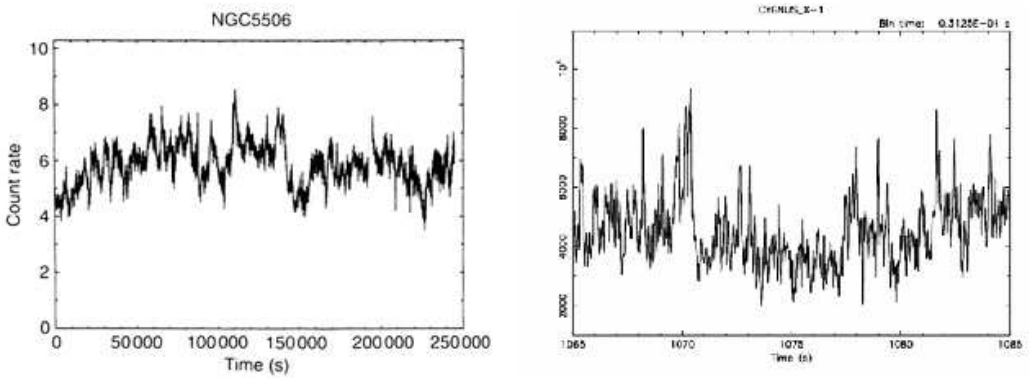

Figure 1.15: *X-ray light curves for the Seyfert 2 galaxy NGC5506 (left panel) and the well-known X-ray Binary Cygnus X-1 (right panel). The amplitude and the pattern of the variation is quite similar apart from the timescales: the variation measured on a timescale of* $\sim 10^5$ *seconds for the AGN, is similar on a timescale of few tens of seconds for the XRB.*

reason, studies on X-ray variability on nearby galactic BHs allow to better understand the origin of this phenomenon.

Nearly all the BHBs are X-ray novae that are discovered when they first go into outburst. In the past decade the large-area timing detector aboard the 'Rossi X-ray Timing Explorer' (RXTE) allowed to study this transient

phenomena and to obtain the light curves shown before. For X-ray outburst that last between ~ 20 days and many months, the generally accepted cause of the outburst cycle is an instability that arises in the accretion disk. When the accretion rate from the donor star is not sufficient to support continuous viscous flow to the compact object, matter fills the outer disk until a critical surface density is reached and an outburst is triggered. This model predicts recurrent outbursts; indeed, half of the BHBs are now known to recur on timescales of 1 to 60 years (Remillard and McClintock 2006 [61]). Outbursts on much shorter or longer timescales do occur, but these are not understood in terms of the disk instability model. Sources such as GRS 1915+105 and 4U 1755-338 exhibit 'on' and 'off' states that can persist for $\gtrsim 10$ years. The behavior of the companion star may play a role in causing these long-term changes in the accretion rate. An important analysis tool for studying the rapid variaitons in X-ray intensity is the 'Power-Density Spectrum' (PDS) which describes how the power of a signal (function of time) is distributed with frequency. The continuum power in the PDS is of interest for both its shape and its integrated amplitude (e.g., $0.1 - 10\,Hz$), which is usually expressed in units of rms fluctuations scaled to the mean count rate. PDSs of BHBs also exhibit transient, discrete features known as 'Quasi-Periodic Oscillations' (QPOs) that may range in frequency from 0.01 to $450\,Hz$ and are generally modeled with Lorentzian profiles.

It has been known for decades that the energy spectra of BHBs often exhibit a composite shape consisting of both a thermal and a nonthermal component. Furthermore, BHBs display transitions in which one or the other of these components may dominate the X-ray luminosity. The thermal component is well modeled by a multitemperature blackbody, which originates in the inner accretion disk and often shows a characteristic temperature near $1\,keV$ (in the next Chapter the physics of accretion disc will be treated in more detail). The non-thermal component is usually modeled as a power law (PL). It is characterized by a photon index Γ, where the photon spectrum is $N(E) \propto E^{-\Gamma}$. The PL generally extends to much higher photon energies than does the thermal component, and sometimes the PL suffers a break or an exponential cutoff at high energy. X-ray spectra of BHBs may also exhibit an $Fe\,K_\alpha$ emission line that is often relativistically broadened.

Emission states of BHBs

The concept of X-ray states was born when Tananbaum and collaborators, in 1972 [72] observed a global spectral change in Cyg X-1 in which the soft X-ray flux ($2 - 6\,keV$) decreased by a factor of 4, the hard flux ($10 - 20\,keV$) increased by a factor of 2, and the radio counterpart turned on. Thereafter,

a similar X-ray transition was seen in A 0620-00 (Coe et al. 1976 [9]) and in many other sources as well. The soft state, which was commonly described as $\sim 1\,keV$ thermal emission, was usually observed when the source was bright, thereby prompting the name 'high/soft state'. The hard state, with a typical photon index $\Gamma \sim 1.7$, was generally seen when the source was faint, hence the name 'low/hard state'. In this state, the disk was either not observed above $2\,keV$ or it appeared much cooler and withdrawn from the BH. An additional X-ray state of BHBs was identified in the Ginga era. It was characterized by the appearance of several-Hz X-ray QPOs, a relatively high luminosity (e.g., $> 0.1 L_{Edd}$), and a spectrum comprised of both a thermal component and a PL component that was steeper ($\Gamma \sim 2.5$) than the hard PL. This state was named the 'very high' state. During this period, Gamma-ray observations ($\sim 40-500\,keV$) of seven BHBs brought clarity to the distinction between the soft and hard types of X-ray PL components (Grove et al. 1998 [28]; Tomsick et al. 1999 [73]). Sources in the low/hard state ($\Gamma \sim 1.7$) were found to suffer an exponential cutoff near $100\,keV$, whereas sources with soft X-ray spectra ($\Gamma \sim 2.5$) maintained a steep, strong, and unbroken PL component out to the sensitivity limit of the gamma-ray detectors ($\sim 1\,MeV$). More recently, radio observations have cemented the association of the low/hard state with the presence of a compact and quasi-steady radio jet see Fender 2005 [20] ; McClintock and Remillard 2006 [48]).

In Figure 1.16, the character of each state is illustrated by showing examples of PDSs and energy spectra for the BHB GRO J1655-40 (from [48]). The relevance of X-ray states fundamentally rests on the large differences in the energy spectra and PDSs that can be seen in a comparison of any two of these states.

In the thermal state (also known as high/soft state), the flux is dominated by the thermal radiation from the inner accretion disk, the integrated power continuum is faint, and QPOs are absent or very weak. There is usually a second, nonthermal component in the spectrum, but its contribution is limited to $< 25\%$ of the flux at $2 - 20\,keV$. The state is illustrated in the middle row of panels in Figure 1.16. The spectral deconvolution shows that the thermal component (red line) is much stronger than the PL component (blue, dashed line) for $E \leq 10\,keV$. The PDS (right panel) appears featureless. The hard state (also known as low/hard state) is characterized by a hard PL component ($\Gamma \sim 1.7$) that contributes $\geq 80\%$ of the $2-20\,keV$ flux. The power continuum is bright with rms power (PDS integrated from $0.1 - 10\,Hz$) > 0.1 and QPOs may be either present or absent. A hard state osbervation of GRO J1655-40 is shown in the bottom row of panels in Figure 1.16. The accretion disk appears to be faint and cool compared to the thermal state. As noted previously, the hard state is associated with

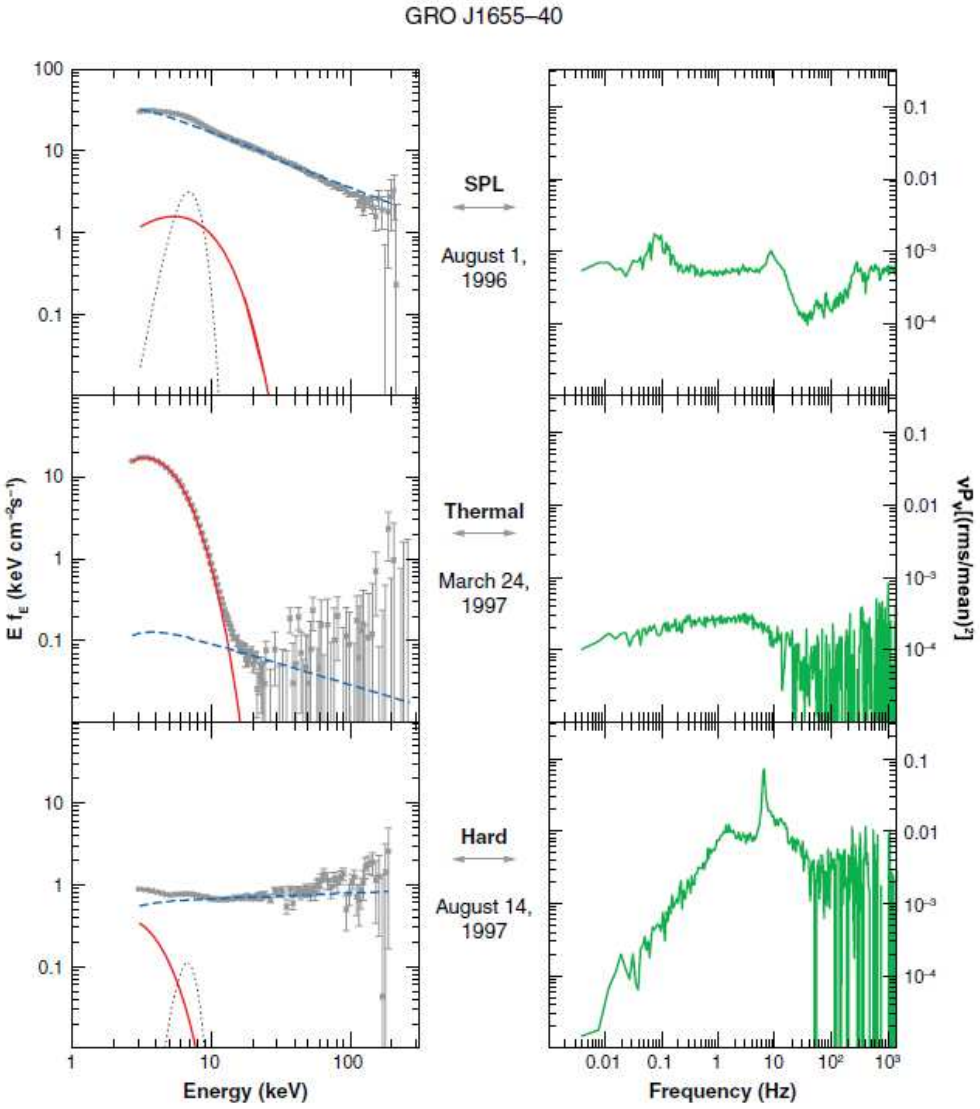

Figure 1.16: *Sample spectra of black-hole binary GRO J1655-40 illustrating the three outburst states: steep power law, thermal, and hard. Each state is characterized by a pair of panels. Left panels show the spectral energy distribution decomposed into three components: thermal (red, solid line), power-law (blue, dashed line), and a relativistically broadened Fe K_α line (black, dotted line). Right panels show the PDSs plotted as $log(\nu \times P_\nu)$ versus $log(\nu)$ (from McClintock and Remillard, 2006 [48])*

the presence of a quasi-steady radio jet, and clear correlations between the radio and X-ray intensities are observed. As said previously, the hallmark of the SPL state is a strong PL component ($\Gamma \sim 2.5$) and characterized by the presence of a sizable thermal component and the frequent presence of X-ray QPOs. An example of the SPL state is shown in the top row of panels in Figure 1.16. There are similarities between the SPL state and the thermal state; both show a thermal component and a steep PL component. However, in the thermal state the PL is faint and has a more variable photon index, while the SPL state is plainly distinguished by its powerful PL component and the commonly-occurring QPOs. The SPL state tends to dominate BHB spectra as the luminosity approaches the Eddington limit, and it is this state that is associated with high-frequency QPOs (HFQPOs). Intermediate states and state transitions are another important aspect of BHB studies. The three states defined before represent an attempt to define spectral and timing conditions that are quasi-stable and that appear to have distinct physical origins.

For the thermal state there is a satisfactory paradigm, namely, thermal emission from the inner regions of an accretion disk. For a detailed explanation on the emission from an accretion disc we refer the reader to Chapter 2.

The association of the hard state with the presence of a steady radio jet marked a substantial advance. However, the relationship between the disk and jet components and the origin of the X-ray properties of the hard state remain uncertain. Using simultaneous HST, EUVE, and Chandra observations (McClintock et al. 2001 [49]), the disk was found to be unusually large ($\sim 100\, r_g$) and cool ($\sim 0.024\, keV$).Though it seems clear that the blackbody radiation is truncated at a large radius, the physical condition of material within this radius remains uncertain. Alternative scenarios include a thermal 'advection-dominated accretion flow' (ADAF; Esin et al. 2001 [16]), a radiative transition to synchrotron emission in a relativistic flow that is entrained in a jet (Markoff, Falcke and Fender 2001 [41]), and a radiative transition to a Compton corona (Frontera et al. 2003 [23]), which must then be sufficiently optically thick to mask the $\sim 1\, keV$ thermal component normally seen from the disk. Such a corona might be a hot wind leaving the disk (Blandford and Begelman 1999 [46], 2004[47]).

The physical origin of the SPL state remains one of the outstanding problems in high-energy astrophysics. It is crucial that we gain an understanding of this state, which is capable of generating high frequency QPOs, extremely high luminosity, and spectra that extend to $\geq 1\, MeV$. Most models for the SPL state invoke inverse Compton scattering as the operant radiation mechanism (see Zdziarski and Gierlinski 2004 [81]). The MeV photons suggest

that the scattering occurs in a nonthermal corona, which may be a simple slab operating on seed photons from the underlying disk (e.g., Zdziarski et al. 2005 [82]). Efforts to define the origin of the Comptonizing electrons have led to models with more complicated geometries and with feedback mechanisms, such as flare regions that erupt from magnetic instabilities in the accretion disk (Poutanen and Fabian 1999 [55]). An analysis of extensive RXTE spectral observations of GRO J1655-40 and XTE J1550-564 shows that as the PL component becomes stronger and steeper, the disk luminosity and radius appear to decrease while the temperature remains high. These results can be interpreted as an observational confirmation of strong Comptonization of disk photons in the SPL state (Kubota and Makishima 2004 [34]).

The unified model for Radio Jets

Many researchers investigate the spectral evolution of BHBs using a hardness intensity diagram (HID), which is a plot of X-ray intensity versus a 'hardness ratio' (HR), i.e., the ratio of detector counts in two energy bands (e.g.,Homan et al. 2001 [32], Belloni 2004 [4], van der Klis 2006 [79]). This diagram is widely used in tracking the behavior of accreting neutron stars. Compared to the spectral-fitting approach described above, the HID approach has the advantage that it is model independent and the disadvantage that it is difficult to relate the results to physical quantities. Interpretations of variations in the HID depend on the particular energy bands chosen to define HR in a given study. If both bands are above $\sim 5\,keV$, then the HR value effectively tracks the slope of the PL component (i.e., lower HR means a steeper PL). Softer energy bands admit a mixture of thermal and nonthermal components, and interpretations are then more complicated. The HID is also used in illustrating the 'unified model for radio jets' proposed by Fender, Belloni and Gallo (2004) [19]. Figure 1.17 shows their schematic for the relationships between jets and X-ray states, where the state of an observation is distinguished simply by the value of HR.

The figure shows qualitatively how the jet Lorentz factor (lower panel) and the morphology of the jet (sketches i-iv) evolve with changes in the X-ray state. Tracks for state transitions of an X-ray source in the HID are also shown (top panel). The solid vertical line running through both panels in Figure 1.17 is the 'jet line'. To the right of the jet line the X-ray spectrum is relatively hard and a steady radio jet is present, and to the left the spectrum is soft and the jet is quenched. The jet line also marks an instability strip where violent ejections of matter may occur (see sketch iii), as indicated by the spike in the Lorentz factor (lower panel). The tracks for state evolution in the HID are influenced by observations of GX 339-4 (Belloni et al. 2005 [5]).

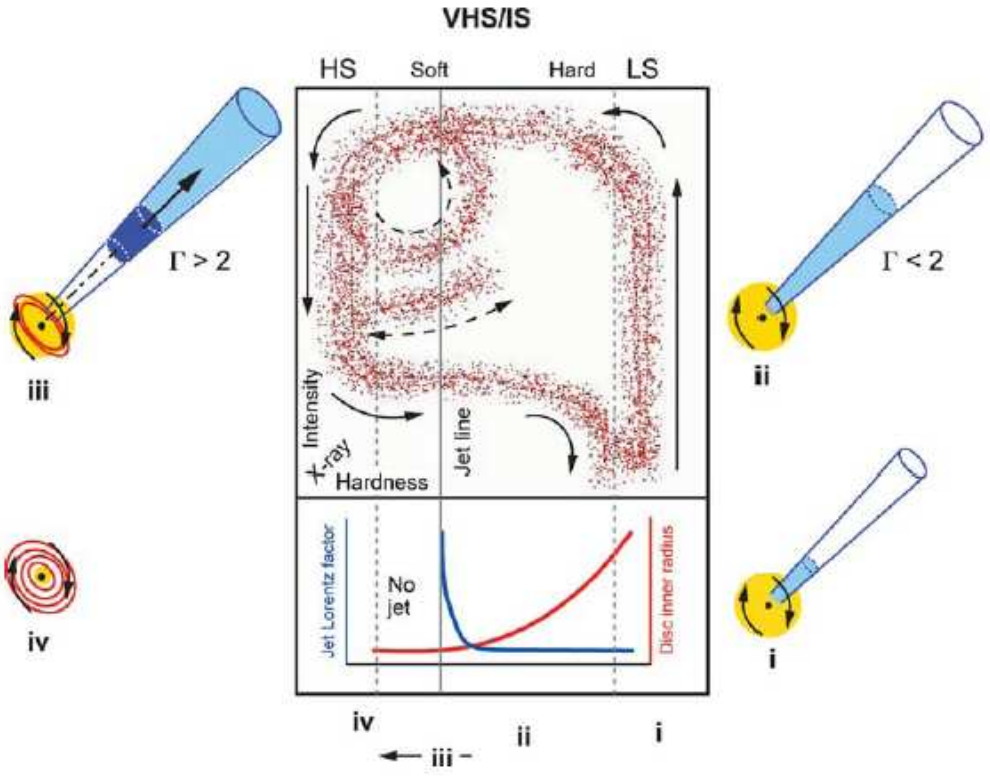

Figure 1.17: *A schematic representation of the model for disk-jet coupling in black-hole binaries from Fender, Belloni and Gallo (2004). The top panel shows evolutionary tracks in a HID, which is a plot of X-ray intensity versus X-ray hardness. (These quantities increase upward and to the right, respectively.) The bottom panel gives a qualitative impression of how the jet's bulk Lorentz factor (blue curve) and the inner disk radius (red curve) vary with X-ray hardness. The X-ray states are labeled at the top in the old nomenclature (i.e., HS=high/soft state, VHS/IS=very high and intermediate states, and LS=low/hard state).*

In this study HR was defined as the ratio of source counts at $6.3 - 10.5\,keV$ to the counts at $3.8 - 7.3\,keV$. The vertical source track on the right side of the figure corresponds to the low/hard or hard state with HR > 0.8 in the case of GX 339-4. The vertical track on the far left (and most observations of GX 339-4 with HR < 0.2) are in the high/soft or thermal state. For the intermediate values of HR, which fall between the dashed lines, the states are described differently. The states in this region are further divided into 'soft intermediate' and 'hard intermediate' states, based on the HR values and the properties of the power continuum in the X-ray PDS. This completes a description of the four X-ray states defined in the unified jet model. The unified model for X-ray states and radio jets provides opportunities to study the disk-jet coupling explicitly, and the HID format is very easy to apply to observations. We refer any other detail on HID studies to the enlightening and updated review by Dunn, Fender and collaborators (2010) [13].

Chapter 2

Accretion

Accretion is a common mechanism in astrophysics and, due to its peerless efficiency it is the only one able to power the most luminous objects in the Universe. Accretion can take place in different ways and the final result depends on many factors like the geometry of the system, the presence of a magnetic field, the optical depth of the accreting material, and so on. The simplest model of accretion was developed in the 50s by Bondi and is based on spherical accretion approximation. Although instructive, this model does not find practical application because accreting material always have some angular momentum that breaks spherical symmetry and especially does not work with objects without a solid surface, like black holes. The right symmetry we need to consider is the cylindrical one, with matter orbiting around the central compact object and forming an accretion disk.

From the point of view of energetics the question is very simple. By the law of conservation of energy, a portion of gas with mass m falling on a compact object with mass M and radius R, satisfies

$$\frac{1}{2}mv_{ff}^2 = \frac{GMm}{R} \tag{2.1}$$

Assuming that all of the energy is converted into radiation

$$E_{tot} = \frac{1}{2}mv_{ff}^2 = \frac{GMm}{R} = E_{rad} \tag{2.2}$$

Differentiating the previous equation we get the luminosity

$$L = \frac{dE_{rad}}{dt} = \frac{dU}{dt} = \frac{GM}{R}\frac{dm}{dt} = \frac{GM\dot{m}}{R} \tag{2.3}$$

Therefore luminosity is proportional to the accretion rate, $\dot{m}$, and to the compactness, $\left(\frac{M}{R}\right)$, and that is the reason why accretion is so efficient for

collapsed objects like black holes. Indeed, recalling equation (1.3) and the definition of 'Schwarzschild radius', efficiency can be written as

$$\begin{aligned} R_S &\equiv 2\frac{GM}{c^2} \Rightarrow L = \frac{1}{2}\left(\frac{R_S}{R}\right)\dot{m}c^2 = \eta\dot{m}c^2 \Rightarrow \\ \Rightarrow \eta &= \frac{1}{2}\left(\frac{R_S}{R}\right) \end{aligned} \tag{2.4}$$

Obviously not all of the energy is transformed into radiation, hence the previous equation represents an upper limit to the efficiency. In equation (1.4), for black holes, we can replace R with the last stable orbit radius R_{lso} which is $R_{lso} = 3R_S$ for non-rotating BHs and $R_{lso} \simeq R_S/2$ for maximally rotating ones, obtaining

$$\begin{aligned} \eta(a=0) &= \frac{1}{6} \backsimeq 0.16 \\ \eta(a \sim M) &\simeq \frac{1}{2} = 0.5 \end{aligned}$$

where $a \in [0, M)$ is the adimensional spin of the black hole. Actually we cannot neglect relativistic effects and we should solve the entire calculus in Schwarzchild metric for a non-rotating BH and in Kerr metric for a rotating one, obtaining

$$\begin{aligned} \eta(a=0) &\backsimeq 0.057 \\ \eta(a \sim M) &\backsimeq 0.42 \end{aligned} \tag{2.5}$$

A maximally rotating black hole forces the surrounding portion of space-time to co-rotate with it, allowing matter to reach a radius three times smaller than in the case of a Schwarzchild black hole, and bringing to an efficiency of an order of magnitude larger.

The main problem with accretion is to find a clear way to let the gas loose angular momentum (considering that the system is isolated) and to convert gravitational energy into radiation. In a classical approach, both problems are resolved invoking viscosity forces between disk annuli, originated by the differential disk rotation. The nature of this mechanism is still under debate, but useful results can be obtained confining all the uncertainties about kinematic viscosity arising from turbulent motions in a dimensionless parameter α (the so called 'α-prescription') as proposed by Shakura and Sunyaev in 1973 [68]. Leaving the details to the beautiful review by Pringle in 1981 [60] we will briefly describe the main concepts behind Shakura and Sunyaev approach showing the most important equations and results.

The first problem to solve is the angular momentum loss: the idea is that viscosity forces act to decrease velocity difference between annuli. If we consider only two annuli, the outermost slows his neighbor down letting it lose rotational kinetic energy and letting it fall in the potential well produced by the black hole. At the same time the angular momentum is transferred to the outer part of the disk. Since the last stable orbit is circular, and assuming that gas can radiate efficiently[1], the falling material will form a thin accretion disk.

Let us consider an annulus at radius R with surface mass density Σ, orbiting with Keplerian angular velocity[2] around the BH. By making use of mass conservation (continuity equation) and angular momentum conservation, it is possible to obtain a differential equation that describes how Σ varies with radius

$$\frac{\partial \Sigma}{\partial R} = \frac{3}{R} \frac{\partial \left\{ \sqrt{R} \frac{\partial \left(\nu \Sigma \sqrt{R} \right)}{\partial R} \right\}}{\partial R} \tag{2.6}$$

Generally, kinematic viscosity ν is a function of local properties of the disk like Σ, R and t (time) and therefore Eq.(1.6) is a non-linear (and not analytically solvable) diffusion equation for the surface density Σ. Instead, assuming ν as constant, Eq.(1.6) can be solved and $\Sigma(R,t)$ can be written in an integral form using the Bessel function $J_{\frac{1}{4}}$.

In Figure 2.1 the time evolution of a disk annulus is shown. When $t = 0$ the whole mass is confined around R_0 and $\Sigma_0(t_0) = \delta(R - R_0)$; then, as time goes by, viscosity forces cause the energy loss and the gas flows toward $R = 0$ while a small fraction moves outward carrying the angular momentum and guaranteeing the conservation.

In order to obtain a complete description of our accreting annulus, we should solve Navier-Stokes equations considering all forces involved (gravitational, centrifugal and viscous) and, as previously, we would have to do with the 'viscosity uncertainty'. In their enlightening paper[68] Shakura and Sunyaev, by making use of the thin disk approximation, were able to find an easy-to-handle expression for viscosity. Adopting the 'steady disk' approximation (i.e. $\dot{m} = const$), which is satisfied in many situations of astrophysical interest, they were capable of achieve a simple expression for the rate of energy dissipated by one side of the disk

[1] Time scale for viscous processes, responsible for angular momentum redistribution, is larger than radiative and dynamic (orbital) time scale

[2] $\Omega = \sqrt{\frac{GM}{R^3}}$

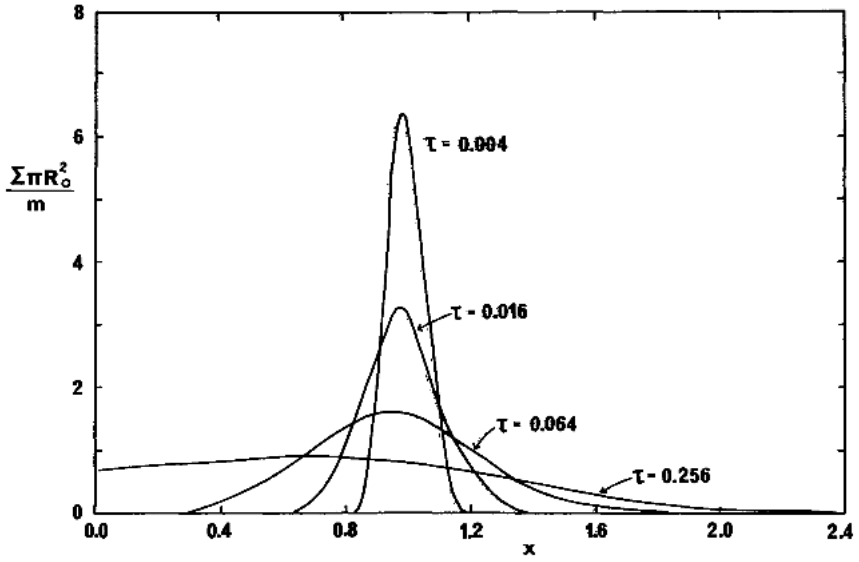

Figure 2.1: *The viscous evolution of a ring of matter of mass m. The surface density Σ is shown as a function of dimensionless radius $x = \frac{R}{R_0}$, where R_0 is the initial radius of the ring, and dimensionless time $\tau = 12\frac{\nu t}{R_o^2}$ where ν is the viscosity. (from Shakura & Sunyaev, 1973)*

$$\dot{Q} = \frac{3GM\dot{m}}{8\pi R^3}\left(1 - \sqrt{\frac{R_0}{R}}\right) \tag{2.7}$$

Assuming that the dissipated energy is entirely converted into radiation, the total luminosity of the disk is simply

$$L = \int_{R_0}^{\infty} 2\left(-\dot{Q}\right) \cdot 2\pi R dR = \frac{1}{2}\frac{\dot{m}GM}{R_0} \tag{2.8}$$

where R_0 is now the inner radius of the disc, often assumed to be coincident with the ISCO[3]. Thus, during radial motion, half of the liberated potential energy goes into increasing the kinetic energy and half goes into heat and then into radiation. In order to obtain the emission spectrum we should be able to predict the emission from any part of the disk and than integrate over the whole surface or, in other words, we should solve the radiative transfer

[3]The ISCO is the 'Innermost Stable Circular Orbit' which is also called 'Last Stable Orbit' and it is equal to $3R_S$ for non-rotating BHs and $\simeq R_S/2$ for maximally rotating ones. The accretion disc, in general, can be truncated even far before the ISCO, depending on the accretion rates and other parameters. Nonetheless, approximate the inner radius with the ISCO is quite common and we adopted this simplification as well.

equation for any radius. However, if the disk is optically thick, every part emits like a black body with its radius-dependent temperature $T(R)$ and, from the Stefan-Boltzmann law, the energy flux density is

$$U = \sigma_{SB} T(R)^4 \tag{2.9}$$

As for the steady disk approximation, the optically thick disk approximation extremely simplifies the problem. Equating (1.7) with (1.9) we get the temperature at each radius

$$\dot{Q} = U \Rightarrow$$

$$\Rightarrow T(R) = \left[\frac{3GM\dot{m}}{8\pi R^3 \sigma_{SB}} \left(1 - \sqrt{\frac{R_0}{R}} \right) \right]^{\frac{1}{4}} \tag{2.10}$$

We can define a characteristic temperature $T_\star$

$$T_\star = \left[\frac{3GM\dot{m}}{8\pi R_{min}^3 \sigma_{SB}} \right]^{\frac{1}{4}} \tag{2.11}$$

For AGN, $T_\star$ is around $10^5 K$ which correspond to an emission peaked in the UV band, while for galactic black holes it is around $10^7 K$ with an emission peaked in the soft X-rays. At smaller radii the temperature increases up to the maximum value $T_{max} = 0.49\, T_\star$ which correspond to a radius $R_{hot} = \frac{49}{36} R_{min}$. For radii smaller than R_{hot} the temperature decreases to an unphysical value of zero.

The overall spectrum is the sum on the entire disk surface of the single black body radial dependent emission

$$S_\nu \propto \int_{R_0}^{R_{out}} B_\nu T(R)\, 2\pi R dR \tag{2.12}$$

where R_{out} is the outer radius of the disk and B_ν the Planck photon distribution.

$$B_\nu(T(R)) = \frac{2\, h\, \nu^3}{c^2} \frac{1}{e^{\frac{h\,\nu}{k_B\, T(R)}} - 1} \tag{2.13}$$

The spectrum, shown in Figure 2.2, is the so-called 'multi-temperature black body'. At low frequencies the emission is due to the outer and cooler (T_{out}) part of the disk and the spectrum follows the typical $S_\nu \propto \nu^2$ Rayleigh-Jeans tail; the Planck exponential cut-off is clearly visible at high frequencies, while in the middle the characteristic $S_\nu \propto \nu^{\frac{1}{3}}$ trend for accretion spectra can be seen.

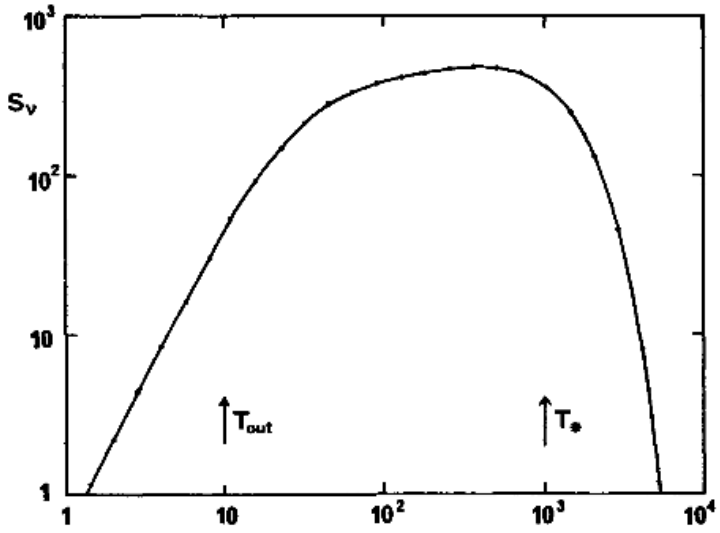

Figure 2.2: *Integrated spectrum of a steady, geometrically thin and optically thick accretion disk. The units are arbitrary but the frequencies corresponding to T_{out} and T_* are labelled. (from Shakura & Sunyaev, 1973)*

The accretion model of geometrically thin and optically thick disk we have just considered fits quite well the AGN case. α-discs represents the 0th-order of accretion discs description. As can be easily figured out, there is a vast literature on accretion physics and a lot of different model (one need only to consider all the combination between geometrically thin/thick and optically thin/thick conditions). The description of these discs is out of the purpose of this work. We just want to mention, among all the models, the 'Advection Dominated Accretion Flows' (ADAF) accretion model[4]. In ADAF models the accretion rate is so low that the surface mass density of the disk is not high enough to keep ions and electrons thermally coupled via Coulomb interactions. As a consequence, the energy associated to ions, which are poor radiators, cannot be locally emitted and it is advected togheter with the accretion flow beyond the black hole event horizon. Therefore a large fraction of the available energy turns into internal energy and the gas becomes hot and optically thin, with a very low radiative efficiency. Great attention has been focused on ADAF models thanks to their success in explaining the emission from the Galactic Center (see Narayan et al. 1995 [51]).

The optically thick disc acts like the optically thick atmosphere of a star. As stated by Chandrasekhar in 1960 [7], the limb darkening effect should

[4]ADAFs are a subclass of 'Radiatively-Inefficient Accretion Flows' (RIAF) disks, characterized by a sub-Eddington accretion rate that brakes down radiative efficiency

be considered in the pure scattering atmosphere approximation. Photons emitted almost parallel to the plane of the disc are less than the ones emitted perpendicularly but can be linearly polarized up to $\sim 12\%$,

For Chandrasekhar limb darkening effect, the analytical expression in [36] represent a good approximation

$$F(\mu) = 1 + a\,\mu \tag{2.14}$$

where μ is the cosine of the polar angle ($\mu = cos(\Theta)$) measured from the axis normal to the disc surface, F is the flux and $a = 2.06$ in an optically thick electrons' atmosphere.

The initial polarization degree for a given μ is taken from Table XXIV in [7]. For perpendicularly arising photons, $\Theta = 0°$, the initial linear polarization degree is 0% while for parallel seed photons, $\Theta = 90°$, it reaches the value of 11.7%. In Figure 2.3 we show the degree of polarization for unscattered photons generated by an optically thick disc as a function of μ. The plot is obtained by summing the contributions of unscattered photons and hence represents the polarization due only to the optically thick atmosphere of the disc. Photons emitted almost parallel to the disc ($\mu = 0$) show the maximum degree of polarization which is exactly 11.7%.

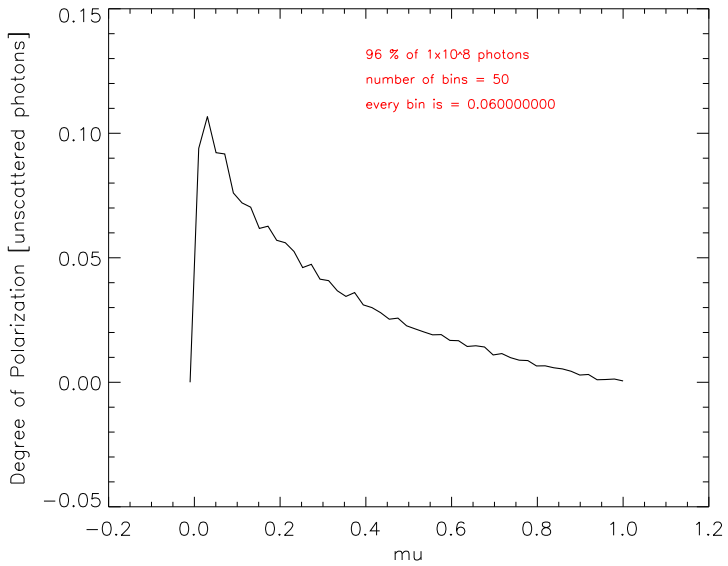

Figure 2.3: *The plot is obtained by calculating and binning the degree of polarization for the photons escaped without any scattering during a simulation which in this case are the* 96% *out of* 10^8 *photons.*

Chapter 3

Comptonization

Soon after the development of quantum mechanics, Artur Holly Compton discovered, in 1923, the Compton effect, an inelastic scattering between a photon and a charged particle, earning the Nobel Prize in 1927. The effect is important because demonstrates that light cannot be treated as a wave in the high energy regime (i.e. when $\epsilon = h\nu$ is comparable with the rest energy of the charged particle $E = mc^2$). Due to conservation of mass-energy and momentum, part of the photon's energy is given to the charged particle (from now on we consider an electron), which recoils, and the photon is emitted at a different direction and with a different wavelength. The classical limit of Compton scattering is the elastic Thomson scattering:

$$\begin{aligned} \epsilon &= \epsilon_1 \\ \frac{d\sigma_T}{d\Omega} &= \frac{1}{2} r_0^2 \left(1 + \cos^2\theta\right) \\ \sigma_T &= \frac{8\pi}{3} r_0^2 \end{aligned} \tag{3.1}$$

The emitted photon has the same energy of the incident one (first equation). The angular distribution of scattered photons is modulated by the cosine of the scattering angle[1] θ, as shown in the differential cross-section (second equation). $r_0 = \dfrac{e^2}{m_e c^2} = 2.8 \times 10^{-13} cm$ is the classical radius of the electron. The third equation in (3.1) is the total cross-section.

As the energy of the incident photon (ϵ) increases, quantum effects appears in two ways. First, the scattering will no longer be elastic ($\epsilon_1 \neq \epsilon$) because of the recoil of the particle. By applying energy and momentum

[1]The scattering angle is defined as the angle between the direction of the incident photon and the direction of the scattered one

conservation one can easily obtain (see, e.g. the book by Rybicki and Lightman, 1979 [64]):

$$\epsilon_1 = \frac{\epsilon}{1 + \frac{\epsilon}{mc^2}(1 - \cos\theta)} \tag{3.2}$$

Note that when $\epsilon \ll mc^2$ the scattering is closely elastic ($\epsilon_1 \approx \epsilon$). The second effect is an alteration of the cross-section. The differential cross-section for unpolarized radiation is shown in quantum electrodynamics to be given by the Klein-Nishina formula, who first derived it in 1928:

$$\frac{d\sigma_{KN,U}}{d\Omega} = \frac{r_0^2}{2}\frac{\epsilon_1^2}{\epsilon^2}\left(\frac{\epsilon}{\epsilon_1} + \frac{\epsilon_1}{\epsilon} - \sin^2\theta\right) \tag{3.3}$$

For $\epsilon_1 \sim \epsilon$ equation (3.3) reduces to the classical expression. The principal effect is to reduce the cross section from classical value as the photon energy becomes large. The total cross section can be shown to be

$$\sigma_{KN} = \sigma_T \frac{3}{4}\left\{\frac{1+x}{x^3}\left[\frac{2x\,(1+x)}{1+2x} - ln(1+2x)\right] + \frac{1}{2x}\ln(1+2x) - \frac{1+3x}{(1+2x)^2}\right\} \tag{3.4}$$

where $x \equiv \dfrac{h\nu}{mc^2}$. In the non relativistic regime ($x \ll 1$) we have approximately

$$\sigma_{KN} \approx \sigma_T\left(1 - 2x + \frac{26\,x^2}{5} + \ldots\right) \tag{3.5}$$

whereas for the extreme relativistic regime ($x \gg 1$) we have

$$\sigma_{KN} = \frac{3}{8}\sigma_T\, x^{-1}\left(\ln(2x) + \frac{1}{2}\right) \tag{3.6}$$

In Figure 3.1 the angular distribution for the scattered photon is shown for different incident photon energies. As the energy increases, the back scattering becomes less probable.

For polarized radiation, instead, the azimuthal distribution is no longer isotropic, but is related to the polarization vector of the incident photon. The differential Compton scattering cross section for a free electron at rest in the case of completely polarized incident beam can be written as

$$\frac{d\sigma_{KN,P}}{d\Omega} = \frac{r_0^2}{2}\frac{\epsilon_1^2}{\epsilon^2}\left(\frac{\epsilon}{\epsilon_1} + \frac{\epsilon_1}{\epsilon} - 2\sin^2\theta\cos^2\phi\right) \tag{3.7}$$

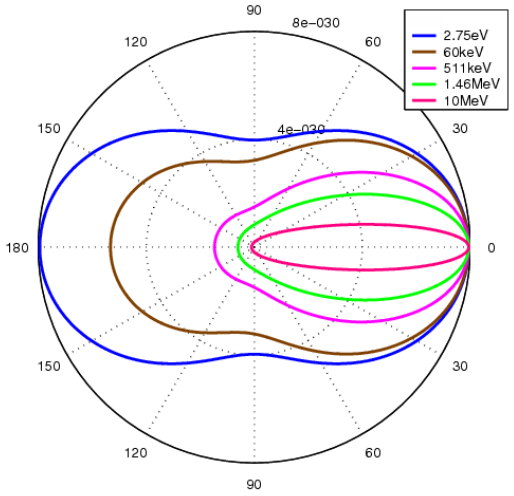

Figure 3.1: *The Klein-Nishina distribution of photon scattering angles over a range of energies. In the transition from optical photons to gamma-ray the back scattering is suppressed.*

where ϕ, the azimuthal scattering angle, is defined as the angle between the polarization unit vector of the incident photon and the plane of scattering (i.e. the plain where the incident photon and the electron lie).

Let us assume that in the rest frame of the electron $h\nu \ll mc^2$, so that the relativistic corrections in the Klein-Nishina formula may be neglected. Whenever the moving electron has sufficient kinetic energy compared to the photon, net energy may be transferred from the electron to the photon, in contrast to the situation indicated in equation (3.2). In such case the scattering process is called 'Inverse Compton'. Let us call K the lab or observer's frame, and let K' be the rest frame of the electron. From Doppler shift formulas, the energies of the incident and scattered photon in the reference frame of the electron are

$$\begin{aligned} \epsilon' &= \epsilon\gamma(1 - \beta\cos\theta) \\ \epsilon_1 &= \epsilon'_1\gamma(1 + \beta\cos\theta'_1) \end{aligned} \tag{3.8}$$

where primed notation indicates quantities in the reference frame of the electron and the angles are those in Fig. 3.2 which shows the scattering event as seen in the two reference frames and γ is the Lorentz factor of the electron

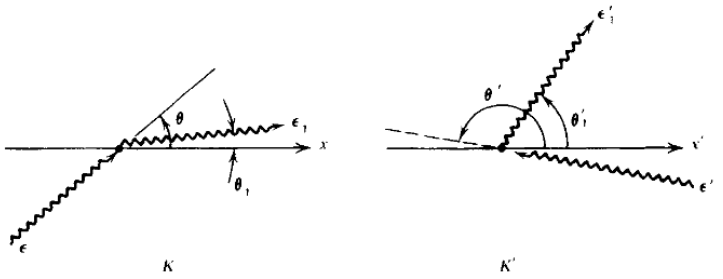

Figure 3.2: *Scattering geometries in the observer's frame K and in the electron rest frame K' (from Rybicki and Lightman [64])*

From equation 3.2 we know that

$$\begin{aligned} \epsilon_1' &\approx \epsilon' \left[1 - \frac{\epsilon'}{mc^2}\left(1 - \cos\Theta\right)\right] \\ \cos\Theta &= \cos\theta_1' \cos\theta' + \sin\theta' \sin\theta_1' \cos(\phi' - \phi_1') \end{aligned} \tag{3.9}$$

where ϕ_1' and ϕ' are the azimuthal angles of the scattered and incident photon in the rest frame of the electron, respectively. In the case of relativistic electrons, $\gamma^2 - 1 \gg h\nu/mc^2$, the energies of the photon before the scattering, in the rest frame of the electron, and after the scattering are in approximate ratios

$$1 : \gamma : \gamma^2$$

providing that the condition for Thomson scattering in the rest frame $\gamma\epsilon \ll mc^2$ is met. This follows from equations (3.7), since θ and θ_1' are characteristically of the order $\pi/2$. This process therefore converts a low-energy photon to a high-energy one by a factor of order γ^2.

These equations are well-known since the first half of the last century. In astrophysics they find many applications since the universe is filled with low-energy radiation (one can just think at the Cosmic Microwave Background, but also the optical photons produced by stars) and matter can exists under extreme condition, i.e. highly ionized and with charged particles accelerated to relativistic speeds. Since then, many physicists applied these equations to solve radiative transfer problems analytically or in approximate forms. Among them, one to be mentioned is with no doubts Subrahmanyan Chandrasekhar who, in his famous book 'Radiative Transfer' (1960) [7], treats Compton scattering in transfer functions, together with many other processes of interest for physics in general. With the advent of computing, a

totally new window opened for theoretical physicists. Thanks to the huge increase in calculus speed and by the use of dedicated methods like Monte Carlo simulations (in the next Chapter we will explain more in detail the basis of this approach) many problems with no analytical solution were dealt with a numerical approach. The pioneers of Monte Carlo approach to Comptonization come from the Russian school (see, e.g. Pozdnyakov et al. 1977 [58] and 1978 [59], the extensive review by Pozdnyakov and Sobol 1983 [57], Sunyaev and Titarchuk 1984 [71]).

In Fig. 3.3 some of the simulations from Pozdnyakov and collaborators showing a Planckian spectrum Comptonized by a weakly relativistic ($kT_e = 0.5\,mc^2$) distribution of Maxwellian electrons (left panel) and the $6.4\,keV$ Iron line emission Comptonized by a cloud of thermal electrons at $kT_e = 1\,keV$.

In all these works, polarization of radiation is not included. Only in Sunyaev and Titarchuk 1984 [71] calculations on the degree of polarization are made, but they are obtained in Thomson regime. In more recent years, after the success obtained with the 'two-phase model' by Haardt and Maraschi 1991 [29], 1994 [30] (see Sec. 1.1.2 and Fig. (1.5)), many other authors developed their own codes in order to study Comptonization with Monte Carlo simulations (see, e.g. Malzac and Jourdain 2000 [40]). Also in these works polarization is usually not included. Only very recently (2009), several missions with X-ray polarimeters on board have been proposed, thanks, mainly, to the new available technology of Gas Pixel Detectors (GPDs) which capabilities for X-ray polarimetry were introduced in 2007 by Bellazzini et al. [3]. Among the latest works on Comptonization which include calculations on polarization we can cite McNamara et al. 2008 [50] and Schnittman and Krolik 2010 [66]. McNamara and collaborators use an approach similar to ours but it is applied on CVs and therefore they do not need relativistic corrections to the Maxwell distribution of electrons and moreover the overall geometry is quite different. White Dwarfs have a strong dipolar magnetic field which forces the matter to flow through columns onto the poles of the compact object instead of forming an accretion disc. They find a linear polarization degree between 2% and 8%, depending on accretion rate, for a viewing angle of 90° (i.e. observing the system edge-on). In their code Schnittman and Krolik consider accretion onto galactic BHs with three different corona geometries: wedge 'sandwich', clumpy and spherical. Their code includes ray-tracing and it is fully relativistic (i.e. special and general). However they use Thomson cross-section for scattering which limits the accuracy of the results to photons with energy $\lesssim 100\,keV$. In Figure (3.4) the results for sandwich and spherical geometry are shown. The polarization degree increases for large viewing angles and non-spherically-symmetric geometry, as expected. The maximum polarization, for a viewing angle of 75° in the

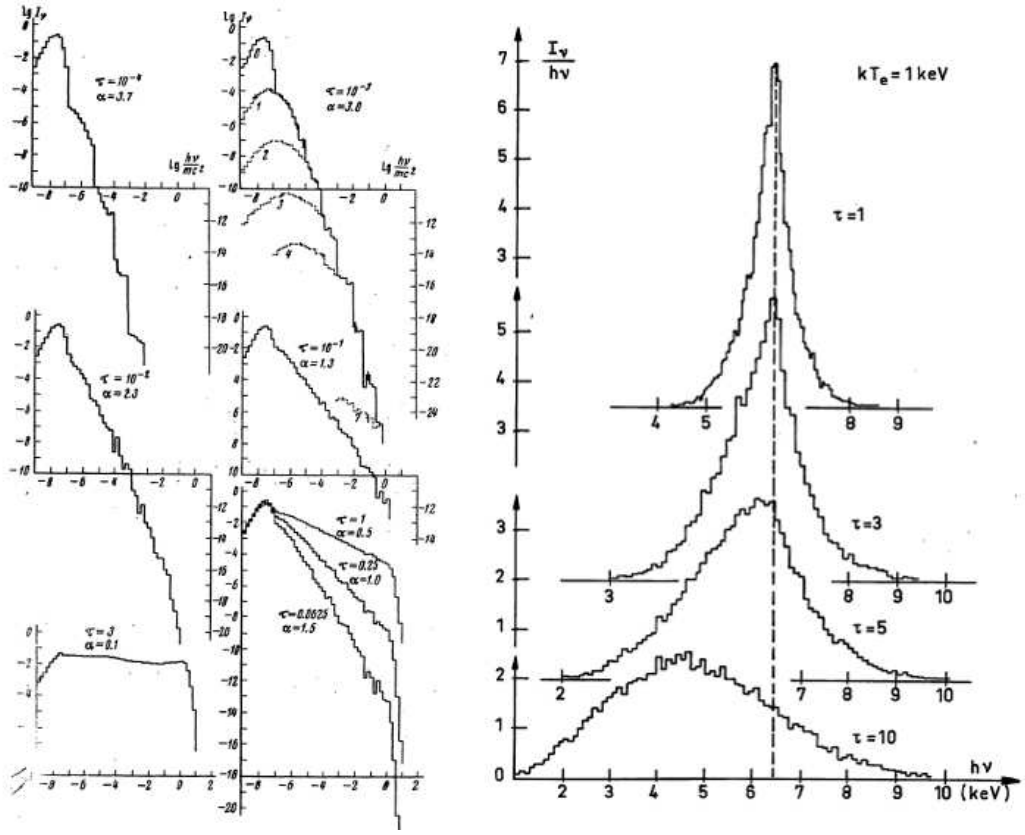

Figure 3.3: *left panel: emission spectra produced by Comptonization of Planckian soft photons - $kT_r = 10^{-8}\,mc^2$ - by weakly relativistic Maxwellian electrons - $kT_e = 0.5\,mc^2$ - for different optical depth, τ (from Pozdnyakov et al. 1977 [58]. right panel: emission spectra produced by Comptonization of $6.4\,keV$ Iron line by a cloud of thermal electron with $kT_e = 1\,keV$ for different optical depth (from Pozdnyakov et al. 1978 [59].)*

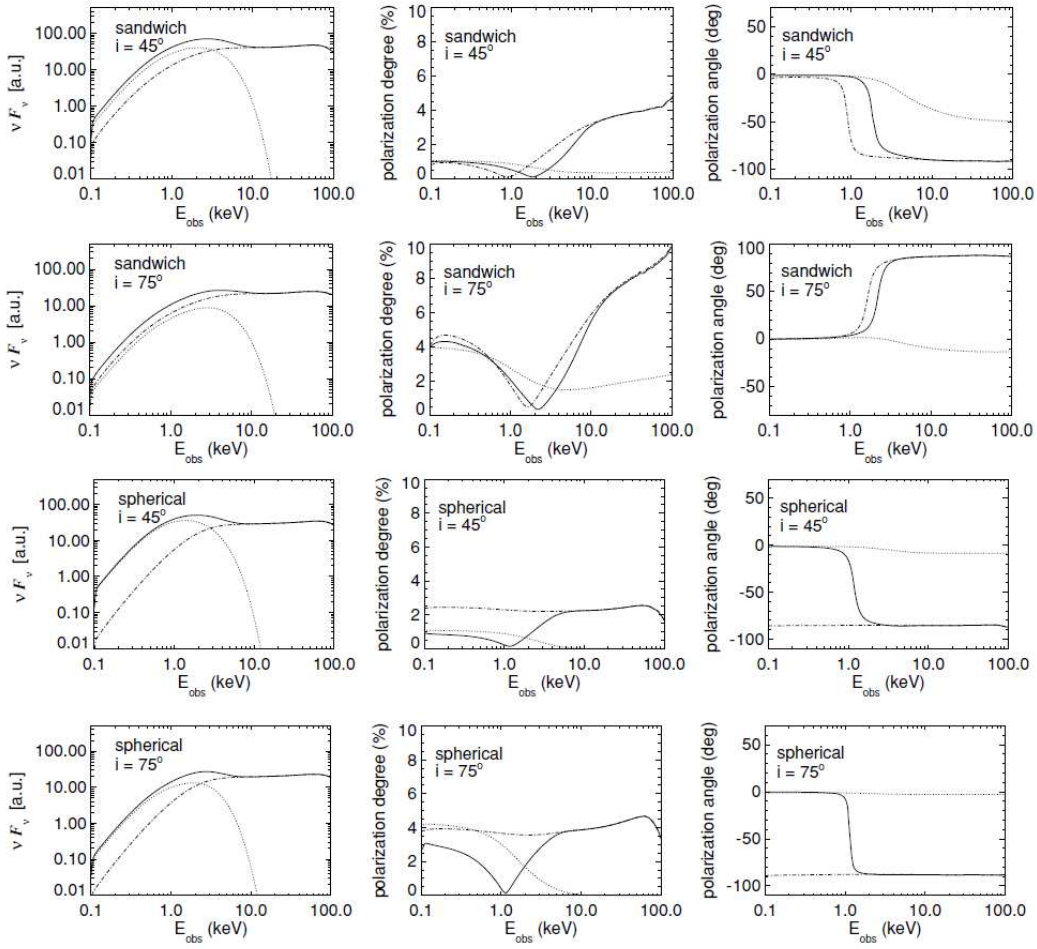

Figure 3.4: *The three columns show Flux, polarization degree and polarization angle as a function of energy for an inclination angle of* 45° *and* 75° *for a sandwich corona (top panels) and a spherical corona (bottom panels). Dotted lines represent contributions directly from the thermal disk, dot-dashed curves are corona-scattered photons and the solid lines represent the total (from Schnittman and Krolik, 2010 [66]).*

sandwich corona reaches the value of 10%.

Chapter 4

The Model

In this chapter we are going to describe the physical model we used in the simulations while the computational algorithms are illustrated in the next chapter. We firstly applied our code on two cases of astrophysical interest: the continuum emission in AGN and the Comptonization of the Iron-line in Binaries. The model includes all special relativistic corrections but general relativity is not considered, implying that light is not bended even when close to the BH. This approximation results in an underestimate of the number of scatterings and lost photons (i.e. fallen into the BH), especially in the case of SPHERICAL corona.

We considered two geometries for the corona, a SLAB corona which completely covers the disc and a SPHERICAL corona surrounding the inner part of the disc. In Figure (4.1) a cartoon representing these two geometries is shown.

In the case of continuum in AGN, the emission is given by the multi-temperature blackbody photons arising from a Shakura-Sunyaev disc (i.e. optically thick and geometrically thin). In the case of the line, the emission is constituted by Iron K_α photons with energy fixed at $6.4\,keV$. The outer radius of the disc affects only the low energy tail of blackbody emission but in terms of photons reabsorption it has to be considered infinite for both cases. Furthermore, we considered only Schwarzschild BHs with event horizon equals to $6\,r_g = 3\,R_S$ for both the models, as shown in the cartoon. Finally, due to symmetry, the spectra and the polarization signals are the same if considering only one hemisphere of the system (with respect to the disc), as we did.

The free parameters for the AGN model are

- BH mass: we set this value to $10^8\,M_\odot$
- τ, the optical depth of the corona: we considered the optically thin

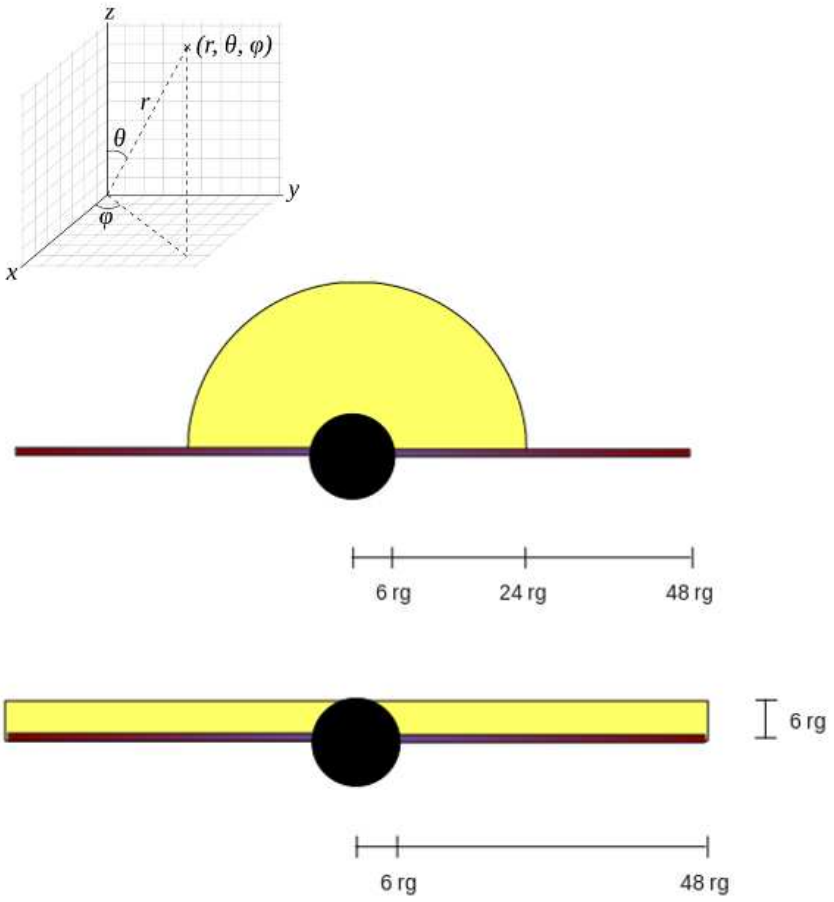

Figure 4.1: *Corona geometries used in the simulations. Lengths are expressed in gravitational radii and are all on scale, apart from the disc which in the code has no thickness. Due to symmetry, spectra and polarization signals are the same if considering only one hemisphere of the system and so we did. Spherical and Cartesian coordinate systems are shown in the upper-left corner.*

case $\tau = 0.1$ and the optically thick case $\tau = 1$. For the SPHERICAL corona the optical depth is defined radially while for the SLAB corona is defined vertically

- kT_e, the thermal energy of the corona fixed at the value of $kT_e = 100\,keV$

the free parameters for the XRB model are

- τ, the optical depth of the corona: we considered two cases for both types of emission, $\tau = 0.1$ and $\tau = 1$
- kT_e, the thermal energy of the corona fixed at the value of $kT_e = 2\,keV$

The mass is not considered in the case of line emission because affects only the blackbody emission from the disc.

The accretion rate, is set to the value $\dot{m}_{Edd} = 7.2 \times 10^{-8}\,M_\odot\,s^{-1}$ which correspond to having a source which radiates at Eddington luminosity. For AGN typical luminosities are of the order of fraction of L_{Edd}, but in our code the accretion rate affects only the temperature of the disc, through equation (2.10), and we did this choice to avoid having too much infrared seed photons.

Before starting, it is useful to introduce some notation rules: all the quantities with the subscript 'd' refers to the reference frame of the disc which is assumed to be non-rotating; the subscript 'e' indicates quantities in the reference frame of the electron; the lower-case, θ and ϕ refer to position angles in spherical coordinates while the upper-case Θ and Φ refer to direction angles in spherical coordinates. Finally, the prime apex $'$ represents quantities after the scattering, non-primed quantities before the scattering. We used standard definition of spherical coordinates (see the upper-left corner of Fig. (4.1) with R the radial coordinate, θ the polar angle and ϕ the azimuthal angle which can be obtained from a right-handed Cartesian coordinate system by the following transformations

$$\begin{cases} R &= \sqrt{x^2 + y^2 + z^2} \\ \theta &= \arctan\left(\dfrac{y}{x}\right) \\ \phi &= \arccos\left(\dfrac{z}{R}\right) \end{cases}$$

The approach is to follow every photon trough its journey from the disc to the observer or into the BH or onto the disc. For the moment reflection from the disc is not included, so when a photon hit the disc or escape from the corona with an angle $\Theta_d > \pi/2$ is lost, as well as if it fall into the BH.

4.1 Generating the seed photons

As said before, we considered two types of emission from the disc. From now on, we will refer to optical/UV photons arising from the Shakura-Sunyaev disc as 'BB seed photons', and to monochromatic $6.4\,keV$ Iron-line photons as 'K_α seed photons'. For K_α seed photons the angular distribution of the emission is isotropic, both polar and azimuthal. In the case of blackbody emission we considered limb darkening effect (see Eq. 2.14).

In order to properly extract the radius, in the case of multi-temperature blackbody emission, we considered two opposite effects:

- inner annuli $(R + dR)$ emit most because they are hotter and the flux is proportional to the fourth power of the temperature, in accord with the Stefan-Boltzmann law:

$$F(R) = \sigma_{SB} \cdot T(R)^4 \tag{4.1}$$

- on the other hand, outer annuli also emit most because the emission is proportional to the area and to big radii correspond big areas (for the same dR)

where $T(R)$ is given by equation (2.10).

In the case of the Iron-line emission, we assumed a simple emissivity law (**citazione!!!**) such as

$$F(R) \propto R^{-2.5} \tag{4.2}$$

Once the emission point and direction are calculated, the energy of the BB seed photon is extracted from the Planckian, corresponding to the temperature associated with that radius (see Eq. 2.10 and 2.13). At this point is possible to build the wave 4-vector of the seed photon

$$\begin{aligned} K_{d,t} &= \frac{2\,\pi\,\nu_d}{c} \\ K_{d,x} &= K_{d\{0\}}\, sin(\Theta_d)\, cos(\Phi_d) \\ K_{d,y} &= K_{d\{0\}}\, sin(\Theta_d)\, sin(\Phi_d) \\ K_{d,z} &= K_{d\{0\}}\, cos(\Theta_d) \end{aligned} \tag{4.3}$$

where ν_d is the frequency of the photon in the reference frame of the disc. The possible initial polarization is calculated as well, in accord to the values tabulated in Table XXVI in Chandrasekhar [7]. In order to build the polarization vector, $\vec{P_d}$, we follow the approach in Matt et al. 1996 [45] by making

use of auxiliary unit vectors:

$$\begin{aligned}
\vec{Q_+} &= \frac{1}{\sqrt{1-D_z^2}}\left(-D_y\,,D_x\,,0\right)\\
\vec{Q_-} &= \frac{1}{\sqrt{1-D_z^2}}\left(-D_x\,D_z\,,-D_y\,D_z\,,1-D_z^2\right)\\
\vec{U_+} &= \frac{1}{\sqrt{2\,(1-D_z^2)}}\left(-D_y\,-D_x\,D_z\,,D_x\,-D_y\,D_z\,,1\,-D_z^2\right)\\
\vec{U_-} &= \frac{1}{\sqrt{2\,(1-D_z^2)}}\left(D_y\,-D_x\,D_z\,,-D_x\,-D_y\,D_z\,,1\,-D_z^2\right)
\end{aligned} \tag{4.4}$$

where $\vec{D}$ is the spatial part of the wave 4-vector, $\vec{K_d}$, normalized to 1.[1]

These vectors define two reference frames in the plane normal to the photon direction. The axes x' and y' of the first frame are defined by $\vec{Q_+}$ and $\vec{Q_-}$ respectively. y' is the projection of the z-axis, while x' is the intersection with the $x-y$ plane and it is obtained by a 90° clockwise rotation of the y' axis. The second frame is obtained by a 45° counterclockwise rotation of the first one.

It can be shown that the contributions of the jth photon to the second, Q, and third, U, Stokes parameters are given by:

$$\begin{aligned}
\vec{Q_j} &= \left(\vec{Q_+}\cdot\vec{P_j}\right)^2 - \left(\vec{Q_-}\cdot\vec{P_j}\right)^2\\
\vec{U_j} &= \left(\vec{U_+}\cdot\vec{P_j}\right)^2 - \left(\vec{U_-}\cdot\vec{P_j}\right)
\end{aligned} \tag{4.5}$$

Therefore, once the auxiliary vectors are built, the polarization vector, $\vec{P_d}$, is needed to calculate the Stokes parameters of the jth photon. If the value of an extracted random number between 0 and 1 is less than the initial polarization degree taken from Table XXVI of Chandrasekhar [7], the photon is linearly polarized and the polarization vector can be constructed by satisfying the following conditions:

- $P_z = 0$ (the linear polarization due to the optically thick atmosphere is on a plane parallel to the disc)
- $D_x\,P_x + D_y\,P_y = 0$ (the polarization vector is always orthogonal to the propagation of the photon)
- $P_x^2 + P_y^2 = 1$ (the polarization vector is a unit vector)

[1] $D_x = \frac{K_{d,x}}{|\vec{K_d}|}$, $D_y = \frac{K_{d,y}}{|\vec{K_d}|}$, $D_z = \frac{K_{d,z}}{|\vec{K_d}|}$

Otherwise the seed photon is randomly polarized and can be obtained as a random linear combination of the auxiliary vectors $\vec{Q_+}$ and $\vec{Q_-}$:

$$\begin{aligned} P_x &= sin(\alpha_r)\, Q_{-,x} + cos(\alpha_r)\, Q_{+,x} \\ P_y &= sin(\alpha_r)\, Q_{-,y} + cos(\alpha_r)\, Q_{+,y} \\ P_z &= sin(\alpha_r)\, Q_{-,z} + cos(\alpha_r)\, Q_{+,z} \end{aligned} \tag{4.6}$$

where α_r is a random angle between 0 and 2π.

It is important to notice that the polarization vector is not a real 4-vector. The spatial components represent where the electric field of the electromagnetic wave is pointing, the temporal component can always be set to zero. Finally, the Stokes parameters for the jth photon are calculated in accord to Eq. (4.5).

K_α seed photons have energy fixed and no initial polarization (i.e. randomly polarized).

4.2 The scattering

The corona is believed to made up of relativistic but thermal electrons. When the the thermal energy of the electrons is of order of their rest energy ($mc^2 = 511\, KeV$), relativistic corrections are needed to properly extract their speed. Since we are considering thermal energies of the order $kT_e = 100\, keV$, we used the relativistic Maxwell distribution given by Poutanen and Vilhu 1993 [56]

$$f(\gamma) = \frac{y}{4\,\pi K_2(y)}\, e^{-y\,\gamma},\ y = \frac{m_e\, c^2}{k\, T_e} \tag{4.7}$$

where γ is the Lorentz factor of the electron while $K_2(y)$ is the modified Bessel function of the second kind and it is a function of y, the ratio between the rest energy of the electrons and their thermal energy. From γ, the modulus of the velocity is derived $\beta = \sqrt{1 - (1/\gamma^2)}$ and a random direction for the vector $\vec{\beta}$ is chosen, assuming that electrons do not have any preferential motion in the corona with respect to the seed photon.

At this point, a scattering event might happen but, in order to calculate the cross-section and the energy exchange, we need to switch to the reference

frame of the moving electron. The Lorentz matrix for the boost is:

$$\Lambda = \begin{pmatrix} \gamma & -\beta_x\,\gamma & -\beta_y\,\gamma & -\beta_z\,\gamma \\ -\beta_x\,\gamma & 1+(\gamma-1)\dfrac{\beta_x^2}{\beta^2} & (\gamma-1)\dfrac{\beta_x\,\beta_y}{\beta^2} & (\gamma-1)\dfrac{\beta_x\,\beta_z}{\beta^2} \\ -\beta_y\,\gamma & (\gamma-1)\dfrac{\beta_x\,\beta_y}{\beta^2} & 1+(\gamma-1)\dfrac{\beta_y^2}{\beta^2} & (\gamma-1)\dfrac{\beta_y\,\beta_z}{\beta^2} \\ -\beta_z\,\gamma & (\gamma-1)\dfrac{\beta_x\,\beta_z}{\beta^2} & (\gamma-1)\dfrac{\beta_y\,\beta_z}{\beta^2} & 1+(\gamma-1)\dfrac{\beta_z^2}{\beta^2} \end{pmatrix} \tag{4.8}$$

The wave 4-vector in the reference frame of the electron, K_e, is obtained by a simple boost of the wave 4-vector in the reference frame of the disc, K_d:

$$K_e = \Lambda\,K_d \tag{4.9}$$

During the boost, the energy of the photon, contained in the temporal component of the wave vector ($K_{d,t} = \dfrac{2\,\pi\,\nu_d}{c}$), is statistically increased by a factor γ. The polarization vector needs more attention to be boosted: the degree of polarization is indeed a Lorentz invariant and the unit 4-vector P_d is only defined to within a multiple of K_d (see Connors et al. 1980 [11]). Let P_{temp} be the Lorentz-transformed polarization vector P_d

$$P_{temp} = \Lambda\,P_d \tag{4.10}$$

The polarization 4-vector in the reference frame of the electron, P_e, can be rewritten in the form:

$$P_e = \left(0, P_{temp,i} - \frac{P_{temp,0}\,K_{e,i}}{K_{e,0}}\right), \quad i = x, y, z \tag{4.11}$$

Once the frequency of the photon in the reference frame of the electron is calculated, it is possible to derive the Klein-Nishina cross section for the scattering (Eq. 3.4).

At this point, switching back to the reference frame of the disc, the mean free path (MFP) of the photon is calculated. The mean free path is defined as the average distance a photon can travel through an absorbing or scattering material without being absorbed or scattered. Assuming that the electrons are spatially Poisson (i.e. randomly) distributed, the probability that a scattering happens is:

$$P = 1 - e^{-\tau} \tag{4.12}$$

where τ is the optical depth of the medium and it is defined as:

$$d\tau = n_e \, \sigma_{sc} \, dx \tag{4.13}$$

where n_e is the density of the electrons in the corona, σ_{sc} the scattering cross-section (Klein-Nishina, in this case) and dx the space traveled by the photon before the scattering. The product of the density and the cross-section of the scattering material is nothing else but the mean free path $l = \dfrac{1}{n_e \, \sigma_{sc}}$. Replacing τ and l in Eq. (4.12) and inverting we can derive the space, x, traveled by the photon before the scattering happens:

$$x = -\ln(1 - P) \, l \tag{4.14}$$

On the other hand, the mean free path can also be geometrically defined as the ratio between the extent of the scattering medium and its optical depth. In the case of the SLAB corona, the optical depth of the medium is meant vertically with respect to the plane of the disc while for the SPHERICAL corona is meant radially. We can therefore define l, respectively, as:

$$\begin{aligned} l &= \frac{H_{cor}}{\tau} \\ l &= \frac{R c_{out}}{\tau} \end{aligned} \tag{4.15}$$

Finally, the photon energy dependence on the mean free path is taken into account by weighting the traveled space with the ratio between the Thomson cross-section and the Klein-Nishina cross-section previously calculated, so that the MFP increases with energy because σ_{KN} decreases. In the end the traveled space, x, is calculated as:

$$x = -\ln(1 - \xi) \, l \, \frac{\sigma_T}{\sigma_{KN}} \tag{4.16}$$

where ξ is the usual random number between 0 and 1.

The coordinates of the photon are updated considering the traveled distance, x. If the arrival point falls within the BH radius the photon is lost, as well as if the arrival point is on the disc. If the arrival point falls outside the corona, the photon escapes toward the observer with no scattering and all the information related to that photon (energy, Stokes parameters and direction) are saved. Lastly, if the arrival point falls within the corona, the scattering happens at that point. In the case of SPHERICAL corona, we took into account also the possibility for photons generated in the outer part of the disc to hit the corona. In this case the mean free path is calculated

from the hit edge of the corona. If scattering happens, the energy exchange, is calculated in accord to Eq. (3.2) in the reference frame of the electron.

In order to calculate the scattering angle, Θ_{sc}, we followed the general Monte Carlo approach (see Eq. 5.2 in the next chapter for the details), used in Matt et al. 1996 [45]. Calling $\epsilon_0 = \frac{E_e}{mc^2}$ the ratio between the incident photon energy and the rest mass energy of the electron and $\mu = \cos\Theta_{sc}$ the cosine of the scattering angle, and noting that μ does not depend on the polarization status of the incident photon, we end up with the relation

$$P = \frac{\epsilon_0\left(\frac{3}{2} + \mu - \frac{1}{2}\mu^2\right) + \frac{1}{3}\left(1+\mu^3\right) - \frac{1}{\epsilon_0}\{\ln\left[1+\epsilon_0\left(1-\mu\right)\right] - \ln\left(1+2\epsilon_0\right)\}}{\frac{2}{3} + 2\epsilon_0 + \frac{1}{\epsilon_0}\ln\left(1+2\epsilon_0\right)} \tag{4.17}$$

where P is a number between 0 and 1 and represent the probability of having a scattering angle $\Theta_{sc} = \arccos\mu$. As said in Chapter 3, for polarized radiation the azimuthal distribution is no longer isotropic, but is related to the polarization vector of the incident photon (see Eq. 3.7). Using the same approach as for Θ_{sc} we obtain the relation

$$(2\pi P - \Phi_{sc})\left(\frac{E'_e}{E_e} + \frac{E_e}{E'_e} - \sin^2\Theta_{sc}\right) + \sin^2\Theta_{sc}\sin\Phi_{sc}\cos\Phi_{sc} = 0 \tag{4.18}$$

where E_e and E'_e are the energies of the incident and scattered photon in the reference frame of the electron, respectively.

The degree of polarization due to the scattering is given by (see Matt et al. 1996 [45])

$$\Pi = 2\frac{1 - \sin^2\Theta_{sc}\cos^2\Phi_{sc}}{\frac{E'_e}{E_e} + \frac{E_e}{E'_e} - 2\sin^2\Theta_{sc}\cos^2\Phi_{sc}} \tag{4.19}$$

With the same methodology followed before, by making use of the auxiliary vectors, the Stokes parameters of the scattered photon are calculated, as well as the polarization vector after the scattering in the reference frame of the electron, P'_e (Eq. 4.4-4.6).

Finally, the wave 4-vector (which contains the energy of the photon in its temporal component) and the polarization vector are anti-transformed to the reference frame of the disc by simply substituting $\vec{\beta}$ with $-\vec{\beta}$ in the boosting matrix (Eq. 4.8) and following the same procedure as for the boosting

(Eq. 4.9, 4.10 and 4.11). During the anti-boost the energy of the photon is statistically increased by another factor γ for an overall gain of γ^2 between the energy before, E_d, and after, E'_d, the scattering in the reference frame of the disc. The coordinates, direction, energy and polarization vector of the photon are updated and a new mean free path is calculated for a new possible scattering event. When a photon escapes, its energy, direction and Stokes parameters are saved and a new seed photon is generated.

Chapter 5

MoCA

In this chapter we are going to illustrate the algorithms used to perform the calculations described in the previous chapter. Before doing this, a brief description of Monte Carlo methods is required.

5.1 Monte Carlo methods

In probability theory, a 'Probability Density Function' (PDF), or density of a continuous random variable, is a function that describes the relative likelihood for this random variable to take on a given value. The probability for the random variable to fall within a particular region is given by the integral of this variable's density over the region. The 'Cumulative Distribution Function' (CDF), or simply 'distribution function', describes the probability that a real-valued random variable X with a given probability distribution will be found at a value less than or equal to x. If the PDF is a continuous function, the CDF is obtained by the integral:

$$P(X \leq x) \equiv F(x) = \int_{-\infty}^{x} f(t)\, dt \tag{5.1}$$

Monte Carlo methods are a class of computational algorithms that rely on repeated random sampling to compute their results. These methods are often used in computer simulations of physical and mathematical systems wherever it is unfeasible to compute an exact result with a deterministic algorithm. The term was coined in the 40s by John von Neumann, Stanislaw Ulam and Nicholas Metropolis, while they were working on nuclear weapon projects (Manhattan Project) in the Los Alamos National Laboratory[1]. The

[1]It was named after the Monte Carlo Casino, a famous casino where Ulam's uncle often gambled away his money.

easiest way to randomly extract a variable t distributed according to a PDF $f(t)$ is by making use of Eq. (5.1). Let t_{min} and t_{max} be the minimum and the maximum value of the interval in which we want to extract the variable t. The probability of randomly extract t within the given interval is

$$P(X = t) = \frac{\int_{t_{min}}^{t} f(t')\,dt'}{\int_{t_{min}}^{t_{max}} f(t')\,dt'} \tag{5.2}$$

where the denominator is a normalization factor which assure that the total probability is equal to 1. From now on we will refer to Eq. (5.2) as the fundamental MC relation. If $f(t')$ is integrable, Eq. (5.2) reduces to

$$P(X = t) = \xi = \frac{F(t) - F(t_{min})}{N} \tag{5.3}$$

where N is the normalization, the CDF $F(t)$ is the primitive of the PDF $f(t)$ and ξ is a number between 0 and 1. If $F(t)$ is invertible, we can derive t as

$$F(t) = N\,\xi + F(t_{min}) \rightarrow t = F^{-1}(N\,\xi + F(t_{min})) \tag{5.4}$$

It can be demonstrated that randomly extracting ξ between 0 and 1 (from now on ξ will always represent a random extracted number between 0 and 1), a random value t, belonging to the PDF $f(t)$, is obtained. From now on we refer to this procedure as 'inversion method' and represents the easiest case. Two kinds of complications may arise: $f(t)$ is not integrable or $f(t)$ is integrable but $F(t)$ is not invertible.

Rejection method and numerical solution

Many PDFs in physics fall into the first category. For example the CDF of the Normal (Gaussian) distribution[2] is the 'Error function', a non-elementary special function defined only in integral form or by a Taylor expansion of the integrand. In this case, a popular, even if time consuming, procedure to extract the random variable is the so-called 'rejection method'. The idea is to confine the unintegrable distribution with a simpler one (the simplest is a flat distribution) and then starting to randomly extract a value for the variable and follow an 'hit & miss' sampling. Let us assume that we want to randomly extract a value for the variable x whose PDF is $D(x)$. First of all we have to choose a reasonable range of values for the sampling, x_{min} and x_{max}, and we have to calculate the peak of the distribution D_{max} which is usually feasible. Then, a random value between x_{min} and x_{max} is extracted,

[2]sometimes we refer to PDFs as 'distributions', as is customary, even if misleading.

$x_{ran} = x_{min} + \xi_1 (x_{max} - x_{min})$ and the corresponding probability for that value is calculated, $D(x_{ran})$. A second random number is extracted, ξ_2, and the 'random probability' is calculated as $D_{ran} = \xi_2 D_{max}$. Now, if $D_{ran} < D(x_{ran})$ then x_{ran} is accepted, otherwise it is rejected and the procedure restarts with the extraction of another x_{ran}. It is possible to demonstrate that the accepted values for the variable x are randomly distributed in accord to $D(x)$. The method can be optimize by using a sampling distribution 'closer' to the unintegrable one, instead of the flat distribution, in order to reduce the number of rejections; this is fundamental if this 'hit & miss' procedure is used for evaluating the area (the CDF) below the distribution which is not our case since we just need one good extraction. In Figure (5.1) a cartoon illustrates the described procedure.

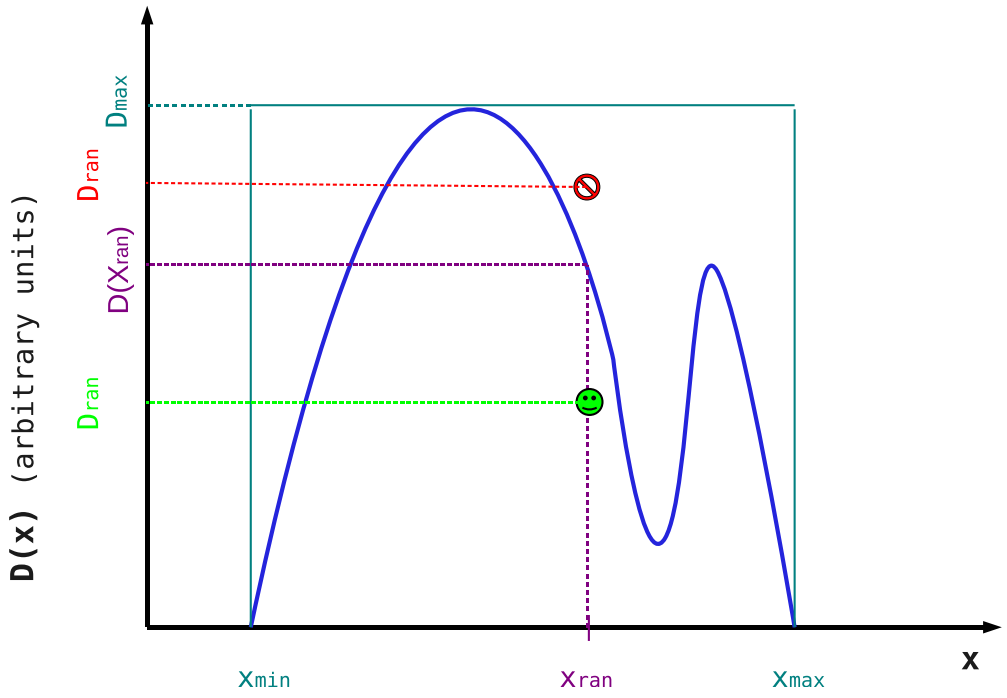

Figure 5.1: *A cartoon representing the rejection procedure: the blue line represent the unintegrable distribution, while the green box is the flat distribution used to sample the blue one. A randomly extracted value x_{ran} is accepted if a second randomly extracted number (D_{ran}) between zero and D_{max} is less than $D(x_{ran})$, otherwise it is rejected.*

If the PDF, $f(t)$, has an analytic primitive, $F(t)$, which is not invertible, we can solve the equation

$$\xi = \frac{F(t) - F(t_{min})}{N} \tag{5.5}$$

numerically. One easy way to do it, is by building up a grid of values of the random number ξ as a function of t and then determine $t(\xi)$ by inversion. The drawback of this approach is the resolution of the variable t which is finite and as large as the grid built for ξ.

Many other algorithms falling within the class of Monte Carlo methods have been developed in the last decades. The main purpose of this algorithms is to optimize the time consumption, especially when these methods are used to perform integrals or repeated samplings. A description of these methods is beyond the aims of this chapter and we refer the interested reader to the overabundant existing literature.

5.2 The code

MoCA is written in IDL (Interactive Data Language), a programming language used for data analysis. IDL is vectorized, numerical, and interactive and it is very popular in astronomy and medical imaging and commonly used for interactive processing of large amounts of data (including image processing). Our code is modular and with minor modifications can be applied to different accreting systems and astrophysical situations. In Fig. **??** a diagram illustrating how the code works is shown. The main procedure (main.pro) consists of a main loop over the number of photons generated and another sub-loop for scatterings. During the travel of the photon from the disc to the observer, the main program calls several subroutines which performs specific tasks. For random numbers, the main ingredient of Monte Carlo simulations, we used a robust random number generator developed by David Fanning [18].

At the beginning, after the free parameters are set, and some quantities are initialized, the main loop starts. The polar angle coordinate of the seed photon is set to the value $\theta_d = \frac{\pi}{2}$ because the photon comes from the disc which lays on the equatorial plane (see the upper-left corner of Fig. 4.1); the azimuthal angle, ϕ_d is randomly extracted in the interval $[0, 2\pi]$. The radius is extracted accordingly to the emissivity of the disc and it is calculated by the emissivity.pro subroutine.

emissivity.pro

As said in the previous chapter, in the case of blackbody emission from the disc, we have to consider that inner annuli are hotter but smaller. This means that we have to weight Stefan-Bolzmann law for area elements ($R\,dR$). In order to do that, the fundamental MC approach (Eq 5.2) has been used

$$\xi = \frac{\int_{R_{min}}^{R} F(R)\,R\,dR}{\int_{R_{min}}^{R_{max}} F(R)\,R\,dR} \tag{5.6}$$

where R_{min} and R_{max} are, respectively, the inner and outer radius of the disc and $F(R)$ is obtained from equations 4.1 and 2.10

$$F(R) = \sigma_{SB}\left[\frac{3GM\dot{m}}{8\pi R^3\sigma}\left(1-\sqrt{\frac{R_{min}}{R}}\right)\right] \tag{5.7}$$

ξ is the usual random number between 0 and 1.

Integration of equation 5.6 leads to

$$\xi = \frac{R_{max}\left[R_{min}\left(-1+\frac{2}{3}\sqrt{\frac{R_{min}}{R}}\right)+\frac{R}{3}\right]}{R\left[R_{min}\left(-1+\frac{2}{3}\sqrt{\frac{R_{min}}{R_{max}}}\right)+\frac{R_{max}}{3}\right]} \tag{5.8}$$

This equation cannot be analytically inverted and a numerical approach is needed to obtain R as a function of ξ. In this case we used a grid of values for the random number ξ as a function of R and then we determined $R(\xi)$ by inversion.
In Fig. 5.2 the radial distribution of BB seed photons is shown.

In the case of the 6.4 KeV Iron line emission, the emissivity law (4.2), weighted for the area, integrated and inverted, leads to the solution

$$R = \left[\xi\left(\frac{1}{\sqrt{R_{max}}}-\frac{1}{\sqrt{R_{min}}}\right)+\frac{1}{\sqrt{R_{min}}}\right]^{-2} \tag{5.9}$$

In Fig. 5.3 the radial distribution of K_α seed photons is shown.

Once the coordinates, R_d, θ_d and ϕ_d, are calculated, the energy and the direction of the seed photon are extracted. The subroutine shaksun.pro is called to accomplish the first task.

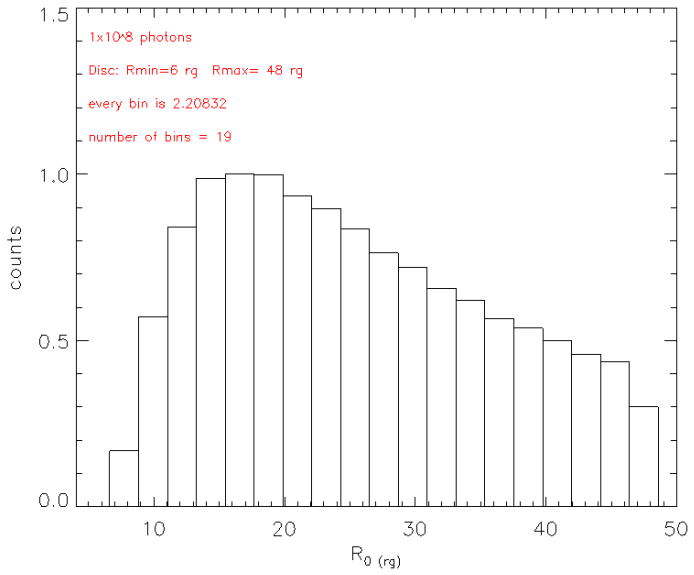

Figure 5.2: *Radial distribution for* 10^8 *BB seed photons. The units are in gravitational radii.*

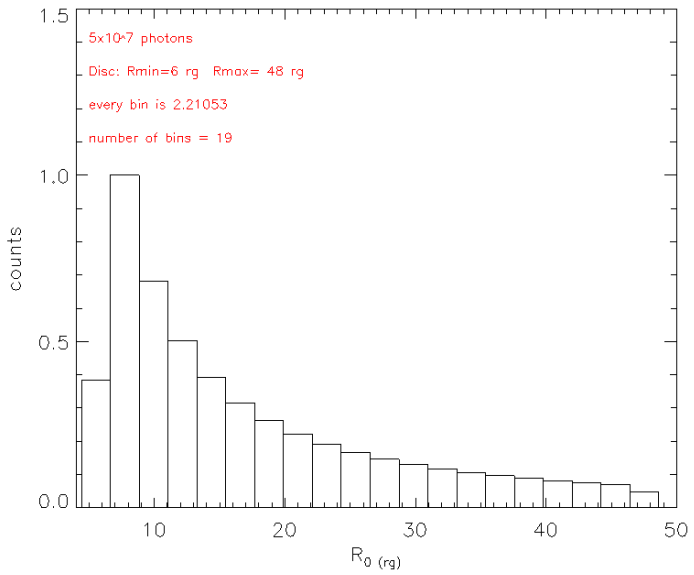

Figure 5.3: *Radial distribution for* 5×10^7 K_α *seed photons. The units are in gravitational radii.*

shaksun.pro

In order to extract the energy of the BB seed photon we should integrate Eq. 2.13 over energies and than invert the result, as we did for the emissivity of the disc. In this case the problem is not the inversion but the integration of the Planck's law, which leads to an uncomfortable poly-logarithmic solution (the 'Error function'). In this case, therefore, we used the rejection method. In the rejection procedure we allowed the energy of the seed photon ($E_d = h\,\nu_d$) to be extracted within a symmetric interval of plus/minus 2 orders of magnitude with respect to $k_B\,T(R_d)$ for the extracted radius R_d.

In Fig. 5.4 a plot of the spectrum produced by the T_{max} annulus of a $10^8 M_\odot$ black hole is shown. The black histogram is obtained binning the extracted frequencies by rejection method, using 10^4 tries. The red line represent the analytical solution for that temperature.

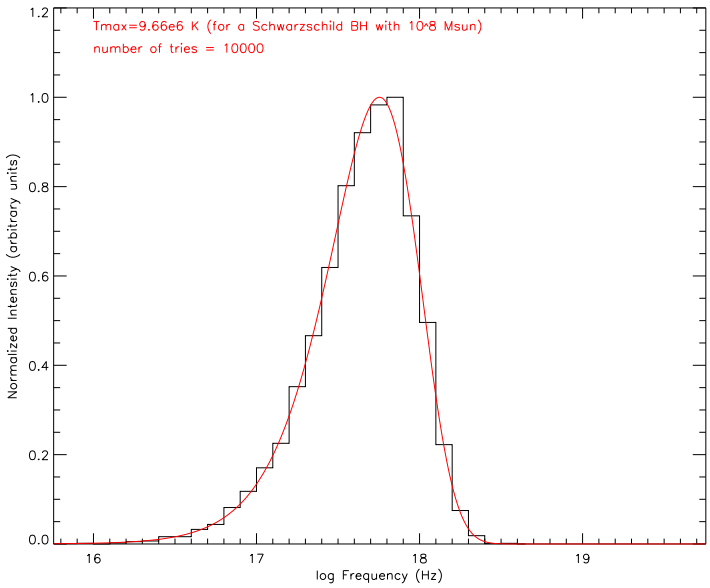

Figure 5.4: *Plot of the Planck distribution. The black histogram is obtained by binning the frequencies extracted with rejection method, using* 10^4 *tries. The red line represent the analytical solution. The distribution peaks in the soft X-rays, as expected for the hotter part of the disc for a* $10^8 M_\odot$ *BH.*

In the case of K_α seed photons the energy is fixed at the value of $6.4\,keV$.

Once the energy of the seed photon is obtained, the direction of propagation is calculated by the routine chandra.pro.

chandra.pro

BB seed photons produced by the optically thick atmosphere of the disc suffer limb darkening effect. In order to extract a polar direction angle Θ_d, we followed the general MC approach

$$\xi = \frac{\int_0^{\mu} F(\mu)\, d\mu}{\int_0^{1} F(\mu)\, d\mu} \tag{5.10}$$

where $F(\mu)$ is given by Eq. 2.14. Integration leads to the cubic equation:

$$\xi = \frac{\mu^2 \left(\frac{1}{2} + \frac{2.06}{3}\mu\right)}{1.18667} \tag{5.11}$$

By the extraction of a random number, ξ, and solving Eq. 5.11, it is possible to obtain a value for μ distributed accordingly to Eq. 2.14 In Fig. 5.5 the polar emission distribution is shown in terms of $\mu = \cos(\Theta_d)$. The routine

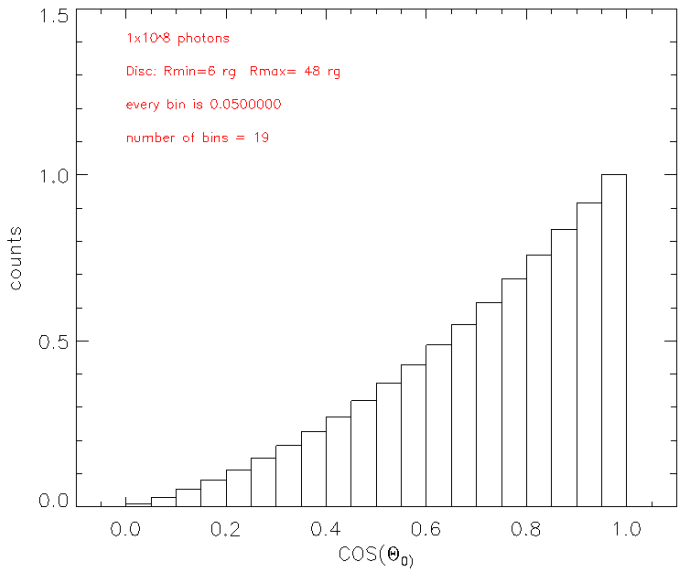

Figure 5.5: *Polar angular distribution for* 5×10^7 *photons arising from a Shakura-Sunyaev disc. The plot is in the cosine of the emission angle,* $\mu = \cos(\Theta_d)$

also associates a probability, $P_{pol,0}$, for the BB seed photon to be linearly polarized, in accord to Table XXVI in Chandrasekhar et al. 1960 [7]. $P_{pol,0}$ ranges from 0% for $\Theta_d = 0$ to 11.7% for $\Theta_d = \pi/2$ (see Fig. 2.3).

In the case of K_α seed photons, Θ_d is randomly extracted in the interval $[0, \pi]$, since the neutral atmosphere of the disc is not optically thick for X-ray

photons as it is for optical BB photons and $P_{pol,0} = 0$. For both the kinds of emission Φ_d is randomly extracted between 0 and $2\,\pi$. With both the direction angles, the wave 4-vector of the seed photon in the reference frame of the disc, $\vec{K_d}$, is built.

In order to calculate the polarization vector, $\vec{P_d}$, the subroutine stokes.pro is invoked by the main procedure.

stokes.pro

The inputs of this routine are the direction of the photon, $\vec{K_d}$, and its probability of being initially polarized, $P_{pol,0}$. Auxiliary vectors (Eq. 4.4) are built and a random number, ξ, is extracted. If $\xi \leq P_{pol,0}$, the polarization vector, $\vec{P_d}$, is calculated in accord to the condition of being parallel to the plane of the disc (see the conditions below Eq. 4.5 in the previous chapter), otherwise it is randomly chosen (see Eq. 4.6). The outputs of the routine are the polarization vector, $\vec{P_d}$, and the Stokes parameters, derived in agreement with Eq. 4.5.

In the case of SPHERICAL corona, the subroutine ControllerDisc.pro checks if photons generated in the outer part of the disc (i.e., those whom radial coordinate is larger than the outer radius of the corona $R_0 > Rc_{out} = 24\,r_g$), can hit the corona. If so, the photon is traslated to the edge of the corona hit. In the case of SLAB corona, this subroutine is not called by the main procedure. At this pont the scattering loop starts.

maxrel.pro

In the maxrel.pro subroutine, the Lorentz factor, γ, of the possible scatterer electron is extracted from the relativistic Maxwell distribution, Eq. 4.7. This function is integrable, so we used again the fundamental MC relation

$$\xi = \frac{\int_1^\gamma f(\gamma')\,d\gamma'}{\int_1^\infty f(\gamma')\,d\gamma'} \tag{5.12}$$

whose integral can be inverted to obtain the simple formula

$$\gamma = -\frac{\ln(1-\xi)}{y} + 1 \tag{5.13}$$

In Figure 5.6 two examples of the relativistic Maxwell distribution are shown.

From the Lorentz factor, the modulus of the speed, β, is derived and random components for the vector are chosen.

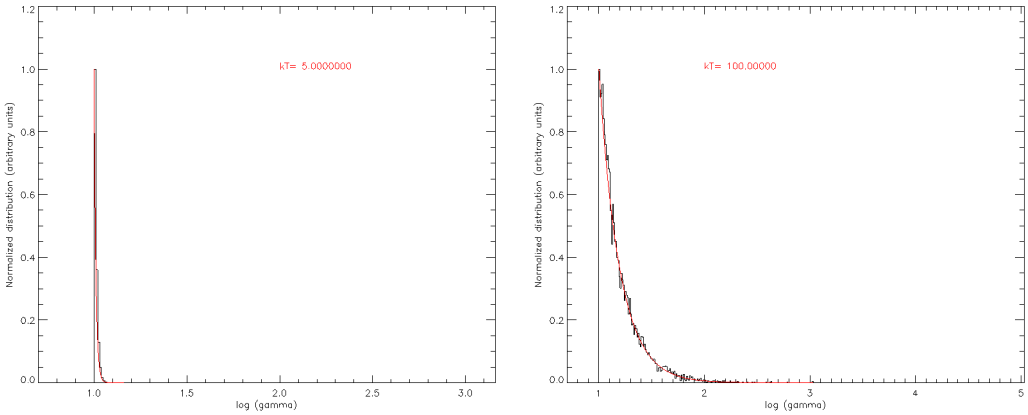

Figure 5.6: *The black histogram is obtained using Eq. 5.13 with* 10^4 *tries. The red line represent the analytical distribution (Eq. 4.7). On the left panel the gamma distribution for electrons with thermal energy* $kT = 5\,keV$ *is shown. On the right the one for* $kT = 100\,keV$*.*

lorentz.pro

In this subroutine the Lorentz matrix for the boost is built. The wave 4-vector, K_d, and the polarization vector, $\vec{P}_d$ are transformed in accord to equations 4.9-4.11. For both the reference frames (i.e. before and after the boost) the routine also checks, if the condition of unitarity for the polarization vectors, the light-like nature of the wave 4-vector and the orthogonality between the two are satisfied:

$$\begin{aligned} |P_\mu| \equiv 1 &= \sqrt{P_t^2 + P_x^2 + P_y^2 + P_z^2} \\ K_\mu\, K^\mu \equiv 0 &= K_t^2 - K_x^2 + K_y^2 + K_z^2 \\ \mathbf{K}\cdot\mathbf{P} \equiv 0 &= K_t\, P_t + K_x\, P_x + K_y\, P_y + K_z\, P_z \end{aligned} \tag{5.14}$$

The temporal component of the boosted wave 4-vector contains the energy of the photon in the reference frame of the electron, which allows to the crosssec.pro routine to calculate the cross-section for the scattering.

crosssec.pro

This routine simply uses the energy of the photon in the reference frame of the electron to calculate the Klein-Nishina cross-section in agreement with Eq. 3.4. If the ratio between the energy of the photon and the rest energy of the electron is less than 10^{-2}, the non-relativistic approximation, truncated at the second order in x is used (Eq. 3.5).

mfp.pro

As anticipated in the previous chapter, the space traveled by the photon inside the corona is given by Eq. 4.16 and it is a function of the energy of the photon, through the cross-section σ_{KN}, and the optical depth of the corona which is contained in the mean free path l. Once this space is calculated, the spherical coordinates of the photon, in the reference frame of the disc, are updated to the arrival point and the subroutine controller checks the fate of the photon.

controller.pro

The inputs of this routine are the radius of the BH, R_{BH}, the coordinates of the arrival point, R_f, θ_f, ϕ_f, the direction of the photon, Θ_d, Φ_d in the reference frame of the disc, and the parameters which define the geometry of the corona, Rc_{in} and Rc_{out} for the SPHERICAL corona and H_{SL} and L_{SL} for the SLAB corona.

If $R_f \leq R_{BH}$, the photon has fallen into the BH and it is lost. The routine creates an exit from the scattering loop and a new seed photon is generated. If $\theta_f > \pi/2$, the photon has fallen onto the disc and it is lost as well. In the case of SPHERICAL corona, if $R_f > Rc_{out}$, the photon has escaped. For SLAB geometry, the escape condition is verified if $R_f \cos(\theta_f) > H_{SL}$ or $R_f \sin(\theta_f) > L_{SL}$. Photons which escapes below the horizon of the disc, i.e. when $\Theta_d > \pi/2$ will fall onto the disc, if it is assumed to be infinite and they are lost as well. Only photons which escape above the horizon are safe and exit from the scattering loop. If none of these condition is verified, a scattering happens at the arrival point, inside the corona.

invcomp.pro

Photons survived to the travel suffers a Compton scattering. The energy, in the reference frame of the electron, is decreased according to equation 3.2. In order to do that, the scattering angle, Θ_{sc} must be calculated. As said in the previous chapter, applying the fundamental MC relation as in Matt et al 1996 [45] leads to the relation 4.17. This equation is not invertible and in order to extract the cosine of the scattering angle, μ, as a function of a random number between 0 and 1 (which is P in Eq. 4.17), a numerical approach is needed. A vector of values for P is created by letting Θ_{sc} range from 0 to π in 10^3 steps. Then a random number is extracted and it is associated to the closest value in the P array and the corresponding angle in Θ_{sc} array is obtained.

The same problem occurs for the distribution in the azimuthal angle, Φ_{sc}, (Eq. 4.18) and the same method has been applied.

sdirection.pro

The direction of the photon after the scattering is calculated in this subroutine as a function of the scattering angles, Θ_{sc} and Φ_{sc}, the direction before the scattering, expressed by the spatial components of the wave 4-vector K_e, and the polarization vector before the scattering, P_e, everything in the reference frame of the electron. In components, from Matt et al 1996

$$\begin{aligned} D'_{x,e} &= D_{x,e}\cos\Theta_{sc} + P_{x,e}\sin\Theta_{sc}\cos\Phi_{sc} + \sin\Theta_{sc}\sin\Phi_{sc}\,(D_{y,e}\,P_{z,e} - D_{z,e}P_{y,e}) \\ D'_{y,e} &= D_{y,e}\cos\Theta_{sc} + P_{y,e}\sin\Theta_{sc}\cos\Phi_{sc} + \sin\Theta_{sc}\sin\Phi_{sc}\,(D_{z,e}\,P_{x,e} - D_{x,e}P_{z,e}) \\ D'_{z,e} &= D_{z,e}\cos\Theta_{sc} + P_{z,e}\sin\Theta_{sc}\cos\Phi_{sc} + \sin\Theta_{sc}\sin\Phi_{sc}\,(D_{x,e}\,P_{y,e} - D_{y,e}P_{x,e}) \end{aligned} \tag{5.15}$$

where $\vec{D_e}$ and $\vec{D'_e}$ are the normalized spatial parts of the incident and scattered wave 4-vector K_e and K'_e. The temporal component of the wave 4-vector after the scattering is $K'_{t,e} = \dfrac{2\,\pi\,\nu'_e}{c}$ and the spatial components are obtained by the multiplication $K'_{i,e} = K'_t\,\vec{D'_e}$ where $i = 1, 2, 3$.

stokes.pro and lorentz.pro, second call

At this point, the degree of polarization due to scattering, Π, is calculated, in accord to Eq. 4.19. The stokes.pro routine is called again with the direction of the scattered photon in the reference frame of the electron, K'_e, and the degree of polarization due to scattering, Π, as inputs. The only difference with respect to the first call is that if $\xi \leq \Pi$, the polarization vector is given by

$$\begin{aligned} P'_{x,e} &= D'_{x,e}\,\sin\Theta_{sc}\cos\Phi_{sc} - P_{x,e} \\ P'_{y,e} &= D'_{y,e}\,\sin\Theta_{sc}\cos\Phi_{sc} - P_{y,e} \\ P'_{z,e} &= D'_{z,e}\,\sin\Theta_{sc}\cos\Phi_{sc} - P_{z,e} \end{aligned} \tag{5.16}$$

as described in Matt et al. 1996 [45]. Otherwise the polarization vector is randomly constructed in accord to equation 4.6.

In the end of the scattering loop, the wave 4-vector and the polarization vector of the scattered photon are anti-transformed back in the reference

frame of the disc by calling for the second time the routine lorentz.pro where the vector $\vec{\beta}$ is substituted with $-\vec{\beta}$. The coordinates of the photon, its wave 4-vector and its polarization vector are updated for a new possible scattering event, starting with the calculation of the speed of the electron in maxrel.pro.

finalpol.pro

When a photon escape towards the observer, finalpol.pro is called by the main procedure to calculate the final Stokes parameters of the survived photon, by using its direction and polarization vector in the reference frame of the disc through the auxiliary vectors and Eq. 4.5.

In the end the direction angles, Θ_d and Φ_d, the energy, $E = h\nu_d$, the Stokes parameters, U_j and Q_j, and the number of undergone scatterings are saved and a new seed photon is generated. Outside the main loop, overall statistics about the number of photons survived or fallen into the BH or onto the disc are saved.

Finally the degree of polarization and the polarization angle are calculated in accord to the relations

$$\begin{aligned} \Pi &= \frac{\sqrt{Q^2 + U^2}}{I} \\ \chi &= \frac{1}{2} \arctan \frac{U}{Q} \end{aligned} \tag{5.17}$$

Chapter 6

Results

In this chapter the results of the simulations are shown. In the first part of the chapter the Spectral Energy Distributions (SEDs) for the two studied cases are reported: the Iron-line emission for galactic BHs and the continuum emission for SMBHs. In the second part, the results on polarization degree and angle for the two cases will be discussed.

Before starting, it is useful to show some figures on the overall population of photons, in order to better understand the plots which follow. In the table below, all four cases (2 corona geometries times 2 optical depth) considered for continuum emission are shown. Every case consists of 10^8 input photons, which then divide in those fallen onto the disc, those fallen into the BH and those escaped towards the observer (first three rows). The fourth row shows the percentage of escaped photons, out of the total, which have not experienced any scattering (so directly from the disc to the observer). In the fifth row the percentage of scattered photons out of the total is shown, and on the last three rows the sub-percentages of survived ones (i.e. escaped), fallen onto the disc or fallen into the BH, out of the scattered photons, are shown.

[BB seed photons]	SPHERICAL		SLAB	
	$\tau = 0.1$	$\tau = 1$	$\tau = 0.1$	$\tau = 1$
Disc (lost)	2%	14%	7%	41%
BH (lost)	0%	1%	0%	1%
Escaped (total)	98%	85%	93%	58%
Escaped (with no scatterings)	96%	72%	86%	25%
Scattered	4%	28%	14%	75%
of which:				
- survived	50%	47%	50%	44%
- Disc (lost)	49%	51%	49%	55%
- BH (lost)	1%	2%	1%	1%

Table I

As one can easily see, the SLAB corona is more efficient than the SPHERICAL corona in terms of scatterings. This is due to the fact that, as mentioned at the beginning of chapter 6, the optical depth, for the SLAB geometry, is defined vertically with respect to plane of the disc. Therefore photons traveling in the corona almost disc-parallel experience an higher optical depth and this quantity, obviously, plays a critical role with respect to the number of scatterings. The drawback is that more than one half of the input photons fall into the BH or onto the disc and are lost. Looking at the sixth and seventh rows, it can be noticed that for all scenarios, on the average, a little bit more than one half, for $\tau = 1$, and a little bit less than one half, for $\tau = 0.1$, of the scattered photons survives and reaches the observer while the other half falls onto the disc, as expected.

In the following the same table for K_α seed photons is shown. The total number of input photons for every case, in this instance, is equal to 5×10^7.

[K_α seed photons]	SPHERICAL		SLAB	
	$\tau = 0.1$	$\tau = 1$	$\tau = 0.1$	$\tau = 1$
Disc (lost)	3%	23%	11%	45%
BH (lost)	1%	3%	1%	8%
Escaped (total)	96%	74%	88%	47%
Escaped (with no scatterings)	93%	55%	77%	18%
Scattered	7%	45%	23%	82%
of which:				
- survived	50%	44%	49%	38%
- Disc (lost)	50%	54%	50%	57%
- BH (lost)	0%	2%	1%	5%

Table II

The results are similar to the previous ones except for an overall higher number of scattered photons, due to the fact that the energy of seed photons, $6.4\,keV$, is closer to the thermal energy of the electrons, $2\,keV$, and therefore scattering events are more probable.

Even if the input is doubled in the continuum emission case with respect to the line emission one, the statistics is not good enough. The results we are going to show for the continuum emission are still preliminary and have to be considered only qualitative.

6.1 Spectral Energy Distributions

For K_α seed photons, the initial SED is a Dirac δ function centered at $6.4\,keV$. In Fig. 6.1 the SEDs produced by a SPHERICAL corona (black solid line) and by a SLAB corona (red dashed line) at $kT = 2\,keV$ with $\tau = 0.1$ are shown. In Fig. 6.2 the SEDs for $\tau = 1$ are shown.

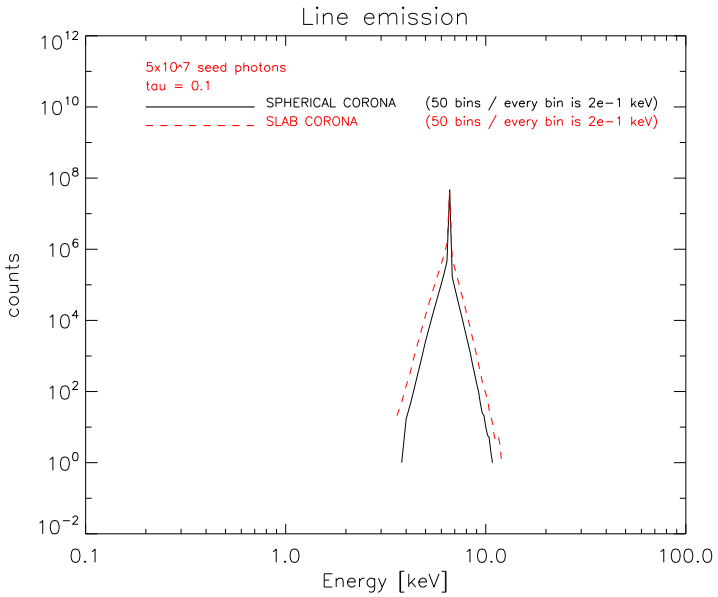

Figure 6.1: *Spectral energy distribution for* 5×10^7 K_α *photons scattered by a SPHERICAL (black solid line) and a SLAB (red dashed line) cloud of relativistic but thermal electrons at* $kT = 2\,keV$ *with optical depth* $\tau = 0.1$.

A comparison between SEDs generated by the two geometries with the same optical depth confirms, through a larger broadening of the line, the higher scattering efficiency of the SLAB corona. In all four cases the broadening of the line is asymmetric with larger tails at low energy. This is due to the fact that the thermal energy of the corona is $2\,keV$, lower than the energy of K_α photons.

In Fig. 6.3 the spectral energy distribution of BB seed photons is shown. The spectrum is the multi-temperature blackbody emission produced by optically thick and geometrically thin accretion discs and represents the input spectrum for the continuum emission scenario. The peak, around $10\,eV$, correspond to UV emission, as expected for a SMBH with a mass of $10^8\,M_\odot$.

In Fig. 6.4 the spectral energy distributions produced by a SPHERICAL (black solid line) and a SLAB (red dashed line) corona at $kT = 100\,keV$ with $\tau = 0.1$ is shown. In Fig. 6.5 the SEDs for $\tau = 1$ are shown.

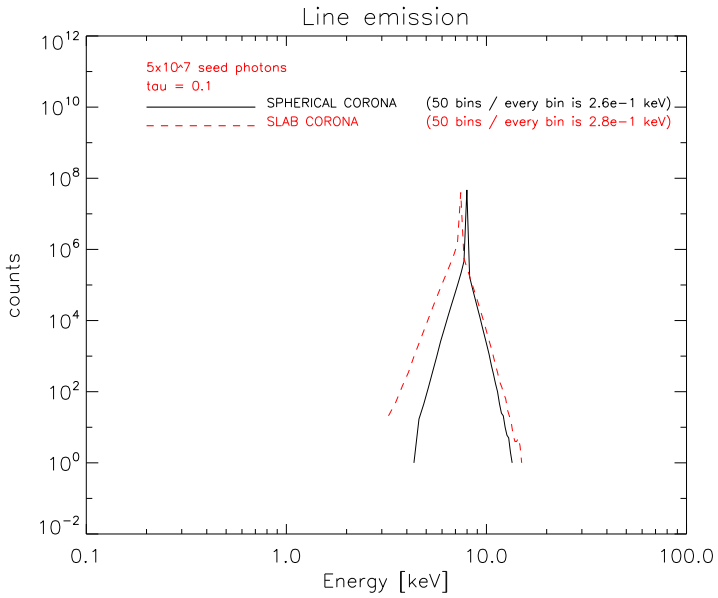

Figure 6.2: *Same as Fig. 6.1 but for* $\tau = 1$.

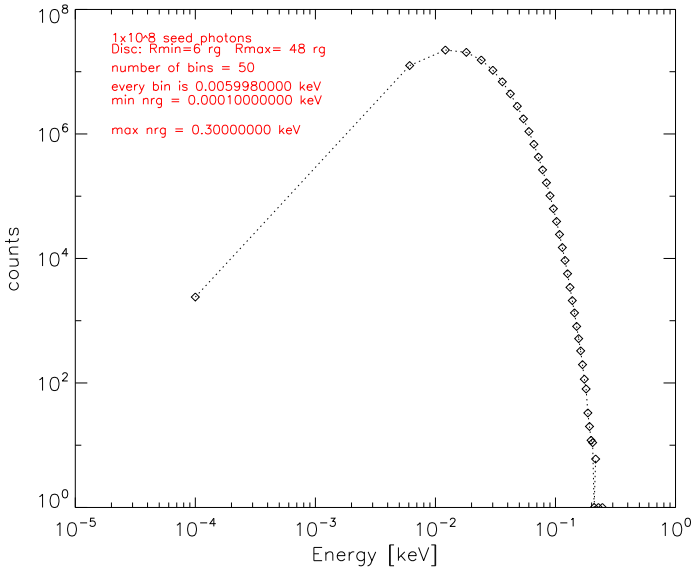

Figure 6.3: *Spectral energy distribution for* 10^8 *photons generated by an optically thick and geometrically thin accretion disc. The multi-temperature blackbody spectrum peaks around* $10\,eV$*, as expected for a SMBH with a mass of* $10^8\,M_\odot$.

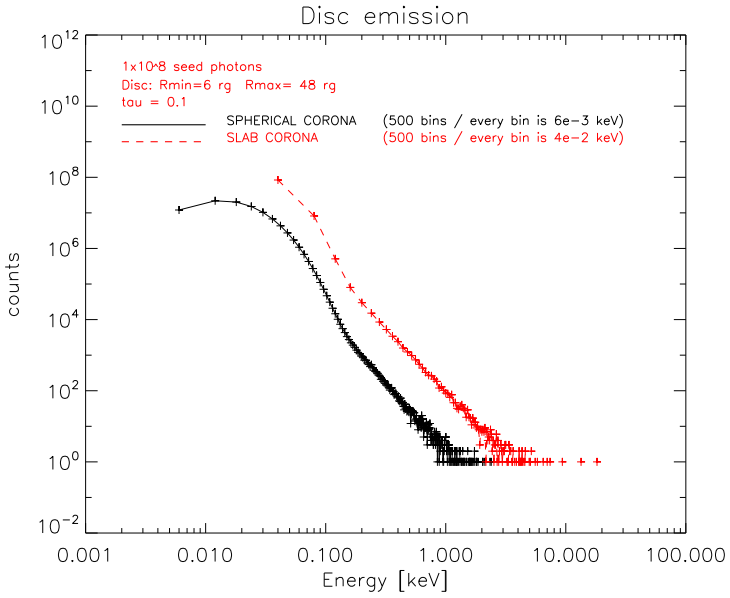

Figure 6.4: *Spectral energy distribution for* 10^8 *BB seed photons scattered by a SPHERICAL (black solid line) and a SLAB (red dashed line) cloud of relativistic but thermal electrons at* $kT = 100\,keV$ *with optical depth* $\tau = 0.1$. *Every cross indicates the counts up to that energy.*

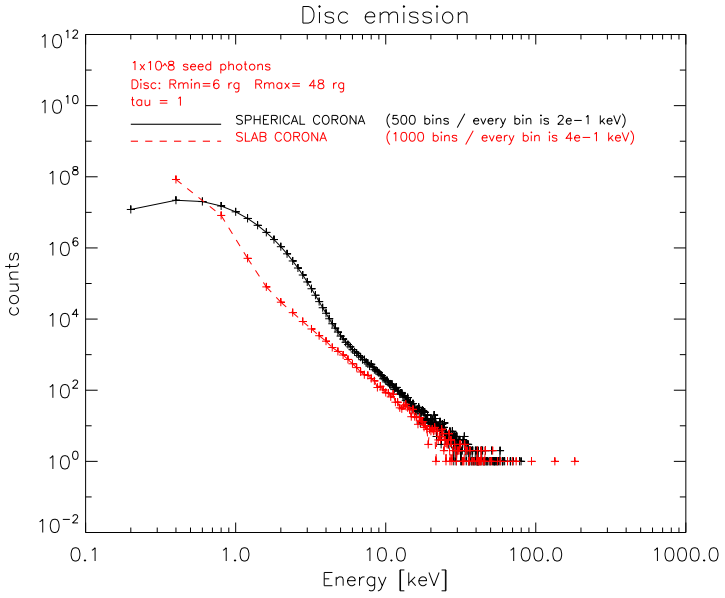

Figure 6.5: *Same as Fig. 6.4 but for* $\tau = 1$.

For the optically thin geometries we built the SEDs using 500 bins in the range $0 - 3\,keV$ for the SPHERICAL corona and in the range $0 - 20\,keV$ for the SLAB one. For the optically thick geometries we divided the range $0-100\,keV$ in 500 bins for the SPHERICAL corona and the range $0-400\,keV$ in 1000 bins for the SLAB one. In the optically thin cases the contribution of the disc is clearly visible up to $0.1\,keV$. Above this energy photons are distributed as a power law, as expected if Comptonized by relativistic but thermal electrons. For the optically thick SPHERICAL corona (black solid line in Fig. 6.5) the bump up to $5\,keV$ is due to first-order Comptonized photons. For both the geometries, above $5\,keV$ the photons are distributed as a power law. The expected thermal cut-off above $100\,keV$ and the contribution of the disc below $1\,keV$ are not visible due to poor statistics.

6.2 Polarization signal

In this section we are going to show the plots on polarization degree and polarization angle. We binned the signals both in cosine of the polar angle, $\mu = \cos(\Theta)$, and in energy. If not specified, we binned the signal using 50 bins both for μ and energy. Θ is the angle at which the photons escape towards the observer and so can be meant also as the viewing angle. We remind that $\mu = 1$ correspond to the direction perpendicular to the plane of the disc (i.e. face-on angle of view) while $\mu = 0$ correspond to the direction parallel to the plane of the disc (edge-on view). For both polarization degree and angle, bins containing less than one milionth of the total number of photons (hence 100 for BB photons and 50 for K_α photons) are automatically set to zero in order to avoid spikes generated by too low statistics. We are going to describe first the polarization degree and angle of the simplest case, the Iron-line emission.

6.2.1 Line emission

Θ binning

Polarization Degree

In Fig. 6.6 we show the polarization degree, binned in μ, for K_α photons generated by a disc surrounded by a SPHERICAL corona with $\tau = 0.1$ is shown. In this plot and all the following plots, the dot-dashed blue line represent the contribution of the unscattered photons, the dashed red line is the contribution of scattered photons and the solid black line the total of the two. In Fig. 6.7 the same plot of Fig. 6.6 but for $\tau = 1$ is shown.

In Fig. 6.8 and 6.9 the degree of polarization, binned in μ, for a SLAB corona with optical depth $\tau = 0.1$ and $\tau = 1$, respectively, is shown.

In all four cases, the contribution of unscattered photons to the degree of polarization (DOP) is zero, because, in the line emission case, seed photons are initially unpolarized (i.e. randomly polarized). For the SPHERICAL corona, at both optical depths, the contribution of unscattered photons dominates and therefore the total DOP is negligible. For SLAB geometry, in the optical thin regime, the total DOP is a few percent $(1 - 2\%)$ while it reaches $5 - 6\%$ in the optically thick regime. The lower DOP of scattered photons (red dashed line) in the optically thick regime with respect to the optically thin one for SLAB geometry (Fig. 6.8 and Fig. 6.9) is due to the fact that multiple scatterings randomize the polarization vector, decreasing the DOP with respect to single scatterings.

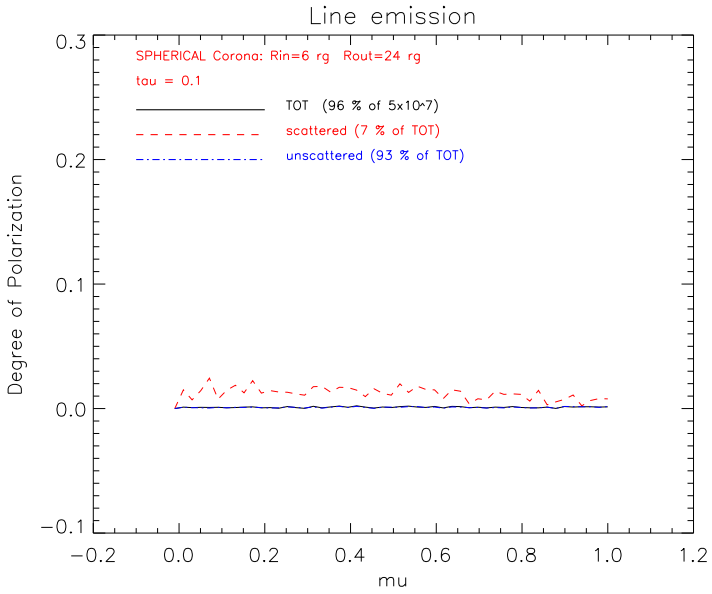

Figure 6.6: *Polarization degree for* 5×10^7 K_α *photons scattered by a SPHERICAL cloud of relativistic but thermal electrons at* $kT = 2\,keV$ *with optical depth* $\tau = 0.1$. *The dot-dashed blue line represent the contribution of the unscattered photons, the dashed red line is the contribution of scattered photons and the solid black line the total of the two.*

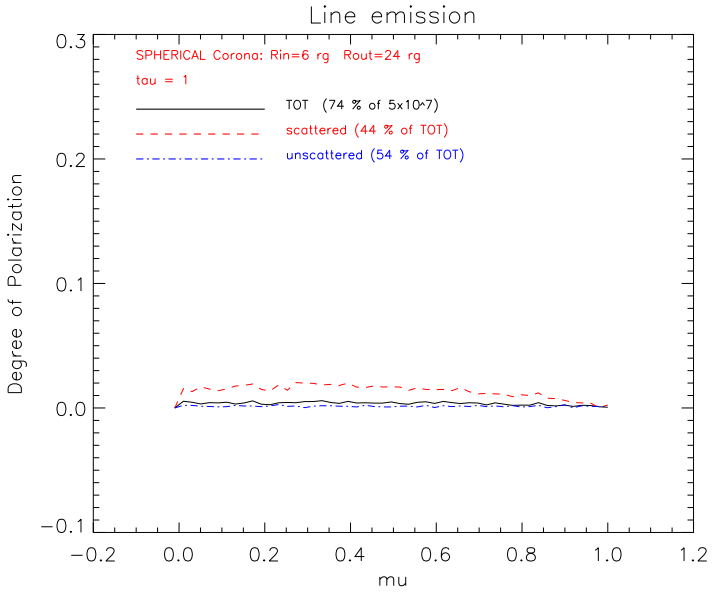

Figure 6.7: *Same as Fig. 6.6 but for* $\tau = 1$.

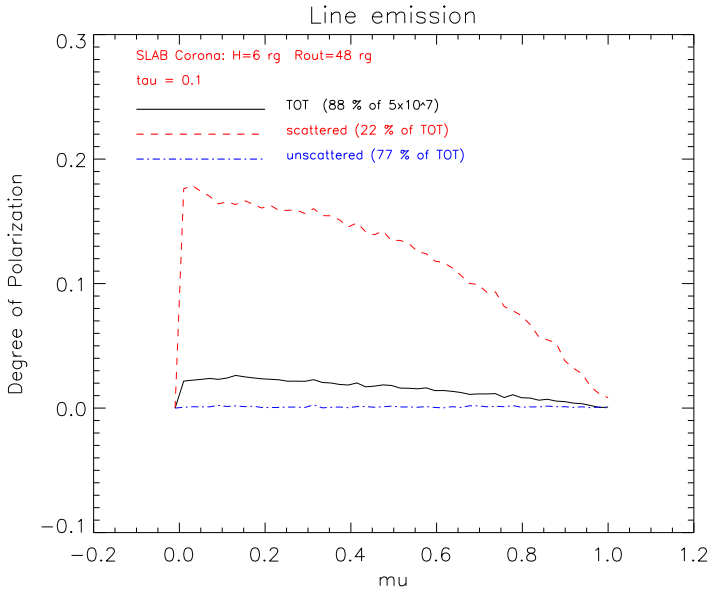

Figure 6.8: *Same as Fig. 6.6 but for a SLAB corona with* $\tau = 0.1$.

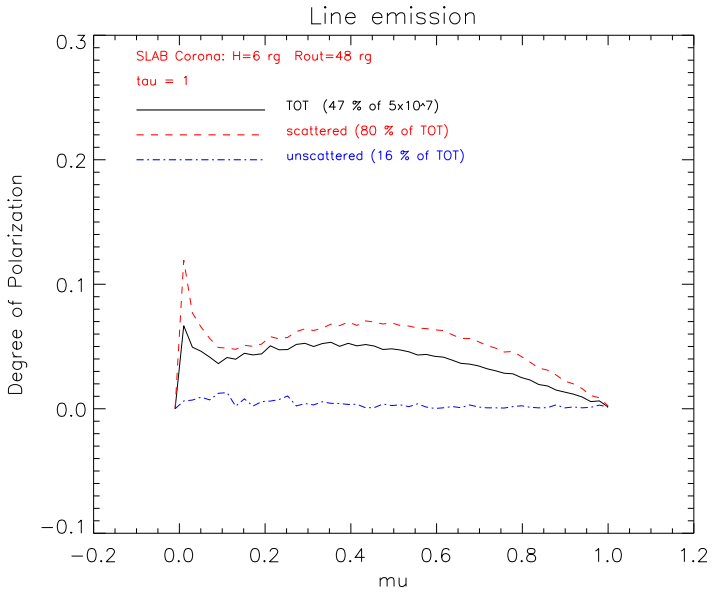

Figure 6.9: *Same as Fig. 6.8 but for* $\tau = 1$.

Polarization Angle

The interpretation of the polarization angle is less straightforward than the polarization degree. Assuming that the y-axis of an hypothetical polarimeter is parallel to the projected symmetry axis of the BH and accretion disc system, the polarization angle is measured from the line obtained by the intersection of the polarization plane, tangent to the propagation of the photon, with the plane of the disc. The polarization angle does not have the sign defined. 0 means that the polarization vector is parallel to the plane of the accretion disc ('horizontal') while $+\pi/2$ or $-\pi/2$ means that it is perpendicular with respect to the plane of the disc ('vertical'). Given the axisymmetric geometries we are exploring, we expect the polarization angle of the scattered radiation to be either purely horizontal or vertical. In our plots we show the modulus of the polarization angle belonging to the interval $[0, \pi/2]$. In Fig. 6.10 the polarization angle for 5×10^7 K_α photons scattered by a SPHERICAL cloud of relativistic but thermal electrons at $kT = 2\,keV$ with optical depth $\tau = 0.1$ is shown. As previously, the dot-dashed blue line represent the contribution of the unscattered photons, the dashed red line is the contribution of scattered photons and the solid black line the total of the two.

In Fig. 6.11 the same plot of Fig. 6.10 but for $\tau = 1$ is shown.

In Fig. 6.12 and 6.13 the degree of polarization, binned in μ, for a SLAB corona with optical depth $\tau = 0.1$ and $\tau = 1$, respectively, is shown.

In all four plots, the polarization angle of unscattered photons (blue dot-dashed line) randomly assumes every value among all the possible (between 0 and $\pi/2$), as expected for unpolarized (i.e. randomly polarized) radiation. Scattering events produce a linear polarization in the vertical direction (i.e $\pi/2$) with respect to the plane of the disc (red dashed lines). A similar effect has been also found by Schnittmann and Krolik, 2010 [66].

For SPHERICAL corona, in the optically thin regime, the contribution of unscattered photons is prevailing and the total polarization angle (black solid line) is random. In the optically thick regime and for SLAB geometry of the corona, in both the optical depths regimes, the total polarization angle is vertical. This is due to the fact that the total polarization angle is determined by the polarized radiation, even if small with respect to the unpolarized one. This is not true for the polarization degree (see Eq. 5.17).

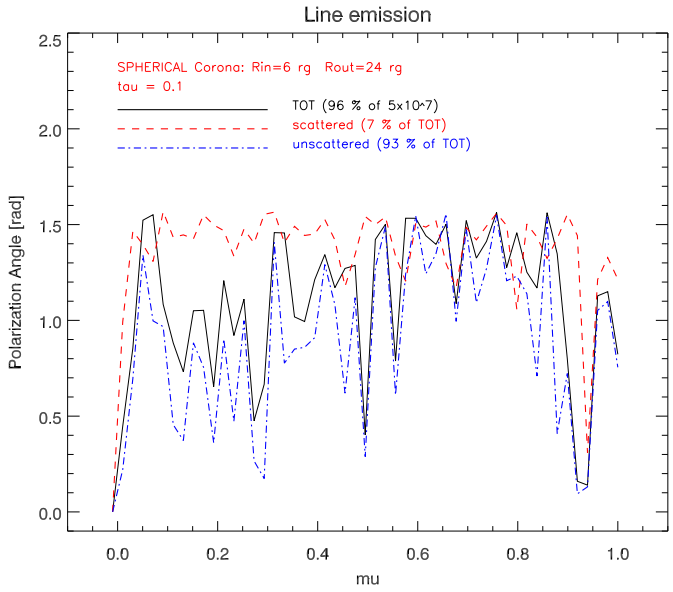

Figure 6.10: *Polarization angle for* 5×10^7 K_α *photons scattered by a SPHERICAL cloud of relativistic but thermal electrons at* $kT = 2\,keV$ *with optical depth* $\tau = 0.1$. *The dot-dashed blue line represent the contribution of the unscattered photons, the dashed red line is the contribution of scattered photons and the solid black line the total of the two.*

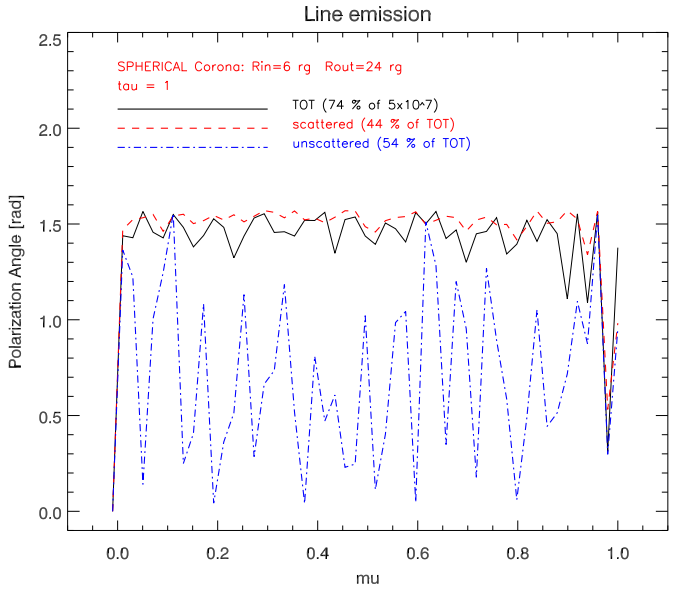

Figure 6.11: *Same as Fig. 6.10 but for* $\tau = 1$.

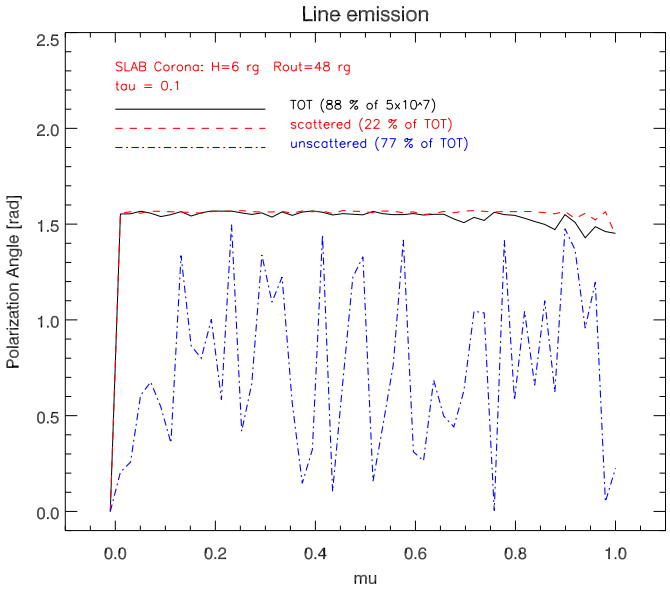

Figure 6.12: *Same as Fig. 6.10 but for a SLAB corona with* $\tau = 0.1$.

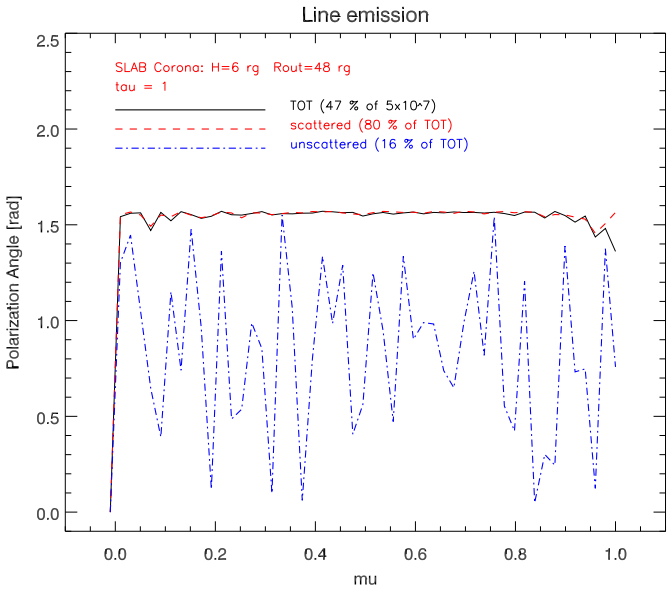

Figure 6.13: *Same as Fig. 6.12 but for* $\tau = 1$.

Energy binning

Polarization Degree

In this subsection we are going to show the polarization signal binned in energy. The binning in the polar angle Θ is important to check at which angle of view the polarization degree is maximum and how, eventually, changes the polarization angle as a function of it. The binning in energy, on the other hand, represents how the polarization signal is measured by a polarimeter and allows to evaluate which is the more convenient energy band in terms of amplitude of the signal. As said at the beginning of the chapter, when less than one milionth of counts (i.e. 100 counts) out of the total (10^8) were found in one energy bin, both the polarization degree and angle are automatically set to zero. In Fig. 6.14 the polarization degree, binned in energy, for K_α photons generated by a disc surrounded by a SPHERICAL corona with $\tau = 0.1$ is shown.

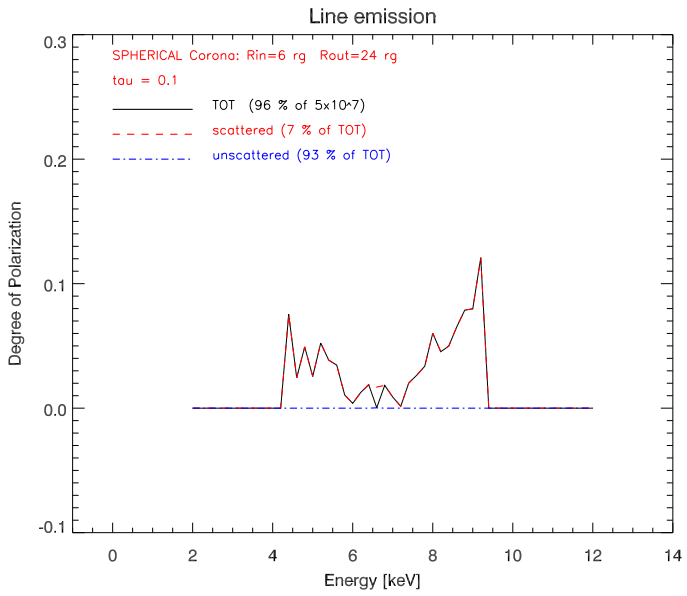

Figure 6.14: *Polarization degree for* 5×10^7 K_α *photons scattered by a SPHERICAL cloud of relativistic but thermal electrons at* $kT = 2\,keV$ *with optical depth* $\tau = 0.1$. *The dot-dashed blue line represent the contribution of the unscattered photons, the dashed red line is the contribution of scattered photons and the solid black line the total of the two.*

In Fig. 6.15 the same plot of Fig. 6.14 but for $\tau = 1$ is shown.

In Fig. 6.16 and 6.17 the degree of polarization, binned in energy, for a SLAB corona with optical depth $\tau = 0.1$ and $\tau = 1$, respectively, is shown.

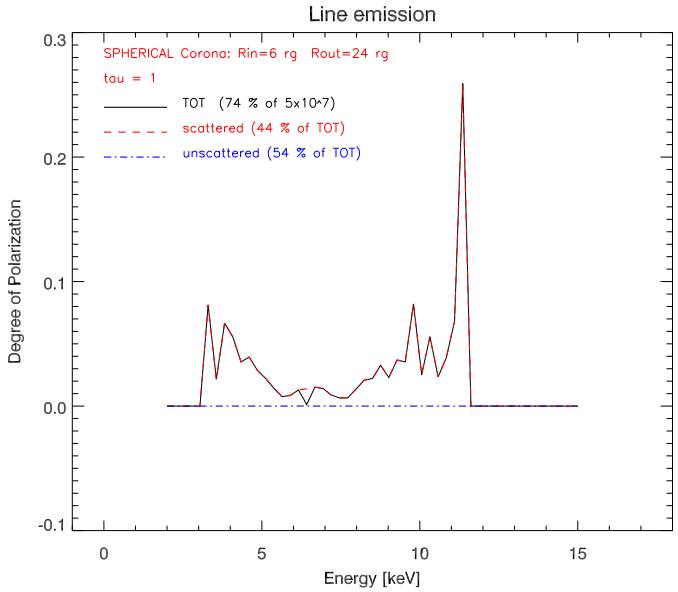

Figure 6.15: *Same as Fig. 6.14 but for* $\tau = 1$.

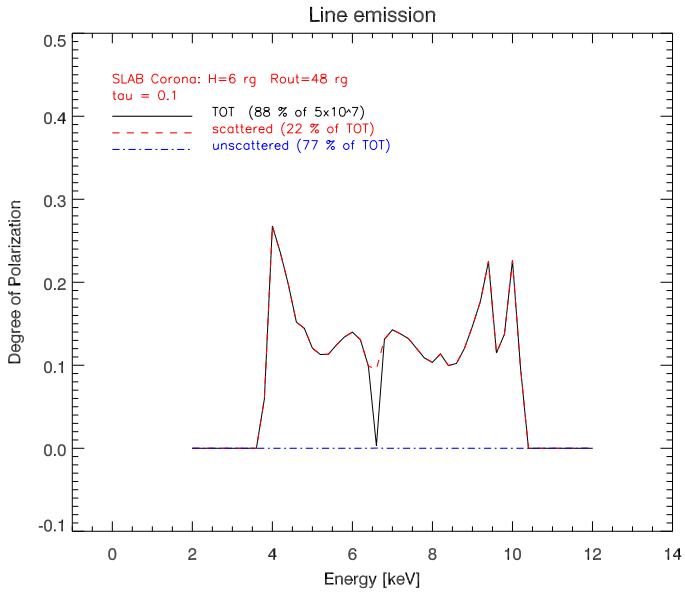

Figure 6.16: *Same as Fig. 6.14 but for a SLAB corona with* $\tau = 0.1$.

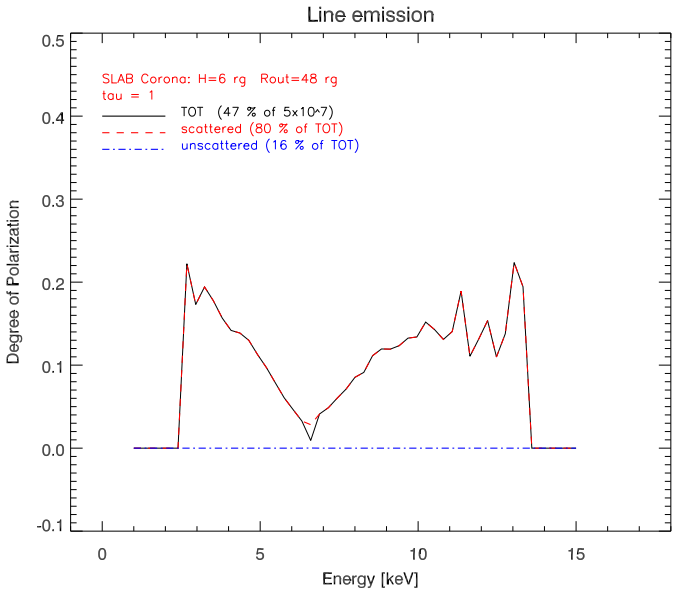

Figure 6.17: *Same as Fig. 6.16 but for* $\tau = 1$.

As in the μ binning, the polarization degree of unscattered photons (blue dot-dashed line) is zero all over the range. In this case, the total degree of polarization (black solid line) is completely determined by the polarization degree of scattered photons (red dashed line) for both the optical depths and the corona geometries. This is due to the fact that all the unscattered photons are located in the $6.4\,keV$ energy bin where, in fact, they contribute lowering the total degree of polarization.

For the SPHERICAL corona the polarization degree is, on average, around $5 - 10\%$ while for SLAB geometry the DOP is slightly higher. Spikes at the lowest and highest energies are symptoms of low statistics and the polarization degree is large because generated by very few photons. As for the polarization degree binned in angle, for both the geometries, multiple scatterings (i.e. $\tau = 1$) lower the degree of polarization as can be seen by comparing the DOP in the two optical depth regimes in an energy bin with no spikes as, for example, $8\,keV$.

Polarization Angle

In Fig. 6.18 the polarization angle, binned in energy, for K_α photons generated by a disc surrounded by a SPHERICAL corona with $\tau = 0.1$ is shown.

In Fig. 6.19 the same plot of Fig. 6.18 but for $\tau = 1$ is shown.

In Fig. 6.20 and 6.21 the polarization angle, binned in energy, for a SLAB

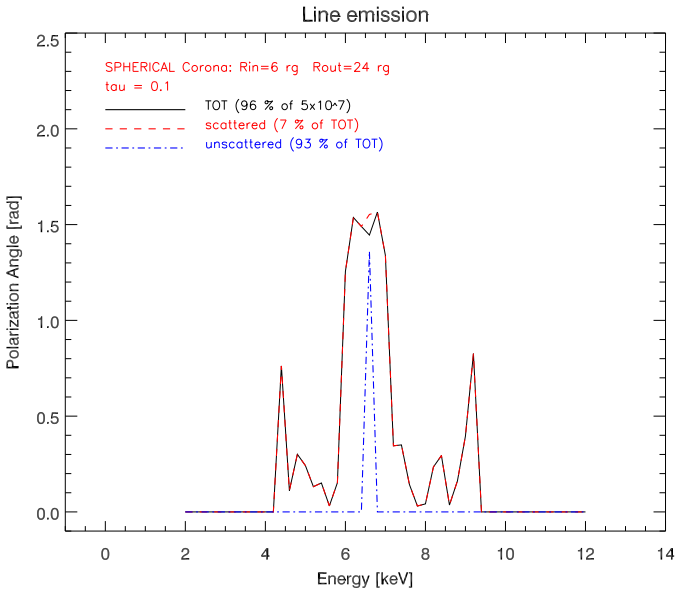

Figure 6.18: *Polarization angle for* 5×10^7 K_α *photons scattered by a SPHERICAL cloud of relativistic but thermal electrons at* $kT = 2\,keV$ *with optical depth* $\tau = 0.1$. *The dot-dashed blue line represent the contribution of the unscattered photons, the dashed red line is the contribution of scattered photons and the solid black line the total of the two.*

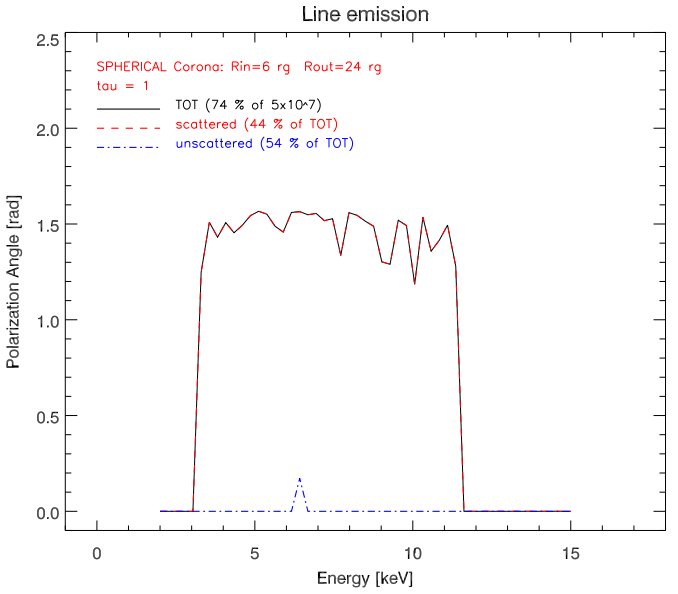

Figure 6.19: *Same as Fig. 6.18 but for* $\tau = 1$.

corona with optical depth $\tau = 0.1$ and $\tau = 1$, respectively, is shown.

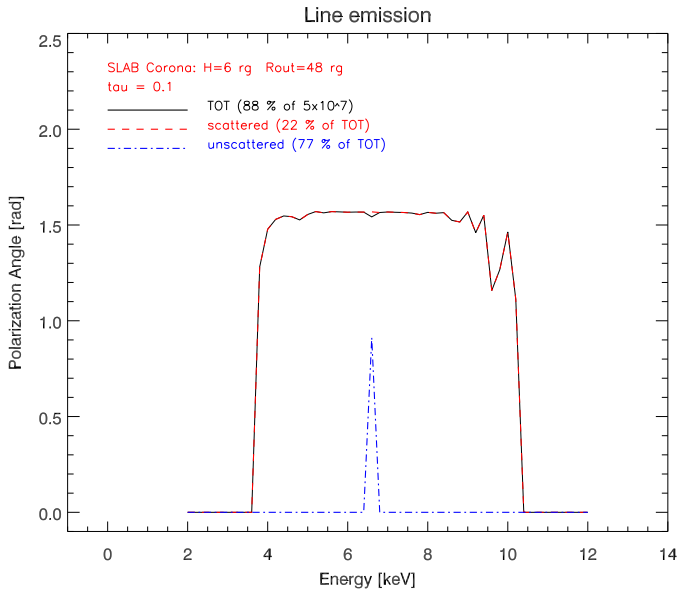

Figure 6.20: *Same as Fig. 6.18 but for a SLAB corona with* $\tau = 0.1$.

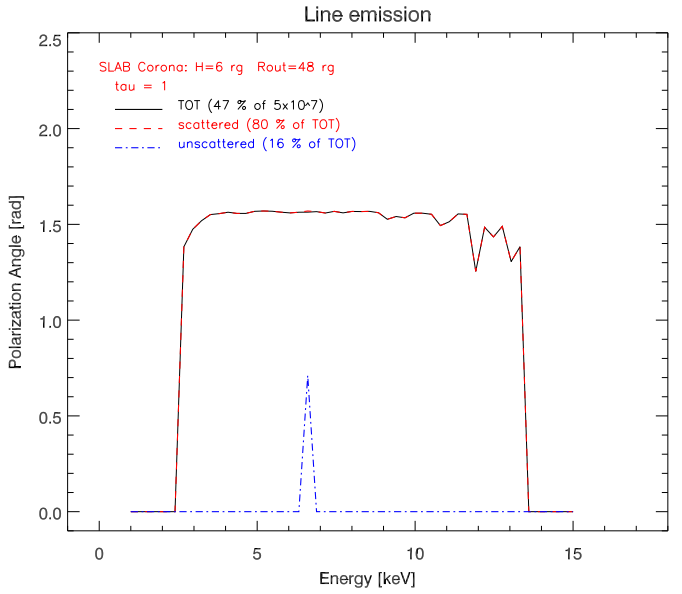

Figure 6.21: *Same as Fig. 6.20 but for* $\tau = 1$.

In all four plots, unpolarized photons (blue dot-dashed line) exhibit a

spike in the energy bin where they are located (around $6.4\,keV$). This spike has no physical meaning and represents the random angle of unpolarized radiation which degree is zero.[1]

As for the degree of polarization binned in energy, the total polarization angle (black solid line) is completely determined by the contribution of scattered photons and the two curves perfectly overlap in all four scenarios. We showed before, in the μ binned polarization angle subsection, that scatterings produce a vertical linear polarization, i.e. perpendicular to the plane of the disc. This results is clearly visible also in the energy binned plots where the polarization angle is $\pi/2$ all over the band, apart in Fig. 6.18 where statistics is bad because the number of scattered photons in a SPHERICAL corona with $\tau = 0.1$ is very small.

6.2.2 Disc emission

In this subsection we are going to show the results on polarization signal produced by Comptonization of BB seed photons generated by an accretion disc with inner radius equals to $6\,r_g$ and outer radius equals to $48\,r_g$ by a corona of relativistic electrons with thermal energy $kT = 100\,keV$. We remind the reader that the results on disc emission are preliminary due to the lack of good statistics.

Θ binning

Polarization Degree

As for the K_α emission, let us start with the plots on polarization degree binned in μ. In Fig. 6.22 the polarization degree, binned in μ, for BB photons generated by a disc surrounded by a SPHERICAL corona with $\tau = 0.1$ is shown.

Unlike the line emission case, unscattered photons (blue dot-dashed line) have an intrinsic linear polarization, due to limb polarization effect predicted by Chandrasekhar in 1960 [7]. The degree of polarization is zero for photons emitted perpendicularly to the disc ($\mu = 1$) and reaches the maximum value of $\sim 12\%$ for photons emitted in parallel to the plane of the disc ($\mu = 0$). For the SPHERICAL corona, in the optically thin regime, the contribution

[1] In Fig. 6.14, 6.15, 6.16 and 6.17 unscattered photons are located in the energy bin around $6.4\,keV$ and the polarization degree is zero. This 'zero' is the sum of all the random Stokes parameters of unpolarized photons divided by their number so it is not perfectly zero but it is a very low value. Therefore those spikes only represent the average of all the random orientation of the $\vec{P}$ vector of unpolarized photons and have not physical meaning. In general, where the polarization degree is zero, the polarization angle is meaningless.

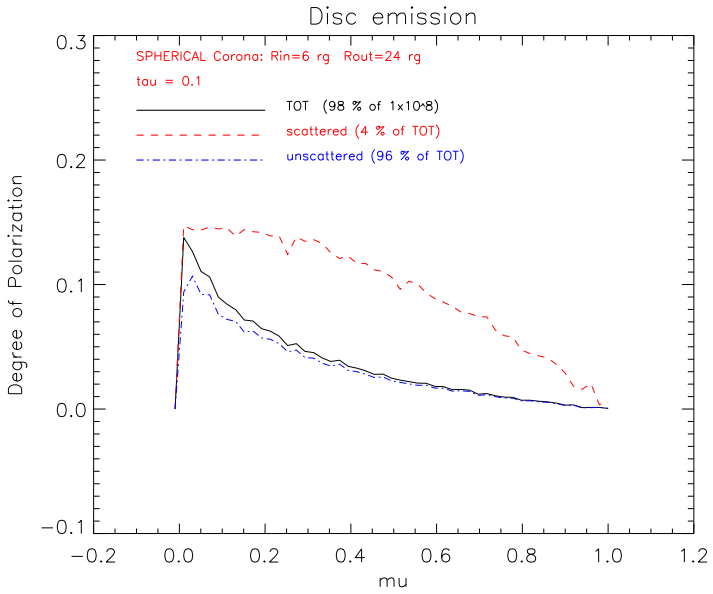

Figure 6.22: *Polarization degree for* 10^8 *BB photons scattered by a SPHERICAL cloud of relativistic but thermal electrons at* $kT = 100\,keV$ *with optical depth* $\tau = 0.1$. *The dot-dashed blue line represent the contribution of the unscattered photons, the dashed red line is the contribution of scattered photons and the solid black line the total of the two.*

of unscattered photons is dominating with respect to scattered photons (red dashed line), therefore the total DOP (black solid line) is substanitially those produced by the optically thick atmosphere of the disc. In the polar angle bin $\mu \sim 0$, the amount of unscattered photons is negligible (see Fig. 5.5) and the total DOP is increased by the contribution of scattered photons. In Fig. 6.23 the same plot of Fig. 6.22 but for $\tau = 1$ is shown.

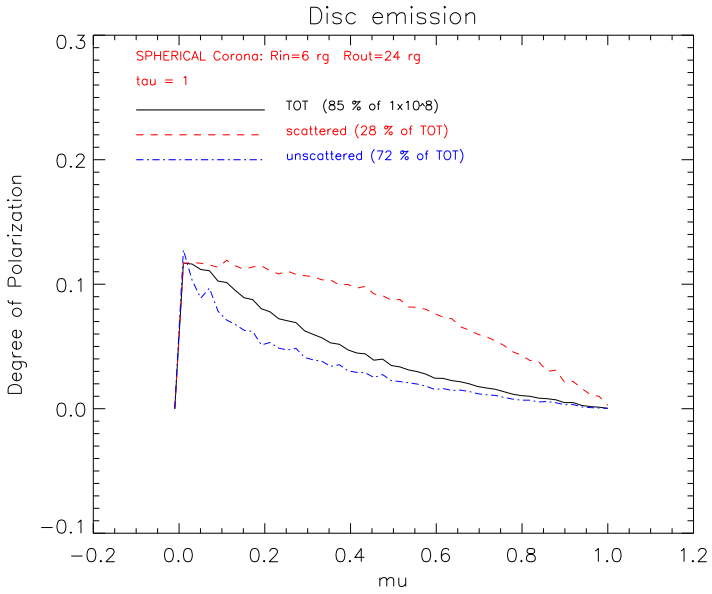

Figure 6.23: *Same as Fig. 6.22 but for* $\tau = 1$.

As observed before, multiple scatterings reduce the degree of polarization (compare the red dashed line in Fig. 6.23 with that in Fig. 6.22). Nonetheless, the increased percentage of scattered photons over the total produces a slight increase of the total polarization degree. In Fig. 6.24 and 6.25 the degree of polarization, binned in μ, for a SLAB corona with optical depth $\tau = 0.1$ and $\tau = 1$, respectively, is shown.

For the SLAB corona, in the optically thin regime, the total degree of polarization is given by the contribution of initially polarized unscattered photons as for the SPHERICAL corona. For $\tau = 1$, multiple-scattered photons dominate, reducing the total DOP to a maximum value of 6% for photons observed perpendicularly with respect to the plane of the disc.

Polarization Angle

In Fig. 6.26 the polarization angle, binned in μ, for BB photons generated by a disc surrounded by a SPHERICAL corona with $\tau = 0.1$ is shown.

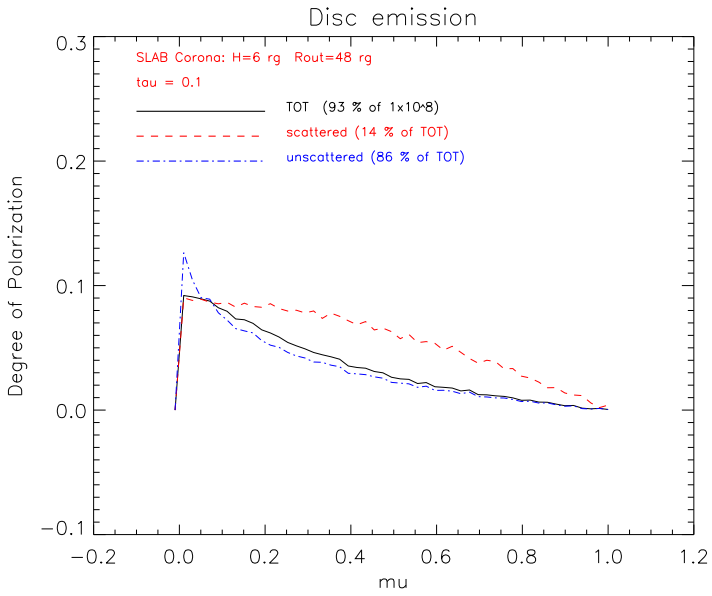

Figure 6.24: *Same as Fig. 6.22 but for a SLAB corona with* $\tau = 0.1$.

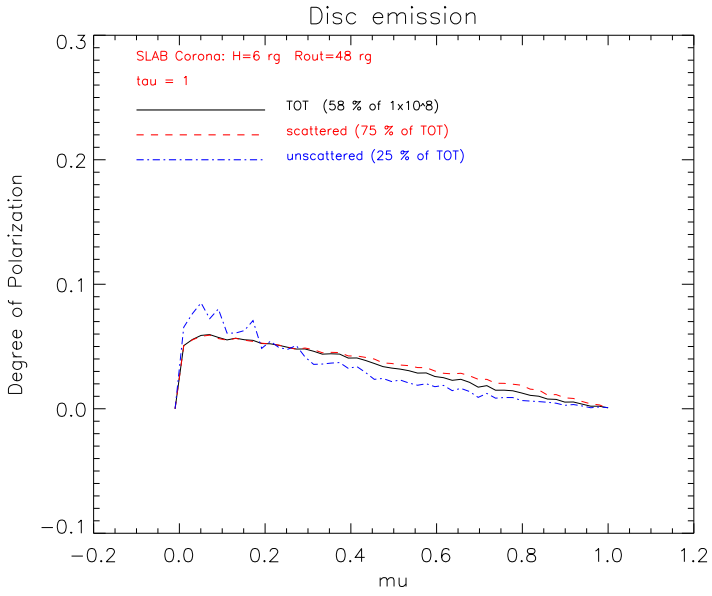

Figure 6.25: *Same as Fig. 6.24 but for* $\tau = 1$.

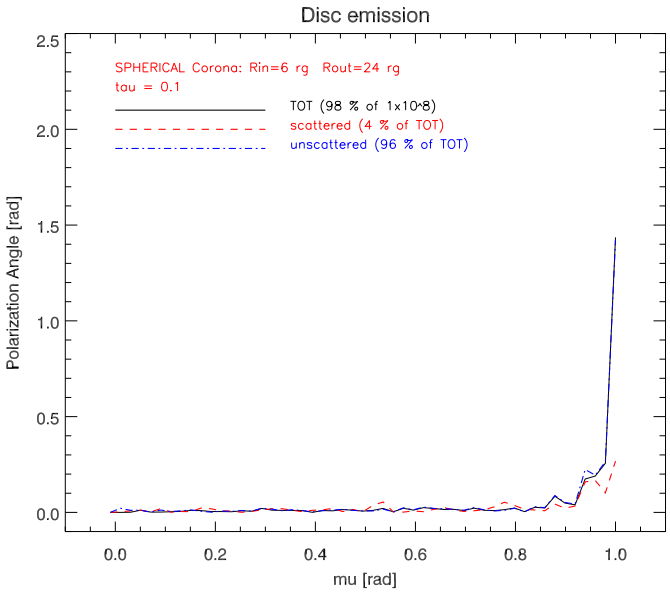

Figure 6.26: *Polarization angle for* 10^8 *BB photons scattered by a SPHERICAL cloud of relativistic but thermal electrons at* $kT = 100\,keV$ *with optical depth* $\tau = 0.1$. *The dot-dashed blue line represent the contribution of the unscattered photons, the dashed red line is the contribution of scattered photons and the solid black line the total of the two.*

Differently from the line emission case, unscattered photons (blue dot-dashed line) are horizontally polarized (polarization angle equals to 0), in accord to Chandrasekhar predictions. The few scattered photons (red dashed line) remain horizontally polarized and the total polarization angle is zero. In Fig. 6.27 the same plot of Fig. 6.26 but for $\tau = 1$ is shown while, in Fig. 6.28 and 6.29, the polarization angle, binned in μ, for a SLAB corona with optical depth $\tau = 0.1$ and $\tau = 1$, respectively, is shown.

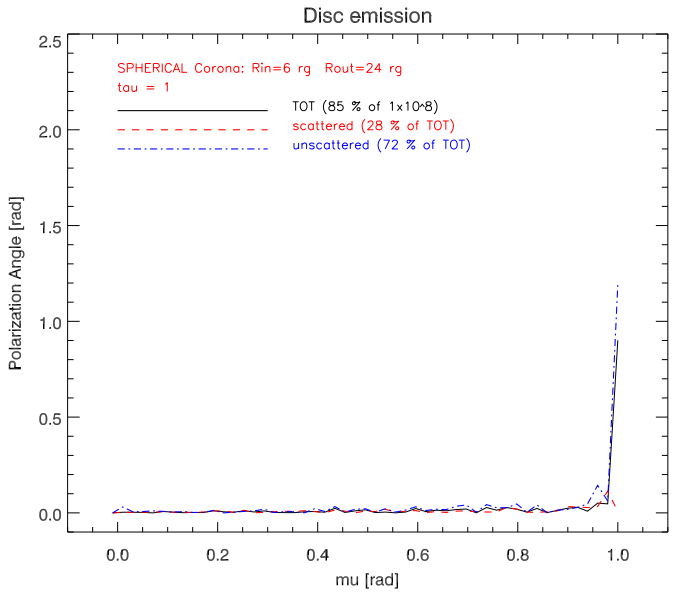

Figure 6.27: *Same as Fig. 6.26 but for* $\tau = 1$.

In all cases the polarization angle of unscattered photons is horizonal, as expected. The polarization angle of scattered photons (red dashed lines) is horizontal as well, differently from the line emission cases. This is due to a combination of two effects. The first one is that a single scattering is not enough to flip the polarization vector from horizontal to vertical. The second one is that most of the photons are emitted perpendicularly to the plane of the disc because of limb darkening effect and this reduce the probability to experience a scattering, especially for the most efficient SLAB geometry. Binning in μ, both one-scattered and multiscattered photons are mixed in every bin and the dominance of one-scattered ones gives a total polarization angle equals to zero in all scenarios.

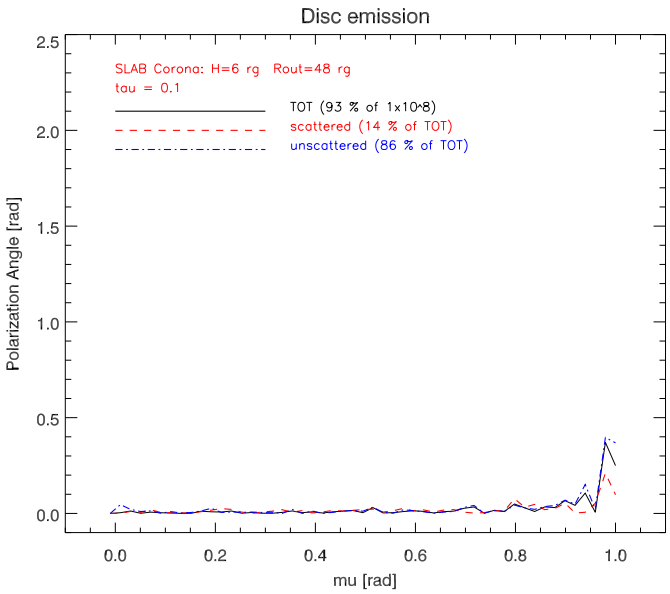

Figure 6.28: *Same as Fig. 6.26 but for a SLAB corona with* $\tau = 0.1$.

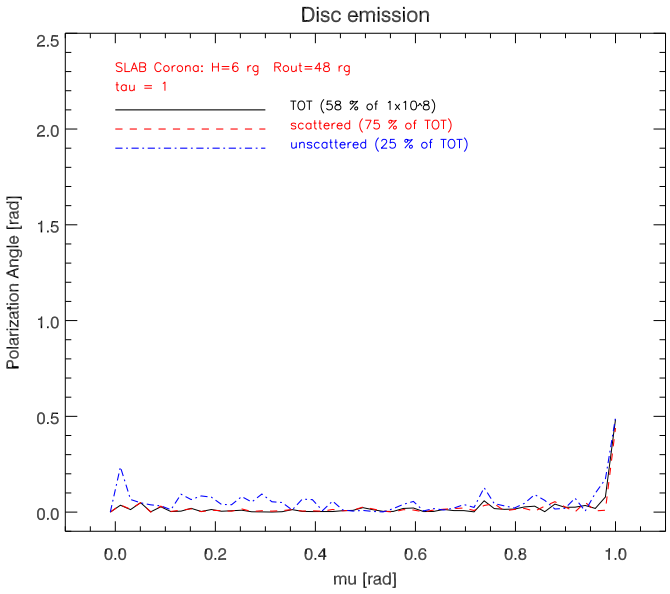

Figure 6.29: *Same as Fig. 6.28 but for* $\tau = 1$.

Energy binning

In this subsection we are going to show the results on polarization signal binned in energy. As for the line emission, when less than 100 counts were found in one bin, both the polarization degree and angle are automatically set to zero.

Polarization Degree

In Fig. 6.30 the polarization degree, binned in energy, for a SPHERICAL corona with $\tau = 0.1$ is shown.

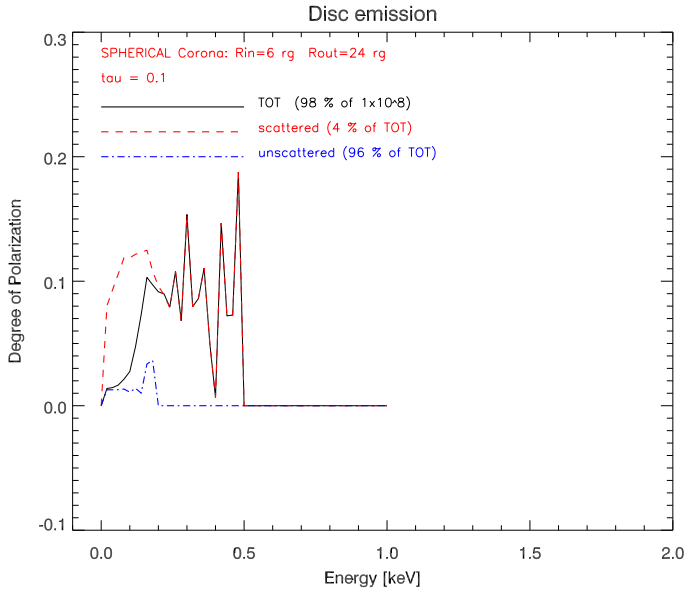

Figure 6.30: *Polarization degree for* 10^8 *BB photons scattered by a SPHERICAL cloud of relativistic but thermal electrons at* $kT = 100\,keV$ *with optical depth* $\tau = 0.1$. *The dot-dashed blue line represent the contribution of the unscattered photons, the dashed red line is the contribution of scattered photons and the solid black line the total of the two.*

Unscattered UV photons (blue dot-dashed line) are produced by the disc and are located below $0.3\,keV$. Their polarization degree is due to the optically thick atmosphere of the disc and is the average between those emitted almost parallel to the plane of the disc with the maximum polarization degree of $\sim 12\%$ (the less of the total) and those emitted perpendicularly to the disc with zero polarization (the most). The averaged degree of initial polarization is around 3%, as shown in figure. In this scenario, scattered

photons (red dashed line) are 4% of the total and one-scattering events are dominating, producing a signal below $0.5\,keV$. The polarization degree, up to $0.3\,keV$ where less spikes are present, is around 10%.

In Fig. 6.31 the same plot of Fig. 6.30 but for $\tau = 1$ is shown.

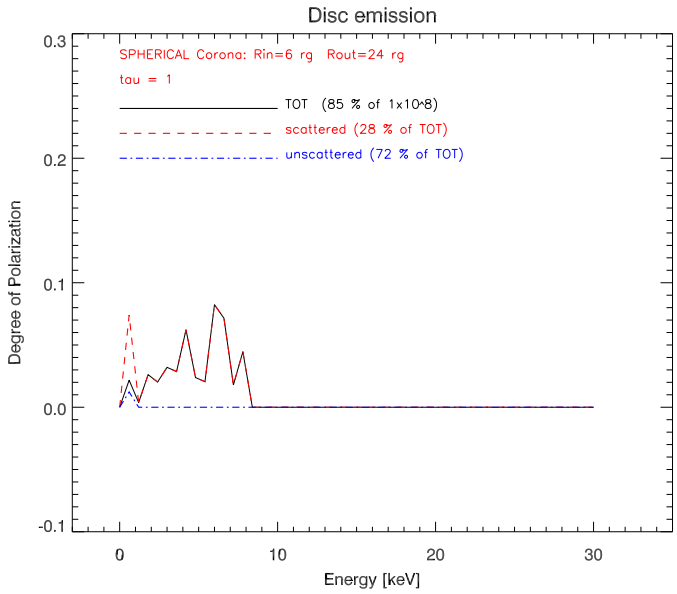

Figure 6.31: *Same as Fig. 6.30 but for* $\tau = 1$.

In the optically thick regime, the percentage of scattered photons is larger and the polarization signal reaches $10\,keV$. The degree of polarization, however, do not exceed 10%. This effect, as seen before, is ascribable to the randomization of the polarization vector by multiple scatterings.

In Fig. 6.32 and 6.33 the degree of polarization, binned in energy, for a SLAB corona with optical depth $\tau = 0.1$ and $\tau = 1$, respectively, is shown.

In the optically thin regime the number of scattered photons (red dashed line) is larger than for the SPHERICAL geometry and the signal reaches $1\,keV$. The average degree of polarization, as for the optically thin SPHERICAL case, is around 10% and the signal is noisy as well. For $\tau = 1$ the multiscattered component is relevant but at high energies (above $40\,keV$) the statistics is poor and the signal is noisy. On the average the total degree of polarization do not exceed the value of 10%, as for the optically thick SPHERICAL geometry case.

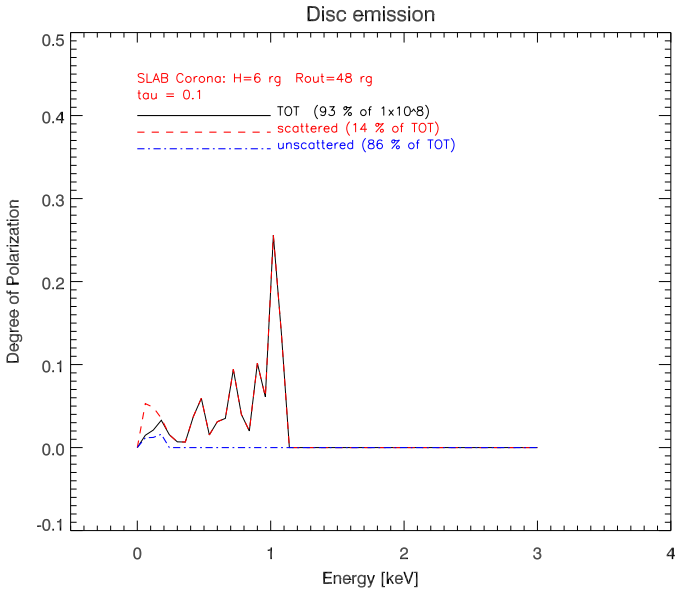

Figure 6.32: *Same as Fig. 6.30 but for a SLAB corona with* $\tau = 0.1$.

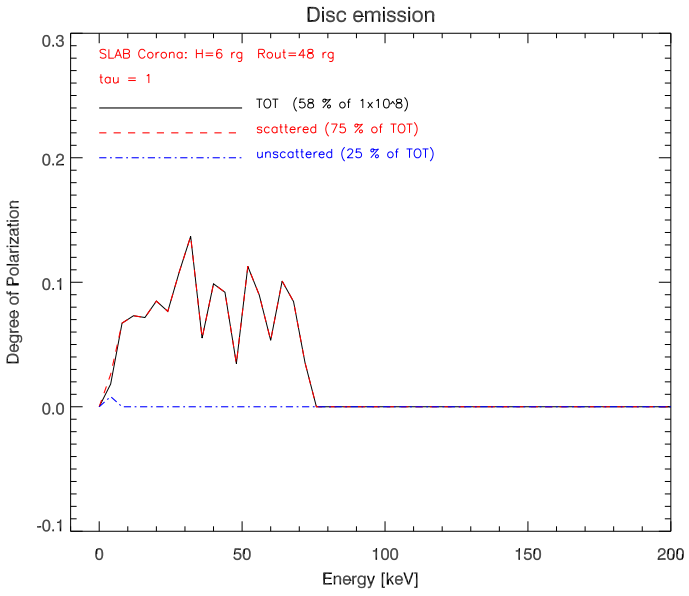

Figure 6.33: *Same as Fig. 6.32 but for* $\tau = 1$.

Polarization Angle

In Fig. 6.34 the polarization angle, binned in energy, for a SPHERICAL corona with $\tau = 0.1$ is shown.

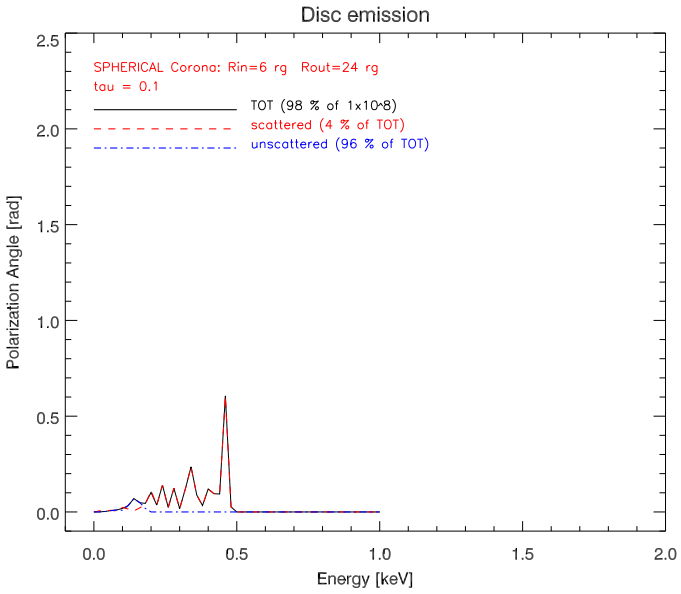

Figure 6.34: *Polarization angle for* 10^8 *BB photons scattered by a SPHERICAL cloud of relativistic but thermal electrons at* $kT = 100\,keV$ *with optical depth* $\tau = 0.1$. *The dot-dashed blue line represent the contribution of the unscattered photons, the dashed red line is the contribution of scattered photons and the solid black line the total of the two.*

Unscattered photons (blue dot-dashed line) are horizontally polarized in accord to Chandrasekhar with polarization angle (almost) equals to zero. In the optically thin regime, the number of scattered photons (red dashed line) is too small and the signal is too much noisy to infer information on the polarization angle.

In Fig. 6.27 the same plot of Fig. 6.26 but for $\tau = 1$ is shown.

In the optically thick case, the number of scattered photons (red dashed line) is larger. Unscattered photons (blue dot-dashed line) are horizontally polarized, as usual, while the scattered ones show a linear vertical polarization with an angle tending to $\pi/2$.

In Fig. 6.36 and 6.37 the polarization angle, binned in energy, for a SLAB corona with optical depth $\tau = 0.1$ and $\tau = 1$, respectively, is shown.

In the optically thin regime, even for the SLAB geometry, we suffer of low statistics and the polarization angle of scattered photon (red dashed line) is

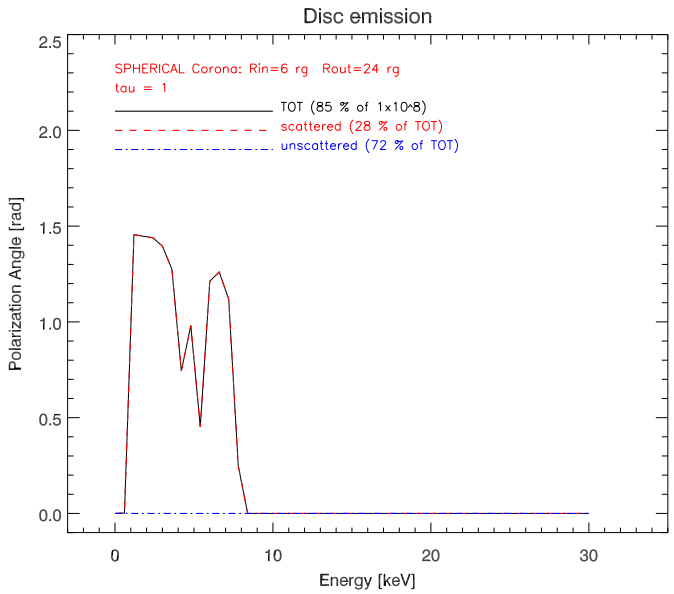

Figure 6.35: *Same as Fig. 6.34 but for* $\tau = 1$.

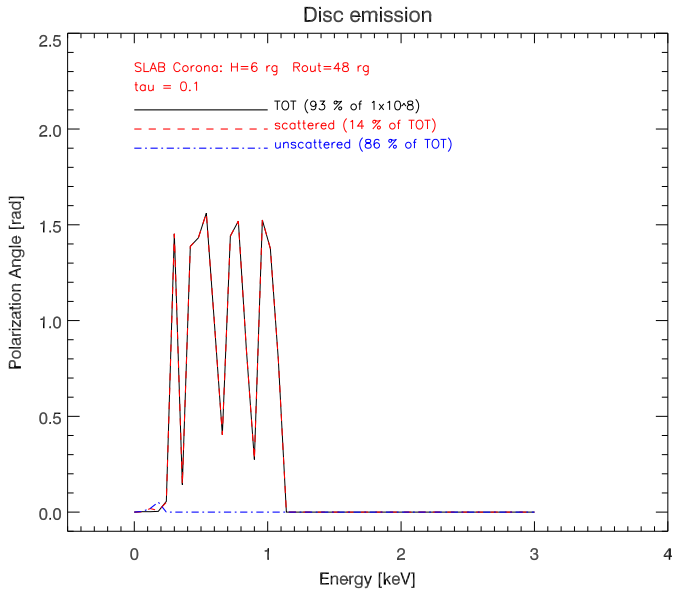

Figure 6.36: *Same as Fig. 6.34 but for a SLAB corona with* $\tau = 0.1$.

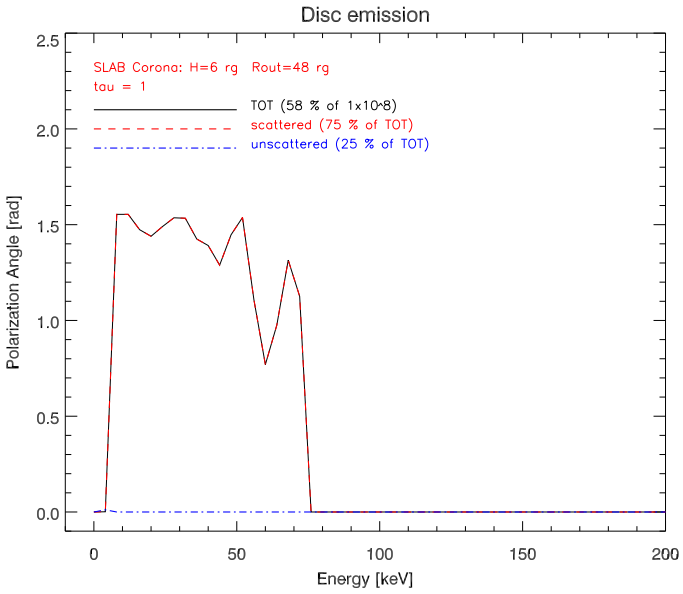

Figure 6.37: *Same as Fig. 6.36 but for* $\tau = 1$.

noisy, as for the SPHERICAL case, and oscillates between 0 and $\pi/2$. In the optically thick regime, the higher number of multiscattered photons (red dashed line) produces a smoother signal which confirms the vertical flipping of the polarization vector induced by multiple scatterings, where the statistics is good enough (below $50keV$).

Chapter 7

Conclusions and Future Developments

The aim of this thesis was to develop a Monte Carlo code devoted to the study of the spectrum and the polarization signal, in X-ray energy band, for accreting systems interesting for Astrophysics. We applied our code to two scenarios of scientific relevance: the properties of the continuum X-ray emission in AGN and the properties of the Iron-line emission in X-Ray Binaries.

With respect to the latter case, we found that Comptonization of monochromatic K_α fluorescence photons generated by the accretion disc can produce a broad emission line. The broadening of the line is directly proportional to the number of scatterings experienced by the photon and therefore to the optical depth of the scattering medium and its geometry. A SLAB corona, completely covering the disc, is far more efficient in terms of scatterings than a SPHERICAL corona surrounding the inner part of the disc. We found also that the broadening is asymmetric, depending on the thermal energy of the corona. Even if the shape of the broad line is qualitatively different from the broadening predicted by Relativistic effects, we cannot say if, from an observational point of view, they can be discriminated from each other. A key role for this issue is played by the polarization signal. If the broadening is due to Comptonization rather than Relativistic effects, in fact, the line should show a measurable degree of linear polarization which can be as high as 15% of the total flux, in the best scenario.

With respect to the X-ray continuum emission in AGN, 10^8 input photons are not enough to have a good statistics. We found that Comptonization of optical/UV photons arising from a Shakura-Sunyaev disc, produces a power law in the spectral energy distribution, as well-known in literature. Optically thick coronas produce more energetic photons up to the thermal energy of

the relativistic clouds of electrons. In the case of emission from the optically thick disc, seed photons are initially horizontally polarized, in accord to Chandrasekhar predictions, up to 12%. The polarization induced by scatterings, in the SPHERICAL corona, is hidden by the initial polarization due to the disc together with the poor statistics. The optically thick SLAB corona represent the most efficient scenario in terms of scatterings and we found that multiscattering events are required to flip the orientation of the polarization vector from horizontal to vertical and hence to ascribe the polarization signal to the corona. The drawback is that multiscatterings randomize the polarization vectors and decrease the polarization degree below the initial degree of polarization. Nonetheless, a measure of vertically polarized radiation represents the proof that scatterings by relativistic electrons are acting, even if a discrimination between the considered corona geometries is not possible.

MoCA is the first fully special relativistic code for studying the polarization signal in accreting sources. The main competitor is the code developed by Schnittman and Krolik which, even if includes GR corrections, treats the scattering classically, making use of Maxwell-Boltzmann distribution for relativistic electrons and Thomson cross-section.

Our code can be improved in different ways. A first improvement can be achieved by including first order reflection of scattered photons by the disc. A ray-tracing routine which takes in account GR corrections can be easily included in the code, due to its modular architecture. The main problem with these routines is the time consumption which depends on the accuracy of the tracks but it is large, considering that the laws of motion are solved numerically. This issue can be partially overcome by translating the code in a programming language which compiles in binary, as Fortran or C.

From an observational point of view, X-ray polarimetry could live a scientific revolution thanks to the new technology of gas-based photoelectric polarimeters which are more sensitive than Bragg crystals, do not need rotation and offer imaging capability. Unfortunately all the planned mission with a polarimeter on board have been canceled and other proposed missions have not been selected. We hope that in the near future an X-ray polarimeter will fly so that our understanding of some of the most exotic phenomena in the Universe will be largely improved.

Bibliography

[1] Antonucci R. *Unified models for active galactic nuclei and quasars. ARA&A 31, 473-521*, 1993.

[2] Antonucci R. and Miller S. *Spectropolarimetry and the nature of NGC 1068. ApJ 297, 621-632*, 1985.

[3] Bellazzini R. et al. *X-ray polarimetry with Gas Pixel Detectors: A new window on the X-ray sky. NIMPA 576, 183-190.*, 2007.

[4] Belloni T. *High-energy spectra from black-hole candidates. NucPhys B PS 132, 337-345.*, 2004.

[5] Belloni T. et al. *The evolution of the timing properties of the black-hole transient GX 339-4 during its 2002/2003 outburst. A&A 440, 207-222*, 2005.

[6] Blustin A.J. et al. *The nature and origin of Seyfert warm absorbers. A&A 431, 111-125*, 2005.

[7] Chandrasekhar S. *Radiative Transfer. Dover Publications, Inc.*, 1960.

[8] Clavel J., Wamsteker W., and Glass I.S. *Hot dust on the outskirts of the broad-line region in Fairall 9. ApJ 337, 236-250*, 1989.

[9] Coe M.J. et al. *Anti-correlated hard and soft X-ray intensity variations of the black-hole candidates CYG X-1 and A0620-00. Nature 259, 544-545*, 1976.

[10] Collin S. and Huré J.-M. *Size-mass-luminosity relations in AGN and the role of the accretion disc. A&A 372, 50-58*, 2001.

[11] Connors P.A., Piran T., and Stark R.F. *Polarization features of X-ray radiation emitted near black holes. ApJ 235, 224-244*, 1980.

[12] di Matteo T. *Magnetic reconnection: flares and coronal heating in active galactic nuclei. MNRAS 299, L15-l20*, 1998.

[13] Dunn R.J.H. et al. *A global spectral study of black hole X-ray binaries. MNRAS 403, 61-82*, 2010.

[14] Elitzur M., Nenkova M., and Ivezic Z. *IR emission from AGNs. Astronomical Society of the Pacific 320, 242*, 2004.

[15] Elvis M. *A Structure for Quasars. ApJ 545, 63-76*, 2000.

[16] Esin A.A. et al. *Modeling the Low-State Spectrum of the X-Ray Nova XTE J1118+480. ApJ, 555, 483-488*, 2001.

[17] Fabian A.C. et al. *Broad Iron Lines in Active Galactic Nuclei. PASP 112, 1145-1161*, 2000.

[18] Fanning David. *www.idlcoyote.com. Fanning Software Consulting, Inc.*

[19] Fender R., Belloni T., and Gallo E. *Towards a unified model for black hole X-ray binary jets. MNRAS 355, 1105-1118.*, 2004.

[20] Fender R., Belloni T., and Gallo E. *A Unified Model for Black Hole X-Ray Binary Jets? AP&SS 300, 1-13*, 2005.

[21] Fiore F. et al. *The BeppoSAX High Energy Large Area Survey (HELLAS) - II. Number counts and X-ray spectral properties. MNRAS 327, 771-780*, 2001.

[22] Fiore F. et al. *Optical identification of sources from the HELLAS2XMM survey. Issues in Unification of Active Galactic Nuclei 258, 205*, 2002.

[23] Frontera F. et al. *Spectral and Temporal Behavior of the Black Hole Candidate XTE J1118+480 as Observed with BeppoSAX. ApJ 592, 1110-1118*, 2003.

[24] Galeev A.A., Rosner R., and Vaiana G.S. *Structured coronae of accretion disks. ApJ 229, 318-326*, 1979.

[25] George I.M. and Fabian A.C. *X-ray reflection from cold matter in active galactic nuclei and X-ray binaries. MNRAS 249, 352-367*, 1991.

[26] Ghisellini G., Haardt F., and Matt G. *Aborted jets and the X-ray emission of radio-quiet AGNs. A&A 413, 535-545*, 2004.

[27] Giacconi R. et al. *Evidence for x Rays From Sources Outside the Solar System. Physical Review Letters, vol. 9, Issue 11, pp. 439-443*, 1962.

[28] Grove J.E. et al. *Gamma-Ray Spectral States of Galactic Black Hole Candidates. ApJ 500, 899*, 1998.

[29] Haardt F. and Maraschi L. *A two-phase model for the X-ray emission from Seyfert galaxies. ApJ 380, L51-L54*, 1991.

[30] Haardt F., Maraschi L., and Ghisellini G. *A model for the X-ray and ultraviolet emission from Seyfert galaxies and galactic black holes. ApJ 432, L95-L99*, 1994.

[31] Haas M. et al. *The ISO view of Palomar-Green quasars. A&A 402, 87-111*, 2003.

[32] Homan J. et al. *Correlated X-Ray Spectral and Timing Behavior of the Black Hole Candidate XTE J1550-564: A New Interpretation of Black Hole States. ApJ 132, 377-402.*, 2001.

[33] Kraemer S.B. et al. *Simultaneous Ultraviolet and X-Ray Observations of the Seyfert Galaxy NGC 4151. II. Physical Conditions in the UV Absorbers. ApJS 167, 161-176*, 2006.

[34] Krolik A. and Makishima K. *The Three Spectral Regimes Found in the Stellar Black Hole XTE J1550-564 in Its High/Soft State. ApJ 601, 428-438*, 2004.

[35] Krongold Y. et al. *Opacity Variations in the Ionized Absorption in NGC 3783: A Compact Absorber. ApJ 622, 842-846*, 2005.

[36] Laor A. and Netzer H. *Massive thin accretion discs - II. Polarization. MNRAS 242, 560-569*, 1990.

[37] Maiolino R., Salvati M., and Bassani L. *Heavy obscuration in X-ray weak AGNs. A&A 338, 781-794*, 1998.

[38] Maiolino R. et al. *Dust in active nuclei. I. Evidence for "anomalous" properties. A&A 365, 28-36*, 2001.

[39] Malkan M.A., Gorjian V., and Tam R. *A Hubble Space Telescope Imaging Survey of Nearby Active Galactic Nuclei. ApJS 117, 25*, 1998.

[40] Malzac J. and Jourdain E. *Temporal properties of flares in accretion disk coronae. A&A 359, 843-854*, 2000.

[41] Markoff S. et al. *A jet model for the broadband spectrum of XTE J1118+480. Synchrotron emission from radio to X-rays in the Low/Hard spectral state. A&A 372, L25-L28*, 2001.

[42] Matt G. *Dust lanes, thick absorbers, and the unification model for Seyfert galaxies. A&A 355, L31-L33*, 2000.

[43] Matt G. and Perola G.C. *The iron K-alpha response in an X-ray illuminated relativistic disc and a black hole mass estimate. MNRAS 259, 433-436*, 1992.

[44] Matt G., Perola G.C., and Piro L. *The iron line and high energy bump as X-ray signatures of cold matter in Seyfert 1 galaxies. A&A 247, 25-34*, 1991.

[45] Matt G. et al. *Treatment of Compton scattering fo linearly polarized photons in Monte Carlo codes. Radiation Physics and Chemistry, Volume 48, Issue 4, 403-411.*, 1996.

[46] Blandford R.D. et al. *On the fate of gas accreting at a low rate on to a black hole. MNRAS 303, L1-L5*, 1999.

[47] Blandford R.D. et al. *Two-dimensional adiabatic flows on to a black hole - I. Fluid accretion. MNRAS 349, 68-86*, 2004.

[48] McClintock J.E and Remillard R.A. *Black hole binaries. Edited by Lewin W.H. and van der Klis M. Cambridge Astrophysics Series, 39. Cambridge University Press*, 2006.

[49] McClintock J.E. et al. *Complete and Simultaneous Spectral Observations of the Black Hole X-Ray Nova XTE J1118+480. ApJ, 555, 477-482*, 2001.

[50] McNamara A.L. et al. *X-ray polarization signatures of Compton scattering in magnetic cataclysmic variables. MNRAS, 386, 2167-2172*, 2008.

[51] Narayan R., Yi I., and Mahadevan R. *Explaining the spectrum of Sagittarius A* with a model of an accreting black hole. Nature 374, 623-623*, 1995.

[52] Panessa F. and Bassani L. *Unabsorbed Seyfert 2 galaxies. A&A 394, 435-442*, 2002.

[53] Perola G.C. et al. *New results on the X-ray emission and its correlation with the ultraviolet in NGC 4151. ApJ 306, 508-521*, 1986.

[54] Perola G.C. et al. *Compton reflection and iron fluorescence in BeppoSAX observations of Seyfert type 1 galaxies. A&A 389, 802-811*, 2002.

[55] Poutanen J. and Fabian A.C. *Spectral evolution of magnetic flares and time lags in accreting black hole sources. MNRAS 306, L31-L37*, 1999.

[56] Poutanen J. and Vilhu O. *Compton scattering of polarized light in two-phase accretion discs. A&A 275, 337-344*, 1993.

[57] Pozdnyakov L.A. and Sobol I.M. *Comptonization and the shaping of X-Ray source spectra: Monte Carlo calculations. Soviet Scientific Reviews Section E vol 2, 189-331*, 1983.

[58] Pozdnyakov L.A. et al. *Effect of multiple Compton scatterings on an X-Ray emission spectrum. Calculations by the Monte Carlo method. Sov. Astron. 21*, 1977.

[59] Pozdnyakov L.A. et al. *The Profile Evolution of X-Ray Spectral Lines Due to Comptonization. Monte Carlo Computations. A&A 75, 214-222*, 1978.

[60] Pringle J.E. *Accretion Discs in Astrophysics. ARA&A 19, 137*, 1981.

[61] Remillard R.A. and McClintock J.E. *X-Ray Properties of Black-Hole Binaries. ARA&A 44, Issue 1, 49-92*, 2006.

[62] Risaliti G., Maiolino R., and Salvati M. *The Distribution of Absorbing Column Densities among Seyfert 2 Galaxies. ApJ 522, 157-164*, 1999.

[63] Risaliti G. et al. *Rapid Compton-thick/Compton-thin Transitions in the Seyfert 2 Galaxy NGC 1365. ApJ 623, L93-L96*, 2005.

[64] Rybicki G.B and Lightman A.P. *Radiative Processes in Astrophysics. Editor: John Wiley and Sons*, 1979.

[65] Sanders D.B. et al. *Continuum energy distribution of quasars - Shapes and origins. ApJ 347, 29-51*, 1989.

[66] Schnittman J.D. and Krolik J.H. *X-ray Polarization from Accreting Black Holes: Coronal Emission. ApJ 712, 908-924*, 2010.

[67] Schodel R. et al. *A star in a 15.2-year orbit around the supermassive black hole at the centre of the Milky Way. Nature 419, 694-696*, 2002.

[68] Shakura N.I. and Sunyaev R.A. *Black Holes in Binary Systems. Observational Appearance. A&A 24, 337*, 1973.

[69] Stella L. *Measuring black hole mass through variable line profiles from accretion disks. Nature 344, 747-749*, 1990.

[70] Sun W.-H. and Malkan M.A. *Fitting improved accretion disk models to the multiwavelength continua of quasars and active galactic nuclei. ApJ 346, 68-100*, 1989.

[71] Sunyaev R.A. and Titarchuk L.G. *Comptonization of low-frequency radiation in accretion disks Angular distribution and polarization of hard radiation. A&A 143, 374-388*, 1984.

[72] Tananbaum H. et al. *Observation of a Correlated X-Ray Transition in Cygnus X-1. ApJ 177, L5*, 1972.

[73] Tomsick J.A. et al. *Broadband X-Ray Spectra of the Black Hole Candidate GRO J1655-40. ApJ 512, 892-900*, 1999.

[74] Torricelli-Ciamponi G. and Petrini P. *Stellar envelopes as sources of broad line region emission: New possibilities allowed. A&A 394, 415-433*, 2002.

[75] Tran H.D. *Hidden Broad-Line Seyfert 2 Galaxies in the CFA and 12 μM Samples. ApJ 554, L19-L23*, 2001.

[76] Tran H.D. *The Unified Model and Evolution of Active Galaxies: Implications from a Spectropolarimetric Study. ApJ 583, 632-648*, 2003.

[77] Ulrich M.-H., Maraschi L., and Urry C.M. *Variability of Active Galactic Nuclei. ARA&A 35, 445-502*, 1997.

[78] Uttley P. et al. *Non-linear X-ray variability in X-ray binaries and active galaxies. MNRAS 359, 345-362*, 1997.

[79] van der Klis M. *Rapid X-ray Variability. Edited by Walter Lewin and Michiel van der Klis. Cambridge Astrophysics Series, 39.Cambridge University Press*, 2006.

[80] Vanden Berk D.E. et al. *Composite Quasar Spectra from the Sloan Digital Sky Survey. AJ 122, 549-564*, 2001.

[81] Zdziarski A.A. and Gierlinski M. *Radiative Processes, Spectral States and Variability of Black-Hole Binaries. Progress of Theoretical Physics Supplement 155, 99-119*, 2004.

[82] Zdziarski A.A. et al. *GRS 1915+105: the distance, radiative processes and energy-dependent variability. MNRS 360, 825-838*, 2005.

[83] Zheng W. et al. *A Composite HST Spectrum of Quasars. ApJ 475, 469*, 1997.